Stony Brook University

Collagen Maturation and Mineralization

− A Three-Dimensional Ultrastructural Evolution of Bone Tissue

A Dissertation Presented

by

Hongwen Zhou

to

The Graduate School

in Partial Fulfillment of the

Requirements

for the degree of

Doctor of Philosophy

in

Chemistry

Stony Brook University

December 2008

Stony Brook University

The Graduate School

Hongwen Zhou

We, the dissertation committee for the above candidate for the

Doctor of Philosophy degree, hereby recommend

acceptance of this dissertation.

Dr. Benjamin Chu – Dissertation Advisor
Distinguished Professor
Department of Chemistry

Dr. Benjamin S. Hsiao – Dissertation Co-advisor
Professor
Department of Chemistry

Dr. John B. Parise – Chairperson of Defense
Professor
Department of Geosciences

Dr. Isaac S. Carrico
Assistant Professor
Department of Chemistry

Dr. Michael Hadjiargyrou
Associate Professor
Department of Biomedical Engineering

This dissertation is accepted by the Graduate School.

Lawrence Martin
Dean of the Graduate School

Abstract of the Dissertation

Collagen Maturation and Mineralization
− A Three-Dimensional Ultrastructural Evolution of Bone Tissue

by

Hongwen Zhou

Doctor of Philosophy

in

Chemistry

Stony Brook University

2008

Synchrotron X-ray studies were conducted on native intramuscular shad and herring bones from the region consisting of newly secreted, unmineralized collagen fibrils, progressively toward the mineralization front, to the region where collagen fibrils are heavily mineralized. Two-dimensional (2D) X-ray diffraction/scattering patterns containing comprehensive 3D ultrastructural information over several levels of bone hierarchical structures were collected by adjusting the sample-to-detector distance.

Study on the native, unmineralized region revealed a new molecular packing scheme, which is significantly different from early postulates based on the quasi-hexagonal arrangement for tendon collagen, and is particularly suited to the biomineralization of bone. The deduced cross-sectional structure in bone collagen fibrils indicates the presence of spatially discrete microfibrils and an arrangement of

intrafibrillar space to form “channels”, which could accommodate crystals with dimensions typically found in bone apatite.

Two analytical schemes were developed to extract the structure information contained in the 2D small-angle X-ray scattering (SAXS) patterns. The first scheme involved analyzing the equidistant meridional reflections resulting from the periodic structure of collagen fibrils in their axial direction. Conventional 2D analysis is difficult because of the large discrepancy between longitudinal and lateral length scales for individual fibrils, as well as their preferred orientation. The new approach represents an unapproximated analysis of the equidistant meridional reflections, which takes the exact separation of preferred orientation and fibril size effects into account. The analytical results (e.g. axial period, fibril diameter etc.) agree well with the parameters obtained from transmission electron microscopy.

The second scheme involved analyzing the fan-shaped near-equatorial diffuse scattering originating from the lateral arrangement of the mineral phase in the collagen matrix. TEM studies of intramuscular herring bone indicate that the lateral packing of nanoscale calcium-phosphate crystals in collagen fibrils can be represented by irregular stacks of platelet-shaped crystals, intercalated with organic layers of collagen molecules. The scattering intensity distribution in this system can be described by a modified Zernike-Prins model, also taking preferred orientation effects into account. Using this model, the diffuse intensity profile that dominates the small-angle equatorial region of the scattering pattern, could be quantitatively analyzed. The analysis leads to the thickness distribution of mineral crystals and that of the intercalated organic layers, and

quantitative information about the preferred orientation of mineral stacks and the average height of crystals along the crystallographic *c*-axis.

Analysis of the XRD patterns from regions at various stages of development revealed the 3D ultrastructural evolution of collagen fibrils during maturation and mineralization. In regions containing newly formed collagen fibrils, the molecular packing in fibrils and the fibril organization in bone were less ordered, as indicated by the reduced number of Bragg reflections and the poorer orientation of collagen fibrils. As it approached the mineralization front, each stage of the bone hierarchical structure became more organized. At the initial site of mineralization, the lateral packing order of collagen molecules in fibrils was significantly improved, suggesting a strong correlation between the collagen matrix structure and the mineralization process. The high degree of lateral order was destroyed by the onset of mineralization owing to the perturbation of the matrix structure by the deposition of apatite crystals.

The mineral packing in the collagen matrix was also evaluated for regions at different degrees of mineralization. The mineral platelets were found to be very thin and showed little growth in thickness during mineralization (from ~1.8 nm at the initial site of mineralization to ~2.1 nm at the heavily mineralized region). At the same time, the intercalated organic layers shrank from an average thickness of ~7 nm to ~5 nm. The average height of crystals along the crystallographic *c*-axis increased from 30 nm to 50 nm during mineralization but the orientation distribution of the mineral stacks remained unchanged. The information about the 3D ultrastructural evolution is critical for the correct understanding of the mechanical properties, biological and physiological functions of bone during aging and in pathological conditions.

Dedicated to my parents

For their endless love and support

Table of Contents

List of Figures

List of Tables

Acknowledgements

I am deeply grateful to my advisors, Distinguished Professor Benjamin Chu and Professor Benjamin S. Hsiao, who gave me the opportunity to work on this exciting project, and taught me knowledge, the way of learning, and precious life experiences. Their passion for science and discovery has greatly influenced me on my way to pursue a doctoral degree, and will continuously encourage me in my career. They are not only excellent scientists but compassionate mentors with a genuine concern for the well being of the students and their families. I wish to thank Dr. Christian Burger who is my mentor on X-ray crystallography. He proposed to use the fiber diffraction theory by Ruland to analyze the equidistant meridional reflections (Chapter 3), and to use Zernike and Prins 1D hard fluid model to analyze the equatorial diffuse scattering (Chapter 4). All the fitting programs used to analyze the SAXS patterns were modified from the general platform developed by Dr. Burger. He also supervised the fitting and simulation work in Chapter 3, 4, and 5, as well as gave a semi-quantitative explanation (Appendix I) to the hypothesis that microfibrils instead molecules could be the direct building blocks of bone collagen fibrils (Chapter 2). His contribution is indispensable for all the discoveries presented in this study. I do appreciate Dr. Melvin Glimcher for his guidance on bone structure research and providing the financial support for this project. I would also like to thank the rest of my dissertation committee, Prof. John Parise, Professor Isaac Carrico and Professor Michael Hadjiargyrou, who gave me insightful comments and made objective judgments on my work.

During my dissertation research, I have received tremendous help from Drs. Dufei Fang (X-ray instrumentation and data analysis), Igors Sics (X-ray instrumentation), Lixia Rong (X-ray instrumentation), Rajesh Harinarayan Somani (X-ray instrumentation), Jie Zhu (X-ray instrumentation), Jinglu Chen (X-ray instrumentation and sample preparation), and Chirakkal V. Krishnan (sample preparation) of Stony Brook University, Drs. Lila Graham (sample preparation), Hao Wang (TEM and sample preparation) of Children's Hospital Boston, Harvard Medical School. I gratefully appreciate their help with my experiments. I would also like to thank the faculty and staff in the Chemistry Department, especially Professor Nancy Goroff, Jane Wainio, Katherine Hughes for their assistance with my study and research.

During the five years I spent in the chemistry department, I have developed great friendship with my senior and follow colleagues: Dr. Ling Yang, Dr. Jun Zhang, Dr. Fen Wan, Dr. Jong Kahk Keum, Dr. Kyunghwan Yoon, Dr. Pranav Nawani, Dr. Xuming Chen, Dr. Liang Sun, Dr. Xianrui Zhao, Dr. Hongyang Ma, Dr. Zhaohui Tang, Dr. Changquan Qiu, Dr. Jie Wei, Feng Zuo, Yimin Mao. Thanks them a lot for their help and support.

Last, but far from the least, I would like to thank my parents, for their endless love and support; my wife, for her love, understanding and encouragement during my graduate study; my father-in-law, for his selfless help; and my daughter, for the joy and happiness she brings to us. This dissertation is dedicated to them.

Chapter 1. Introduction

1.1 Background

Bones are the organs making up the majority of the skeletal system of vertebrates. They are strong and rigid, yet lightweight, and come in a variety of shapes, to support the body, protect the internal organs, facilitate the movement, store the minerals, as well as produce the blood cells. The main constituent of bone is the mineralized osseous tissue, or bone tissue, which endows the bone excellent mechanical properties to perform its biological functions. There are two types of bone tissue, namely, *cancellous* and *compact* bone tissue. Both are composed of mineralized collagen fibrils that are more than ten microns in length but only about 100 nanometers in diameter. The difference between the two types of bone tissue is in the spatial organization of the mineralized collagen fibrils. In compact bone the fibrils are highly oriented and densely packed, and form many levels of structural hierarchy (1-3) to reduce the risk of a sudden fracture (see Fig. 1.1). In cancellous bone the collagen fibrils are grouped into trabeculaes, which then form a three-dimensional (3D) interconnected porous network filled with marrow and blood vessels (1, 3).

Mineralized collagen fibrils are the basic structural units of bone tissue (4). From the structural point of view, the mineralized fibril can be considered as a two-phase composite material, consisting of a pre-deposited organic scaffold impregnated with the mineral phase. The principle component of the organic scaffold is a fibrous protein, genetic type I collagen, which has a right-handed triple-helical structure formed by twisting together three left-handed α-chains (5). The collagen molecules are rope-like

and about 300 nanometers long and 1.2 nanometers in diameter. They are roughly parallel in the axial direction and probably interconnected in the lateral direction through

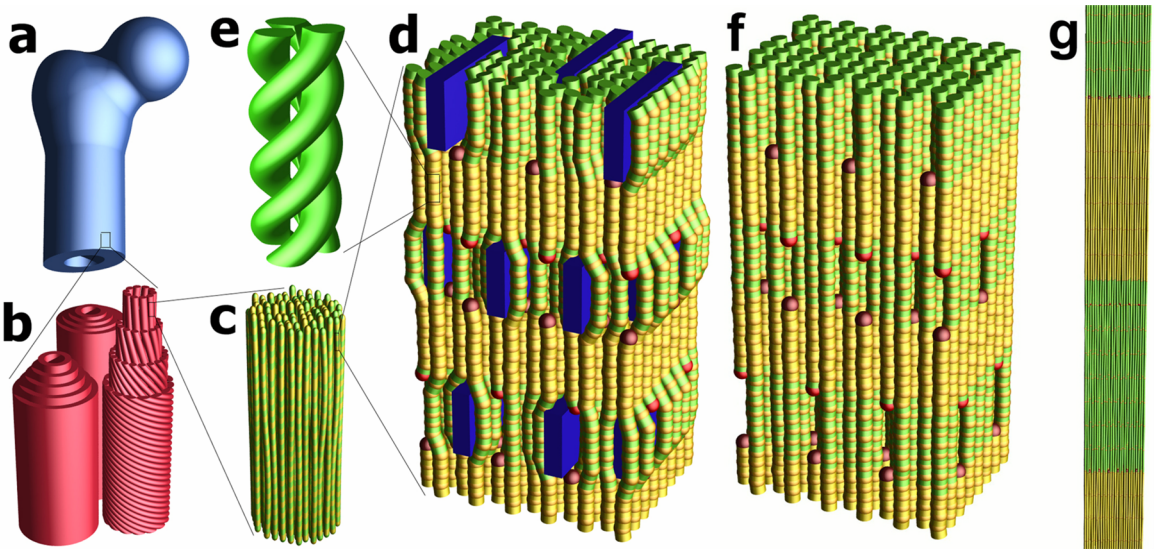

Figure 1.1 Schematic diagram of hierarchical structures in compact bone from human or other higher animals: (a) Macroscopic bone: ~ a few centimeters. (b) Haversian osteons in compact bone: ~100 microns in diameter, consisting of several concentric lamellar layers that are built from parallel collagen fibers. (c) Fine structure of collagen fiber: ~5 microns in diameter, consisting of collagen fibrils: ~50–100 nanometers in diameter. (d) Collagen molecular packing with mineral in the fibril: ~67 nanometers axial period. Collagen molecules are shown as green and yellow rods. Mineral crystals are shown as blue tiles. The figure has a 10:1 aspect ratio distortion. (e) Single molecule triple helix: ~1.0 nm in diameter. (f) Uncalcified collagen matrix (also with a 10:1 aspect ratio distortion). Note that the arrangement of the collagen molecules in the cross-section of the bone collagen fibrils is based on the so-called 'consensus' model deduced for rat tail tendon collagen. No such structural information has been obtained for bone collagen yet (see text below). (g) True aspect ratio of molecular packing in fibril. Courtesy to Dr. Christian Burger.

cross-links (6-8). The mineral phase is in the form of nanometer-scale apatite platelets contained within the fibrils (9-12). Mechanically, bone requires the mineral phase for stiffness, while the role of organic scaffold is to provide resistance to breaking. Bone, however, has a greater bending strength than either collagen or mineral alone, and

modeling studies indicate that its mechanical properties (as a material) are a function not only of its percentage composition of protein and mineral (degree of mineralization), but also of the nanoscale dimensions and precise spatial arrangement of its collagen and apatite (13-15). The biological functions of bone also require that collagen fibrils must have a particular structure, which allows apatite to be deposited at specific sites in the fibrils during the mineralization process (6, 7, 16), and later be available to assist in maintaining blood levels of calcium and phosphate (homeostasis) (17). Thus, to fulfill both the mechanical and physiological functions, bone collagen fibrils evidently require a highly specialized internal architecture.

However, it should be mentioned that detailed information about the spatial arrangement of the collagen molecules and the mineral phase in bone collagen fibrils (Fig. 1d) is rather limited. Using conventional transmission electron microscopy (TEM) to observe the molecular packing in bone collagen fibrils is difficult because in the heavily mineralized portion the fibril cross-section is dominated by the mineral phase and individual collagen molecules are not discernable (18), while in the lightly mineralized or unmineralized portion the native collagen structure could be easily altered by the sample preparation process—which is more severe for soft materials. Using cryo-TEM may alleviate this problem, but to our knowledge, such an experiment has not been conducted on bone collagen. X-ray and neutron scattering techniques are non-destructive. However, in order to obtain high-quality scattering patterns and thus to determine the molecular packing in bone collagen fibrils, the sample must contain a macroscopic volume of well-oriented and unmineralized collagen fibrils—a prerequisite that most bone tissues cannot meet. Therefore, most knowledge on the collagen matrix structure, as reviewed below,

was obtained from other connective tissues (e.g., rat tail tendon) which do not mineralize under normal physiological conditions.

To facilitate studies of the internal fibril structure by small-angle X-ray scattering (SAXS), the ideal case would be a parallel arrangement of all collagen fibrils, so that the central vertical section (referred to as the "meridian") of a SAXS pattern provides information about longitudinal periodicities in the fibril axis direction, and the central horizontal section (referred to as the "equator") contains information about the lateral (cross-sectional) packing of the molecules. Early investigations revealed equidistant meridional reflections spaced by about 67 nanometers (19, 20), indicating the presence of a periodic structure in the fibril axis direction, consistent with the "band pattern" as observed by electron microscopy (21). The Hodge-Petruska scheme (22) that describes the arrangement of the collagen molecules in the direction of fibril axis (see Fig. 1.2) was based on these observations. Specifically, parallel collagen molecules are aligned with their ends displaced longitudinally relative to their nearest neighbors by a multiple of 67 nanometers or "*L*". Since the length of the collagen molecules is about 4.5 times *L*, they have four *L*-length segments, the C-terminal being 0.5 *L* and separated axially from the N-terminus of its neighbor by a "hole" of length 0.5 *L*. The translational shifts of the whole collagen molecules by integer multiples of the period imply that all the "holes" end up into "hole" regions, followed by "overlap regions" not containing any holes. Since every fifth position in the "hole" region is not occupied by a molecular segment, the density of the "hole" regions projected onto the fiber axis is lower than that of the "overlap regions", resulting in the characteristic "band pattern" in electron-micrographs

of the negatively-stained collagen fibrils. The mineral crystals, at least at the early stages of calcification, are deposited in the "hole' regions of the organic matrix (23), with their long axes (coinciding with the crystallographic *c*-axis of hexagonal apatite) preferentially oriented about the fibril axis (24-26).

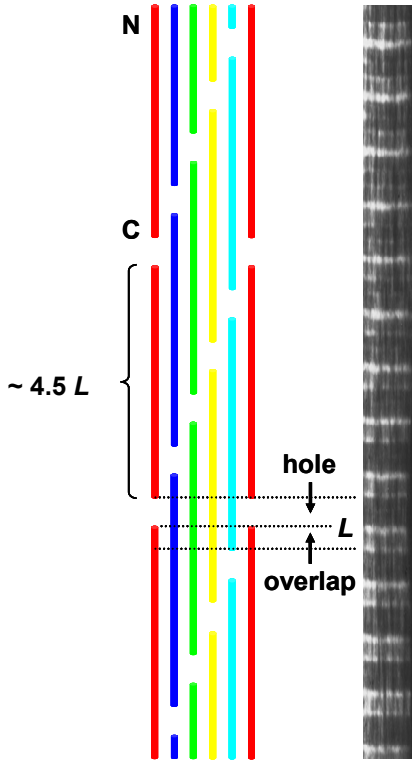

Figure 1.2 Longitudinal arrangement of the collagen molecules (shown as long rods) in the fibril. Rods with the same color represent collagen molecules with $5nL$ axial shift, where n is an integer and L is the longitudinal period observed by small-angle X-ray diffraction or electron microscopy. The electron micrograph is reprinted from ref. 22 with permission.

Note that the discussion so far was completely independent of any details of the lateral arrangement of the collagen molecules, in particular of the arrangement of the "holes" in the "hole" region, but only considered the projection of the total density onto the fibril axis. It is crucial to understand that the vast majority of experiments can only provide this projected density and does not lead to information about the lateral packing. For example, the equidistant meridional SAXS reflections observed in all patterns from fibrous collagen only depend on the density projection onto the fiber axis (27-29). If no

conclusive off-meridional scattering is observed, which frequently is the case, no information about the lateral packing can be extracted from the experiment. Likewise, transmission-electron micrographs show a two-dimensional projection but are not able to spatially resolve the short distances (~1.5 nanometers) between individual collagen molecules so that the contained information (30, 31) is equivalent to that contained in the meridional SAXS reflections and does not address the lateral arrangement.

Information about the lateral arrangement of the collagen molecules in collagen fibrils is, of course, highly relevant, in particular, with respect to its influence on the mineralization process and the correlations between the collagen matrix and the arrangement of the mineral crystals. Different models had been developed to address this problem and the most famous one is probably the quasi-hexagonal model (32) (and its various derivatives (33-37)). This model proposed that collagen molecules are packed in a quasi-hexagonal manner (Fig. 1.3) in the fibril cross-section and it can successfully explain the SAXS results for rat tail (38, 39) and several other tendon collagens (40-42). However, strong lateral packing order has not been observed for collagen from other sources and it is not clear how representative the quasi-hexagonal model is. More importantly, attempts to apply the quasi-hexagonal molecular packing model to the bone matrix structure result in inconsistencies with some well-documented observations. For example, the typical size of the apatite crystals is ~30 nanometers in length, ~20 nanometers in width, and ~2 nanometers in thickness (1, 10), which is significantly larger than the size of a single “hole” (1.5 nm).

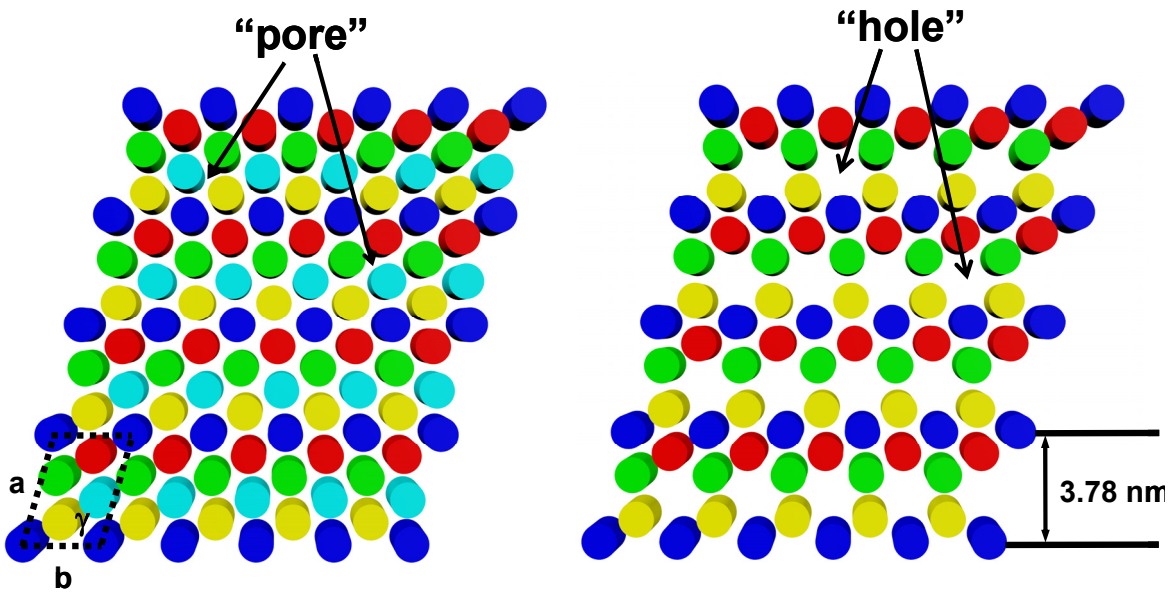

Figure 1.3 Schematic representation of the molecular packing in the fibril cross-section cutting through the overlap zone (a) and the hole zone (b) based on the quasi-hexagonal model. Disks with same color represent the cross-section of molecules with same axial shift ($0 \cdot L$). Unit cell lattice constants $a = 3.903$ nm, $b = 2.667$ nm, $\gamma = 104.6°$ are based on Miller and his colleagues' work (32). The closest center-to-center intermolecular distance is about 1.5 nm. The diameter of collagen molecules is about 1.2 nm. Thus, the size of the "pore" or intermolecular gap is about 0.3 nm, which is smaller than that of unhydrated PO_4^{3-} ion (~ 0.4 nm) (43, 44). The "hole" has a cylinder-like shape with a diameter of about 1.8 nm. A single "hole" cannot accommodate a platelet-shaped mineral crystal.

If the holes are evenly distributed in the transverse direction, as suggested by the quasi-hexagonal molecular packing model, how can a small hole accommodate a large apatite crystal? In order to deal with this discrepancy, it was proposed that holes may be aligned along the transverse direction to form "grooves" (45) or "channels" (4, 46, 47), which are large enough to accommodate apatite crystals. However, even if the "channel" model were correct, it would only be able to explain the mineral content up to small degrees of mineralization, since the small volume fraction of the holes does not change by rearranging them into "channels". Furthermore, any regular arrangement involving "channels" in the fibril cross-section must necessarily lead to a parallel periodic

alignment of the channels, which would generate equidistant row lines/equatorial peaks at relatively low angles. If any reflections at all were observed in this region, either in the literature or in our observations from the intramuscular herring bone, they were not equidistant, which is inconsistent with the "channel" model (see Chapter 2 for more details).

An alternative lateral packing model assumes that collagen molecules firstly form intermediate structural units, called microfibrils. A Smith type microfibril (48) consists of five closely-packed molecules in the cross-section and has a diameter of about 4 nanometers. The model is mainly supported by microscopic studies in which microfibrils appear to be directly visualized (49-53), and by the observation that collagen fibril diameters appear to vary in steps of 8 nanometers (54). The modified microfibril model (55, 56) offers a pathway to the quasi-hexagonal molecular packing models by deforming the microfibrillar cross-section, so that the molecule centers can be arranged on a hexagonal grid ("compressed microfibril"). Microfibrils have been observed for collagens from various tissues and species (57, 58). However, the criticism has often arisen that "microfibrils" seen by morphological techniques could be artifacts from sample preparation. Additionally, most aspects of the packing of microfibrils within the fibril remained an unsolved problem.

The third lateral packing model proposed that collagen molecules have a liquid-like arrangement in the fibril cross-section, since SAXS patterns from collagens of most tissues and species did not show well-resolved off-meridional reflections that indicate an ordered lateral packing (59, 60). Based on these observations, Fratzl proposed the 'random tessellation model', suggesting that the mineral phase is randomly deposited in

the fibril cross section (61). The model assumes that mineral crystals have irregular shape, which is not consistent with the observation that mineral crystals are platelet-like. Owing to their anisotropic cross sections, the apatite platelets cannot be expected to have a completely random arrangement unless their volume fraction is very low. On the other hand, the arrangement cannot be highly regular, or the equatorial scattering would not be as diffuse (see Chapter 3 for more details) as it has been observed.

1.2 Motivation

The objective of the present research is to answer the following set of questions. First, how does the structure of the native bone collagen matrix look like before mineralization occurs? The answer to this question could be key to understanding the correlation between the function of mineralization and the structure of the uncalcified bone collagen matrix. Secondly, how does the 3D collagen/mineral supramolecular architecture evolve from the inception of mineralization to being mature and aged? Such information will be helpful to understand the change in the mechanical properties during bone development.

In order to investigate these questions, we performed a comprehensive synchrotron X-ray study on intramuscular herring and shad bone samples. These bones were chosen for a number of reasons. First, intramuscular herring and shad bones show a contour length-dependent degree of mineralization, including an unmineralized collagen portion that is ready to be mineralized. Thus, the problem of structural distortion in collagen matrix as it becomes impregnated with the mineral phase can be avoided. Second, intramuscular fish bones have a much simpler internal organization at all levels

of anatomic hierarchy than calcified collagens of most other species. Collagen fibrils act as direct building blocks in these native samples. No other intermediate structural units (e.g. Haversian osteons, concentric parallel lamellar layers or fibers) or complicated organization and especially orientation (e.g. plywood-like structure) of these units are encountered in intramuscular shad/herring bone. Therefore, each fish bone can be considered as a single collagen entity composed of bundles of fibrils with their principal axes preferentially oriented about the primary bone axis. Third, collagen fibrils are relatively loosely packed in intramuscular shad/herring bone. They are neither inter-wound nor strongly tilted. Fourth, the sample has cylindrical rotational symmetry. Therefore, with the bone axis perpendicular to the incident beam, a single detector frame registering a two-dimensional section through reciprocal space can, within the limits of the curvature of the Ewald sphere (to be discussed later), essentially contain the complete intensity information of three-dimensional reciprocal space.

In Chapter 2, we report the first-time observation of equatorial Bragg reflections from uncalcified bone collagen fibrils of any bone tissues. The structural model derived from these data shows that compared to the structure of rat tail tendon collagen, bone collagen structure is inherently suitable for the function of mineralization. In Chapter 3, a new scheme has been developed to analyze the equidistant meridional reflections originating from the periodic arrangement of collagen molecules in the fibril axis direction, by taking the preferred orientation of collagen fibrils into account. In Chapter 4, the disordered lamellar stack model is used to describe the lateral packing of mineral crystals in bone collagen matrix, again by taking the preferred orientation effect into account. In Chapter 5, the schemes developed in previous chapters are applied to

quantitatively analyze the SAXS patterns for bone collagen at different stages of development and the results revealed a 3D ultrastructural evolution of bone during collagen maturation and mineralization.

Chapter 2. Molecular Packing in Bone Collagen Fibrils prior to Mineralization

2.1 Introduction

Bone collagen differs from collagens of other connective tissues because it can mineralize under normal physiological conditions. With regard to the factors that determine if a tissue can mineralize, much research has been focused on the presence or absence of certain noncollagenous proteins (62-65), while the role of the collagen three-dimensional (3D) supramolecular structure itself is often overlooked (66). Until now, the 3D collagen supramolecular structure is only known for very few tendon tissues (40-42), in particular, the rat tail tendon (RTT). The longitudinal arrangement of collagen molecules in RTT fibrils can be described by the Hodge-Petruska scheme (22), whereas the quasi-hexagonal model is a good approximation to describe the lateral arrangement of collagen molecules in the fibril cross-section (32). However, it is also known that the RTT collagen is a tissue that cannot be mineralized *in vivo*.

For bone collagen, the longitudinal arrangement of molecules in fibrils is considered to be similar to that of RTT collagen (67). However, the molecular packing in the lateral direction is largely unknown due to the following reasons. Firstly, normal bone tissues are heavily mineralized. The collagen matrix structure in the fibrils is perturbed by the deposition of mineral crystals. This perturbation eliminates most lateral correlations that would be essential to characterize the packing order (68). Secondly, unmineralized collagen can be found in some embryo bones; however, the poor orientation of the collagen fibrils in those bones again hinders the determination of 3D spatial correlations

from corresponding X-ray diffraction (XRD) results. Thirdly, electron microscopy could be applied to study individual fibrils, thereby avoiding the orientation problem. However, electron microscopy cannot resolve individual collagen molecules and their packing in the fibril cross-section because of low density contrast, in addition to problems caused by destructive sample preparation processes.

In view of the lack of structure information for bone collagen, RTT collagen fibrils have usually been used as a model for the structure of bone collagen fibrils. However, the RTT-based supramolecular model raises two important problems. (1) "Pores" or intermolecular gaps (Fig. 1.3) in this model are too narrow to allow PO_4^{3-} ions to penetrate into the fibril—a necessary process for the accumulation of the mineral phase (43, 44). (2) The size of a single "hole" is too small (Fig. 1.3) to accommodate a platelet-shaped mineral crystal (1) with a typical size of ~ 30 nm in length, ~ 20 nm in width, and ~ 2 nm in thickness (10-12). In order to address these problems, it was proposed that, with some reshuffling on a quasi-hexagonal lattice, "holes" could be aligned laterally, producing "grooves" or "channels", with sufficient room for crystals (45, 46). However, this hypothesis was not supported by any experimental results, since the native, uncalcified and thus undisturbed bone collagen had never been studied.

The intramuscular fish bone used for this study consists of a long unmineralized portion in which collagen fibrils are nearly parallel to the principle bone axis. Thus, the problem of structural distortion of collagen fibrils as they become increasingly mineralized can be avoided. As a result, this approach has produced sufficiently detailed XRD data to allow derivation of a structural model, providing new insight into the lateral packing of collagen molecules in bone collagen fibrils.

2.2 Experimental

Sample Preparation. Intramuscular bones were dissected from herring (Clupea harengus, 3 to 5 years old) and shad (4 to 5 years old) which had been frozen in liquid nitrogen immediately after sacrifice. Attached tissues were carefully removed in order to reduce the background scattering. After dissection, the bones were immediately cooled to liquid nitrogen temperature, and then stored at −78.5°C for no more than a few days before use. The bone specimen has a roughly cylindrical shape with a diameter of about 0.5 mm. Fresh RTT samples were prepared using the similar procedure as that for wet bone samples and were used without staining. The dry bones were prepared by exposing them to flowing air (laboratory hood) at room temperature for one day. Dry RTT sample was stretched in air for 3 min with 16.6 g weights. Prior to the X-ray study, fresh bone and RTT samples were sealed in thin-walled quartz capillary tube from Charles Supper Co. (wall thickness ~ 0.01 mm, O.D. ~ 1.0 mm) to preserve the normal internal hydration during measurement.

X-ray Scattering Instrumentation. X-ray measurements were carried out on beamline X27C (69) at the National Synchrotron Light Source, Brookhaven National Laboratory. The wavelength λ used in this study was 0.1371 nm and the corresponding energy resolution ($\Delta E/E$) at this wavelength was about 0.01. A three-pinhole collimation system was constructed to reduce the beam divergence to less than 0.00024 radian. The beam diameter at the sample position was 0.2 mm. A typical sample-to-detector distance was approx. 300 mm. The exposure time ranged between 10 min to 30 min, depending on

the thickness of the sample. The number of Kapton windows was minimized by using a continuous vacuum from the pinhole system to the sample chamber.

2D XRD patterns were recorded on Fuji^{TM} HR-V imaging plates and read out using a Fuji BAS 2500 imaging plate scanner. The intensity data were processed using POLAR program, a comprehensive software package (from Stonybrook Technology and Applied Research Inc., Stony Brook, New York) for 1D/2D X-ray scattering/diffraction analysis. The scattering angle was calibrated using a silver behenate standard.

2.3 Results and Discussion

X-ray Diffraction. Synchrotron X-ray diffraction experiments were performed for unmineralized intramuscular herring bone, both in its native hydrated state and for a dried sample, together with a native and unstained RTT sample. The corresponding XRD patterns are shown in Fig. 2.1. Meridional orders extending up to 21 reflections for herring bone and up to 57 reflections for RTT have been observed. A closer look at the RTT row-lines reveals the split reported by Miller and Wray (39) due to a small tilt of the molecules in the fibril (33).

The fish bone collagen XRD pattern (Fig. 2.1a,c) probes the unmineralized collagen region just beyond the mineralization front of the intramuscular fish bone. In contrast to the vast majority of collagen XRD patterns not from RTT, this pattern shows a large number of well resolved off-meridional reflections, allowing experimentally substantiated conclusions on the lateral packing of bone collagen that, to our knowledge, have not been possible before.

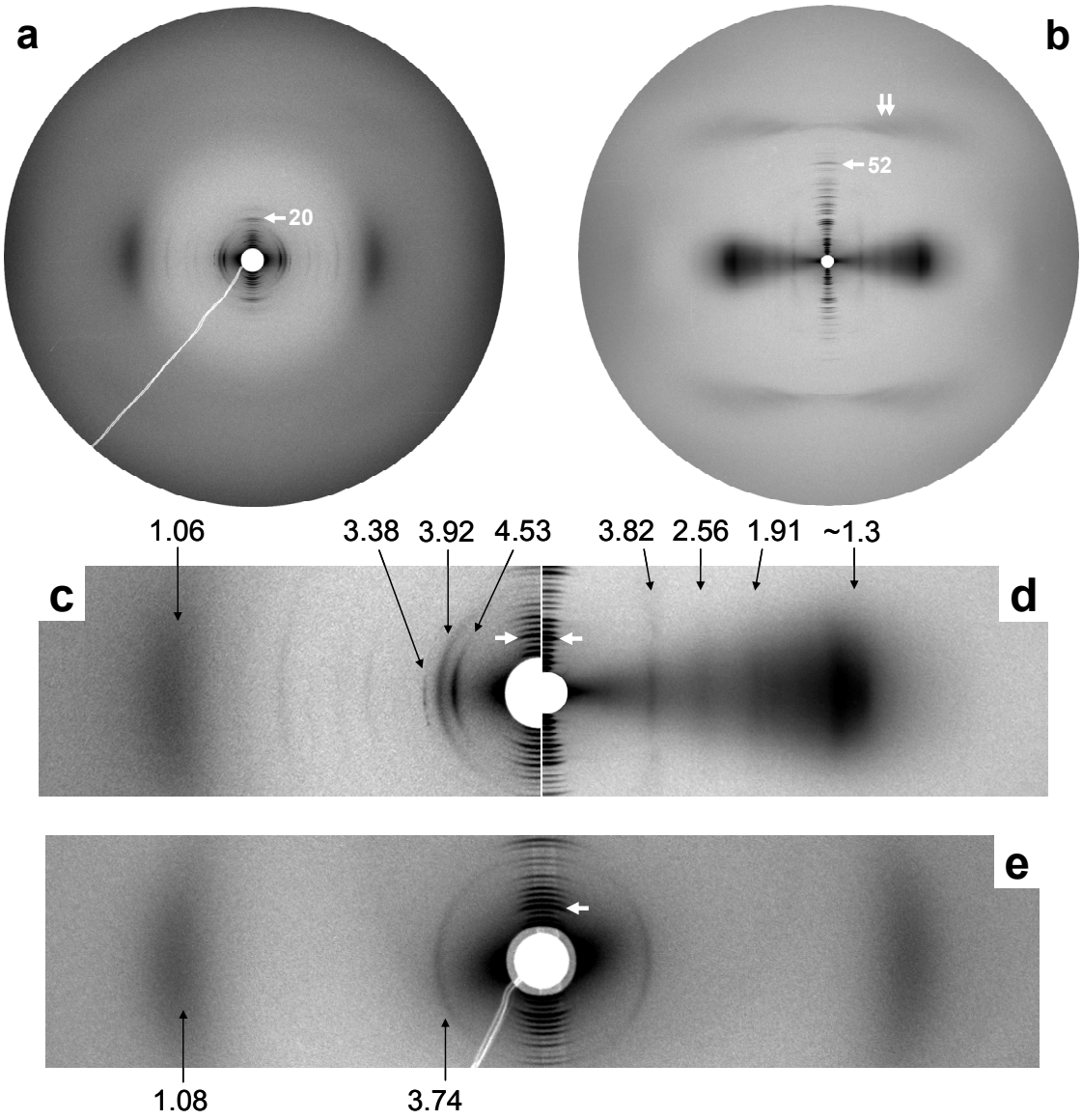

Figure 2.1 XRD patterns of (a) native, not yet mineralized intramuscular herring bone and (b) native unstained rat tail tendon (RTT). The long axis of the fiber-shaped bone or tendon was parallel to the vertical direction, so the meridian is vertical and the equator is horizontal. The arrows indicate the 20th meridional order of herring bone and the 52nd meridional order of RTT. The double arrow indicates the 3rd layer line of the collagen molecule triple helix. The center portions of the two scattering patterns (a) and (b) are shown enlarged in (c) and (d), respectively. The observed RTT pattern is consistent with the previous results, based on which the quasi-hexagonal molecular packing model (32) and its various refinements (33-35, 37) were proposed. (e) shows the XRD pattern from a dehydrated unmineralized intramuscular herring bone sample. In (c), (d), and (e), numbers indicate Bragg spacings in nm, and the white arrows indicate the 9th meridional order; meridional repeat periods are 64.4 nm, 67.7 nm, and 65.3 nm nm, respectively.

Prior to a discussion of structure models compatible with the experimental data, it is important to ensure that these reflections are indeed generated by the lateral packing of collagen molecules. Possible alternative sources for equatorial scattering would be (i) collagen fibrils oriented perpendicular to the principal bone axis, and (ii) scattering from regions not consisting with bone collagen, perhaps related to blood vessels or nerves. We have gathered extensive electron microscopy (EM) data for these samples, to be reported elsewhere, that do not support either case (i) or case (ii). Furthermore, close inspection of the equatorial peak shapes, centers and orientations (Fig. 2.1c) indicates that these are not consistent with a series of orders of 00*l* reflections, which would be required for case (i), while they are perfectly compatible with a lateral packing with small tilts and different coherence lengths in different directions.

Without detailed analysis, it is immediately evident that the positions of the equatorial reflections/row lines for fish bone and for RTT are significantly different (see also Table 2.1). Thus, while the unmineralized fish bone sample clearly shows a high degree of lateral long-range order, packing similar to the quasi-hexagonal structure reported for RTT collagen can be ruled out.

The high degree of lateral order needed to generate well-resolved patterns was found to be easily disturbed. It could be destroyed both by dehydration (Fig. 2.1e) and especially by the onset of mineralization, which can be observed in intramuscular fish bone by merely displacing the area of study into the mineralized region of the bone.

Exclusion of the "Channel" Concept Composed of Lines of Adjacent "Holes". Having established that bone collagen (at least for intramuscular herring bone) is

different from tendon collagen, possible structure models that could explain the XRD patterns were considered. The most important aspect of collagen fibril structural models is the arrangement of the "holes", or longitudinal spacings between molecules. Various arrangements of the holes in cross-sections of regular packing models for collagen molecules are compared in Fig. 2.2, together with calculated XRD patterns based on staggered packing of idealized rods (see Chapter III for details about calculation), following the Hodge-Petruska model (22). A comparison of the peak positions of the inner equatorial peaks/row lines of the RTT pattern (Fig. 2.1b,d) with the quasi-hexagonal hole arrangement without "channels" (Fig. 2a) shows agreement, confirming the absence of channels in tendon collagen.

Clearly, any regular alignment of "holes" into "channels" would lead to a periodic array of channels, generating an equidistant spacing of the lower order equatorial reflections (Fig. 2.2 b, c, d). To our knowledge, none of the few reported collagen XRD patterns with well-resolved off-meridional reflections showed such equidistant maxima. A comparison of the well-resolved fish bone pattern (Fig. 2.1 a, c) with the regular calculated patterns (Fig. 2.2) does not show any agreement, indicating the presence of a more complicated structure with lower symmetry.

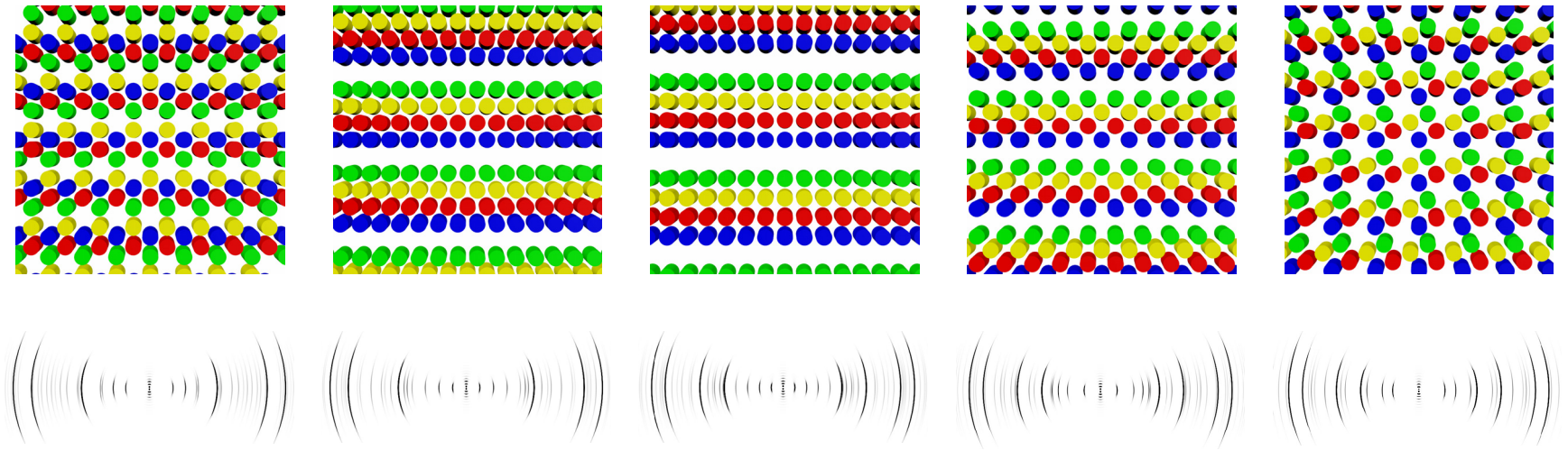

(a) quasi-hexagonal, no channels **(b) quasi-hexagonal, with channels** **(c) square, with channels** **(d) square, diagonal channels** **(e) square, no channels**

Figure 2.2 Regular arrangements of the "holes", with or without "channels" as indicated, in the fibril cross-section of the "hole" zone regions, and calculated XRD patterns (collagen molecules were idealized as rods for the calculation). Courtesy to Dr. Christian Burger.

Lattice Disorder A striking feature of the experimental XRD patterns (Fig. 2.1 a, c) is the observation that the equatorial maximum observed at relatively large angles with a Bragg spacing of around 1 nm (i.e., the length scale of the distance between individual molecules) appears significantly broader than the innermost equatorial reflections/row lines. For a lattice without disorder, where the peak widths are determined by domain size effects only, all peaks should have a constant width, as shown for the calculated patterns (Fig. 2.2). For a lattice with lattice distortions of the second kind, i.e., those that do not abruptly but gradually limit the coherence of the lattice, the peak width should gradually increase with increasing scattering angle. For a lattice with lattice distortions of the first kind, i.e., those that displace the lattice points from their ideal positions but do not destroy the coherence of the lattice, the peak widths should be constant, and the disorder causes the appearance of an additive continuous modulated background.

The abruptly broader nature of the intermolecular maximum cannot be achieved by homogeneously distorting a lattice (a lattice distortion of the second kind in Fig. 2.2). While the overall coherence and long-range order of the present lattice is good, as evidenced by the narrow equatorial peaks/row lines at small angles, the spatial correlation between the individual molecules is much more locally confined than that of the lattice itself.

The simplest (and perhaps the only) possible model compatible with these findings is to (1) group a small number of molecules into a microfibril, (2) pack whole microfibrils on a regular lattice, and (3) allow for some degree of lattice disorder of the first kind, not disturbing the long-range order of the lattice of microfibrils (keeping the inner equatorial peaks narrow) but limiting the correlation of the individual collagen

molecules between different microfibrils. In the simplifying limit of rotational disorder, i.e., each microfibril is rotated by an arbitrary amount about its axis, statistically independent from its neighbors, the scattering of idealized systems of this type can be calculated analytically, and the broad equatorial maximum results as a fluctuation term due to the rotational disorder, as shown in detail in Appendix I. The agreement with the experimental data is not quantitative, indicating that the idealized model used for the calculation is overly simplified, but, independent of the quantitative aspects of the nature of the disorder, the experimental evidence for the presence of microfibrils has been established.

Lateral Packing of Microfibrils. The number of observed well-resolved equatorial reflections/row lines in Fig. 2.1 is large enough so that a lattice for the packing of the microfibrils can be determined with sufficient confidence. Since the equatorial arcs cannot be resolved into individual reflections that would compose the row lines, only a 2D lattice can be given.

As noted above, none of the simple 2D symmetries is applicable. All observed peaks could be indexed with a 2D oblique lattice having parameters a = 4.657 nm, b = 4.029 nm and γ = 103.5° (see Tab. 2.1). In accordance with the ratio of the molecule length to the repeat period, a microfibril should be composed of five collagen molecule segments in the overlap regions, leaving four collagen molecule segments for the hole regions, as originally proposed by Smith (48). Evidence for helical twisting has been reported in five-stranded microfibrils (37, 49, 53). Given the size of the unit cell, it should accommodate a single microfibril. While the exact internal structure of a

microfibril cannot be deduced from the present experimental data, the simplest possible model would consist of regular polygonal arrangements in the cross-section of the molecules forming the microfibrils (Fig. 2.3), with rotational disorder between a microfibril and its neighbors. For this model, a molecule center-to-center distance of 1.26 nm is found (see Appendix I). A pentagonal microfibrillar cross-section has been calculated as the lowest energy configuration for bovine type I collagen (70). A concentric arrangement of microfibrils with these dimensions is compatible with an 8 nm incremental increase of fibril diameters (54). A polygonized rather than circular concentric arrangement would minimize the distortion of the 2D lattice.

Contrary to the overlap regions formed by five-stranded microfibril segments, the hole regions contain four-stranded microfibril segments and a new kind of "channels" (indicated by double arrows in Fig. 2.3b), with a width of about 1.5 nm, that would open a pathway to enable mineralization, as schematically illustrated in Fig. 2.4. While the width of these channels is suitable to accommodate the thickness of apatite platelets (~ 2.0 nm), the mineralization process still eventually leads to a perturbation of the lateral order (Fig. 2.4 b, c) and to a suppression of equatorial peaks in the XRD pattern.

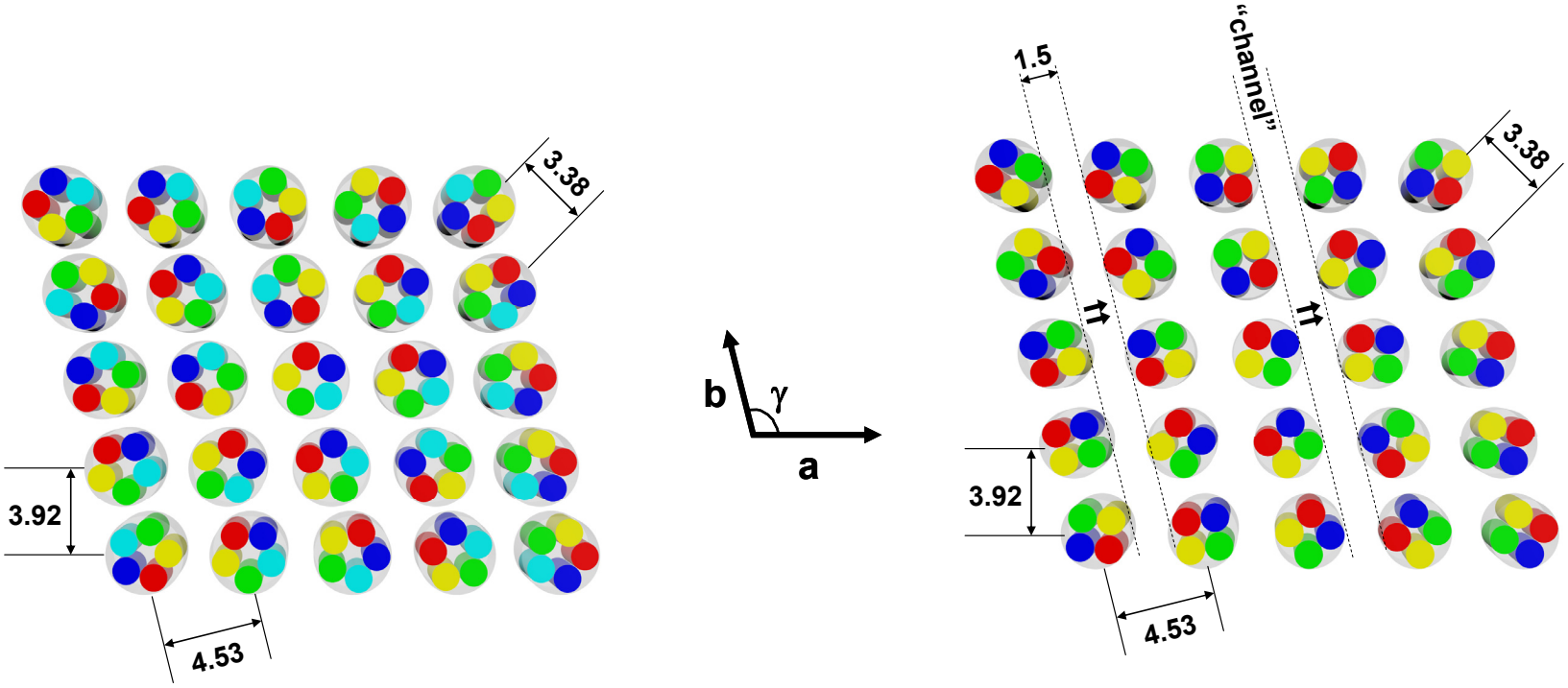

(a) (b)

Figure 2.3 Schematic representation of the lateral packing of microfibrils (ideal rotational disorder is assumed). (a) is the cross-section of the "overlap" region of a fibril (which does not contain any "holes") and (b) is the "hole" region (which does). Unit cell lattice constants are a = 4.657 nm, b = 4.029 nm, γ = 103.5°. The diameter of collagen molecules is about 1.26 nm and the diameter of microfibrils is about 3.5 nm in the "overlap" region and about 3.0 nm in the "hole" region, respectively. The smaller diameter of the microfibril in the "hole" regions opens up a new kind of "channel" different from those obtained by lining up "holes" (Fig. 2.2). The intrafibrillar volume occupied by tissue water is about 55% for bone, assuming the longitudinal length of the "hole" regions is half of the period "D" ~ 64.4 nm. For RTT collagen, the tissue water occupies 45% of the intrafibrillar volume (32).

Table 2.1 List of observed equatorial reflections/row lines as Bragg spacings in nm and *hk* indices.

Herring bone collagen				**Rat tail tendon collagen**[1]			
Obs. (nm)	Cal. (nm)	*h*	*k*	Obs. (nm)	Cal. (nm)	*h*	*k*
4.529(2)	4.529	1	0	3.817(1)	3.778	0	1
3.918(4)	3.918	0	1	2.563(6)	2.582	1	0
3.378(5)	3.378	1	-1		2.436	1	-1
2.258(3)	2.265	2	0	1.907(6)	1.918	1	1
1.944(2)	1.959	0	2		1.889	0	2
1.68[2]	1.689	2	-2	1.778(9)	1.748	1	-2
1.506(1)	1.510	3	0	1.37[2]	1.369	1	2
1.29[2]	1.306	0	3		1.328	2	-1
				1.27[2]	1.264	1	-3
					1.259	0	3

[1] RTT spacings are based on a refined quasi-hexagonal lattice with a = 2.667 nm, b = 3.903 nm, γ = 104.58° as given by ref. (32).
[2] Row-line spacings without confidence estimates are the centers of broad maxima.

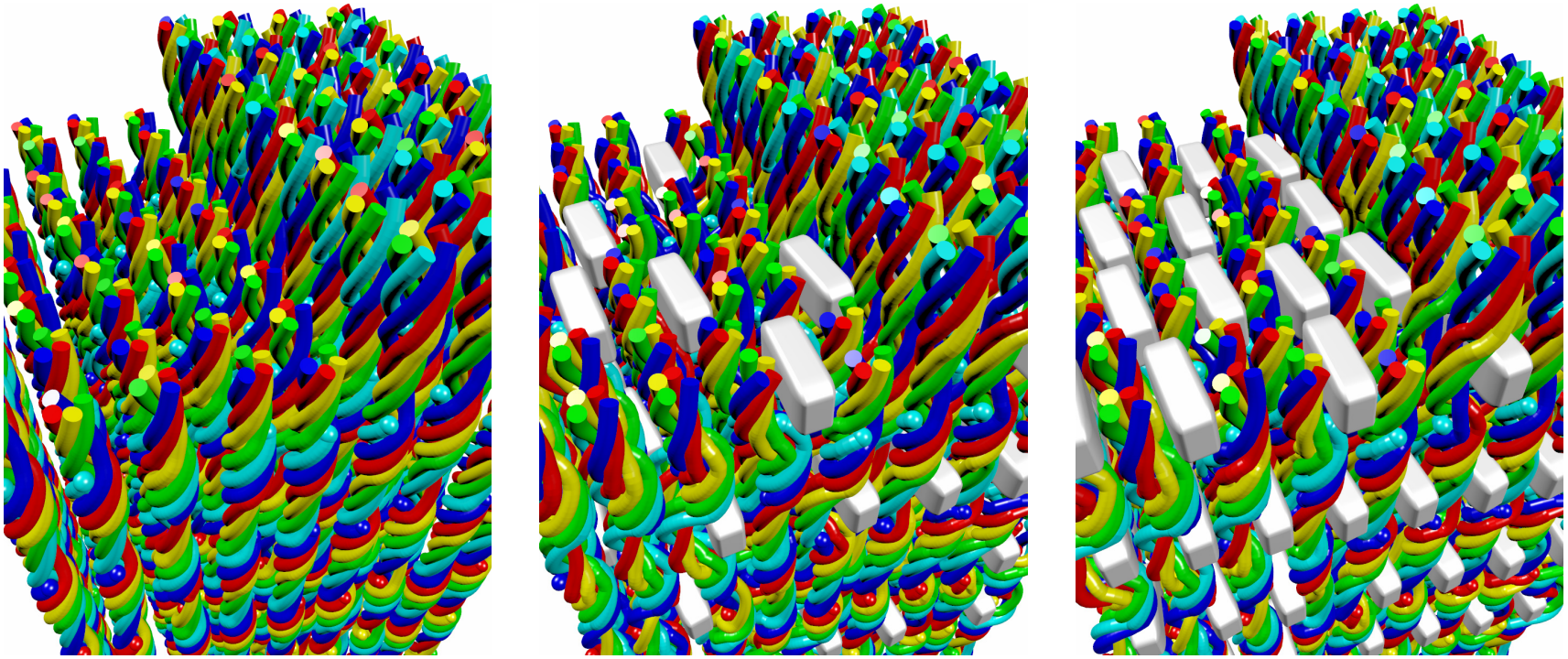

(a) unmineralized **(b) low degree of mineralization** **(c) high degree of mineralization**

Figure 2.4 Schematic illustrations of the microfibrillar packing for unmineralized and mineralized collagen, with cross-sections both through the "hole" region (left hand side of each sub-figure) and the "overlap" region (right hand side). The 2D unit cell is as in Fig. 2.3, but all longitudinal length scales are contracted by a factor of five for representational clarity. Details of the molecular packing inside the microfibrils such as helicity cannot yet be deduced from the experimental data and are assumed for the purpose of visualization. The unmineralized system (a) has "channels" in the cross-section of the "hole" region, providing space for mineral platelets. Even a small degree of mineralization (b) is sufficient to perturb the lattice of the packed micro-fibrils, attenuating the equatorial reflections. Courtesy to Dr. Christian Burger.

Dehydrated Collagen Structure. The microfibrillar model, as shown in Fig. 2.3, is consistent with the effects of dehydration of the sample on the XRD pattern (Fig. 2.1e). Collagen molecules are closely packed within the microfibrils and the microfibrils are loosely packed in the fibril. Therefore, most tissue water in the fibril exists in inter-microfibrillar spaces, while little water content is confined within the individual microfibrils. After dehydration, the tissue water is removed from the inter-microfibrillar spaces, which brings neighboring microfibrils closer to each other and the 2D oblique lattice determined for the wet bone collagen is collapsed. In other words, the unit cell, as shown in Fig. 2.3, shrinks and more disorder is introduced. Consequently, only one equatorial reflection/row line is observed for the dry bone collagen with a shorter Bragg spacing (~ 3.74 nm). However, the dehydration process has a relatively small effect on the inner structure of the microfibrils. Little water content can be removed from the intra-microfibrillar space, thus the center-to-center intermolecular distance should not change from the case in wet bone collagen, as evidenced by the positions of the corresponding interference maximum (~ 1.08 nm for dry bone vs. ~ 1.06 nm for wet bone).

In contrast, collagen molecules are the direct building blocks of RTT and are relatively loosely packed in the quasi-hexagonal lattice (Fig. 1.X). The average center-to-center intermolecular distance is about 1.5 nm and the corresponding interference maximum is located at about 1.3 nm (32, 33, 35). The tissue water is evenly distributed among the gaps between neighboring molecules. The dehydration process results in a significantly reduced average intermolecular distance (1.2 ~ 1.3 nm, estimated from the corresponding interference maximum at about 1.07 nm for dry RTT collagen, see Fig.

2.5). Meanwhile, the long range order for the lateral packing of collagen molecules is destroyed and the molecules adopt a liquid-like packing (59, 71).

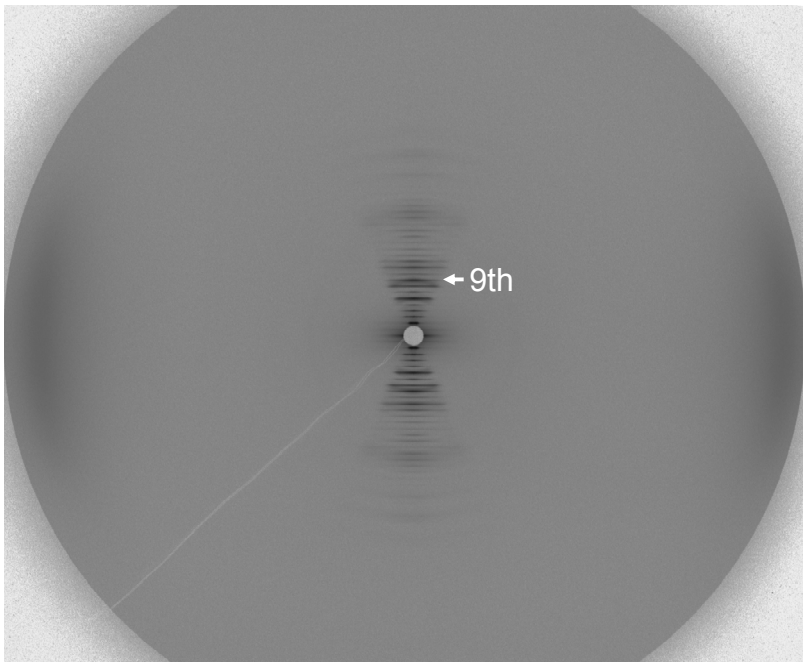

Figure 2.5 XRD pattern of dehydrated rat tail tendon collagen. The pattern was recorded with a sample-to-detector distance of ca. 740 mm. The equatorial interference maximum is located at about 1.07 nm. The arrow indicates the 9th order meridional reflection and the axial period is 64.5 nm.

2.4 Conclusion and Outlook

The new experimental findings in bone collagen fibrils include (1) unequivocal evidence for a novel fibril architecture; i.e., a large number of off-meridional reflections in bone collagen XRD patterns indicate a lateral organization that is quite different from any previously observed arrangement for tendon-like collagen fibrils, and (2) strong evidence for the presence of discrete microfibrils in the structure. Additional studies are underway to determine the range of occurrence, in other mineralized tissues, of the structure presented here. We have also observed similar equatorial reflections for

intramuscular shad bone (Fig. 2.6), which are weaker but consistent with the pattern for herring bone. While it is entirely possible that additional fibril structures remain to be discovered, if a principal criterion is to provide sufficient space for mineral crystals with minimal distortion, then the microfibril structure would be the current leading candidate for mineralized tissues in general.

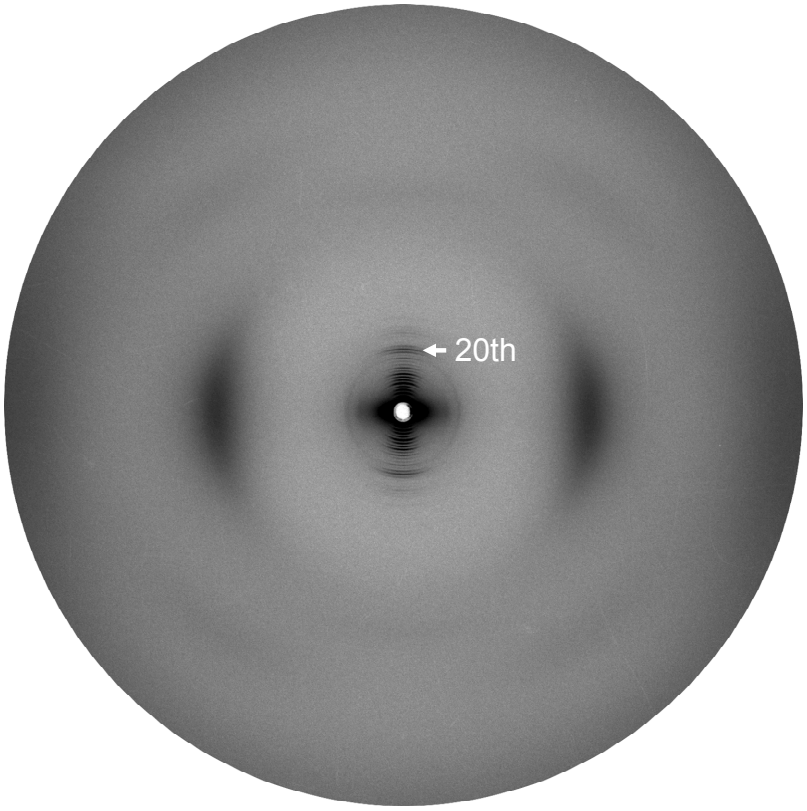

Figure 2.6 XRD pattern of fresh uncalcified intramuscular shad bone. The pattern was recorded with a sample-to-detector distance of ca. 300 mm. Two equatorial Bragg reflections/row lines are observed at 4.76 nm and 3.68 nm and the intermolecular interference maximum is located at about 1.10 nm. The overall equatorial scattering features for shad bone are similar to those for herring bone, indicating that collagen fibrils in shad bone have a similar lateral packing structure as shown in Fig. 2.3. However, fewer equatorial reflections are observed and their intensities are weaker, suggesting the lateral packing in shad bone fibrils is less ordered. The arrow indicates the 20th order meridional reflection and the axial periodicity is 65.1 nm.

Chapter 3. Collagen Fibril Superstructure Determined from Equidistant Meridional Reflections

3.1 Introduction

The use of small-angle X-ray scattering (SAXS) techniques to investigate the structure of collagen fibrils (superstructure) has been reported for more than sixty years (19). These studies revealed an axial repeat period of ~ 67−68 nm along the length of the collagen fibrils, quantifying the periodicity of the band pattern observed by electron microscopy (21). With the advancement of X-ray instrumentation and detector systems, the integrated intensities of meridional reflections were quantified and used to construct the axially projected density profile (27). Further efforts were made to relate the synthesized density profile to the molecular structure and packing in the collagen fibril (28, 30). Later on, Hulmes and colleagues (29, 72) interpreted the small-angle meridional reflections obtained from rat tail tendon in terms of the amino acid sequence and the Hodge-Petruska scheme (22). The axial structure of mineralized collagen fibrils, as proposed by Hodge and Petruska (22), in which the apatite crystals are initially deposited in the hole zone regions of the collagen fibrils, was established by transmission electron microscopy (16). This was confirmed by White *et al.* (73, 74), who demonstrated the same axial relationship between collagen and mineral in calcified turkey leg tendon using low-angle X-ray and neutron diffraction.

After the work done in the late 70's, it is probably fair to state that no major improvement has been made in terms of gaining new insights into the collagen superstructure through the use of small-angle meridional reflections. However, the

information contained in these reflections is not limited to the longitudinal period and the integrated intensities, but also includes the lateral domain size (i.e., fibril diameter), longitudinal disorder and preferred orientation. For several reasons, much of this information cannot be easily or accurately extracted using conventional analytical schemes (for a review, see (41)). Firstly, the precision of intensities measured from photographic X-ray film is often challenged by its poor linearity. Secondly, a detailed quantitative analysis of 2D patterns may also be complicated by the low angular resolution for traditional light sources and collimation systems, by the mathematical difficulties in the appropriate treatment of preferred orientation, and by computationally expensive procedures to handle large 2D intensity data sets and their evaluation procedures.

In the present work, SAXS experiments were conducted using a state-of-the-art synchrotron light source, pinhole collimation system, and advanced detectors with high spatial resolution and dynamic range (69). In order to improve the signal-to-noise ratio, special attention was paid to reduce the background scattering from air, Kapton windows, and/or X-ray instrumentation. Taking the preferred orientation effect quantitatively into account (75, 76), the small-angle equidistant meridional reflections were fitted simultaneously in 2D to the appropriate expressions. The 2D fitting approach of these non-trivial peak shapes, taking a possible sample tilt into account (77), leads to more accurate values for the integrated intensities that are required to yield more precise electron density projections onto the fibril axis. Additionally, the fitting approach generates estimates for the lateral fibril size, the longitudinal coherence length, and the quantitative information about the orientation distribution function.

3.2 Principles and Methods

Intensity Transform for Perfectly Oriented Fibrils. When fibrils are perfectly oriented with respect to the primary bone axis, each fibril can be considered as a one-dimensional lattice with an axial period of $L \sim 67$ nm. The scattering of these 1D lattices is concentrated on a series of parallel disks (layer lines) normal to the fibril axis (78), and spaced by a distance of $1/L$, as shown in Fig. 3.1a. The intensity distribution on the layer lines can be given by

$$I_{(n)}(s_{12}, s_3) = |F_n|^2 \frac{\exp(-\pi s_{12}^2 / b_{12}^2)}{b_{12}^2} \frac{\exp[-\pi (s_3 - n/L)^2 / b_3^2]}{b_3} \tag{3.1}$$

where n is the order of the reflection; s_{12} and s_3 are the components of the scattering vector $\vec{s}$ in the equatorial and meridional directions, respectively ($\sqrt{s_{12}^2 + s_3^2} = |\vec{s}| = 2\lambda^{-1} \sin\theta$, where λ is the wavelength and 2θ is the scattering angle); the prefactor $|F_n|^2$ in front of the normalized peak shape is the total peak intensity integrated in 3D reciprocal space which, after taking the square root and assigning a phase, can be used to synthesize the 1D projected density profile; b_{12} is the lateral integral width and should be a constant with order n and its reciprocal value gives an estimate for the average fibril diameter. This estimate and the Gaussian choice of the lateral component of the peak shape basically correspond to a Guinier approximation. However, practically b_{12} could be broadened by other factors besides the finite size effect, e.g., a molecular tilt with respect to the fibril axis (Fig. 3.1b) that is not handled properly by the orientation distribution function. In that circumstance, the value of b_{12} extrapolated to zero order is used to estimate the fibril diameter; b_3 is the longitudinal integral width which increases with the order n. After proper correction by the lattice disorder and collimation effects, a longitudinal coherence length could be estimated.

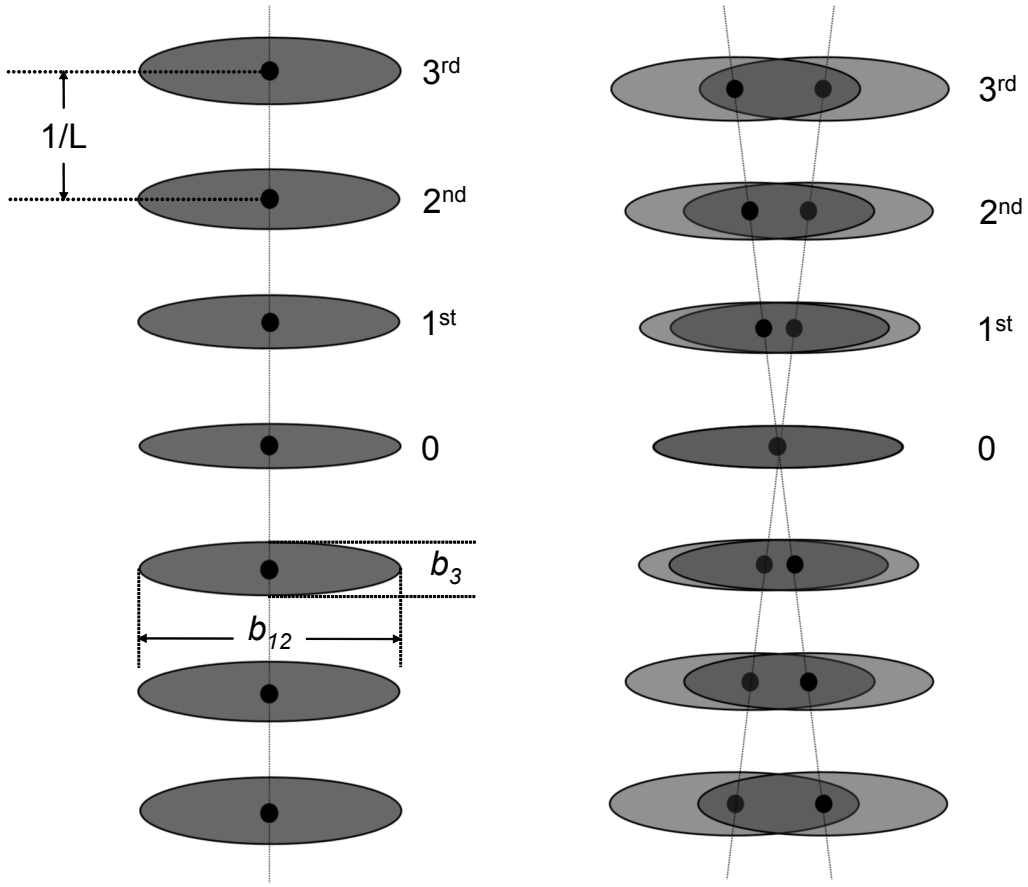

Figure 3.1 Reflection domains for perfectly oriented collagen fibrils: (a) shows the ideal case that the lateral integral width b_{12} remains as a constant for different orders. (b) shows one of the possible reasons that may cause the increase of b_{12} with order, i.e., the molecular tilt with respect to the fibril axis (see Section 3.4 "Fibril Diameter" for details). The tilt angle in the schematic diagram is exaggerated in order to show this effect explicitly.

Intensity Transform for Fibrils with Preferred Orientation. The peak shape for perfectly oriented fibrils is centered on a straight layer line. In this case, the 2D intensity distribution can usually be factorized into a lateral component (only with s_{12}) and a longitudinal component (only with s_3). On the other hand, if fibrils are partially oriented with respect to the primary axis of the specimen, as is the case in native, un-stretched turkey leg tendon (Fig. 3.2d), the peak shape of meridional reflection is approximately located on a circle and its intensity distribution can again

be factorized into a radial component and an angular component. However, information about the lateral fibril size is lost. The orientation of collagen fibrils in intramuscular shad/herring bone is somewhere in between. In addition, the fibril diameter is relatively small which results in the laterally elongated appearance of layer lines (Fig. 3.1a). Therefore, the usually applicable approximation of factorizing 2D intensity distribution breaks down. As can be seen in the experimental SAXS pattern in Fig. 3.2b, and, more clearly, in the calculated pattern (Fig. 3.2c), the bended peak shape does not lie on the circular arc. We could not find any acceptable approximation that could treat this peak shape with sufficient precision. Therefore, we resorted to the exact (i.e., unapproximated) treatment of the preferred orientation in the simple fiber symmetry case. Simple fiber symmetry means that, in addition to the cylindrical rotational symmetry of the whole fiber (fish bone), each structural unit (the collagen fibrils) also possesses cylindrical rotational symmetry. In this case, the preferred orientation of a sample can be fully described by an orientation distribution function $g(\beta)$, depending on a single angle β that is the angle between the primary bone axis and the primary axis of a structural unit (see Fig. 3.3 for definition of β). The integral transformation relating the intensity distribution $I(s,\varphi')$ of the structural unit (collagen fibril) and the orientation function $g(\beta)$ to the resulting fiber-averaged intensity distribution, $J(s,\varphi)$, has been given before (75, 76),

$$J(s,\varphi) = \int_0^{\frac{\pi}{2}} I(s,\varphi')F(\varphi,\varphi')\sin\varphi' d\varphi' \qquad (3.2)$$

where $I(s,\varphi')$ is the $I(s_{12},s_3)$ in equation (3.1) translated into the polar coordinates, the kernel $F(\varphi,\varphi')$ of the integral transformation depends on the orientation distribution, φ is the angle with respect to the primary axis of $J(s,\varphi)$, and φ' is the angle with respect to the primary axis of $I(s,\varphi')$ (Fig. 3.3).

$$\mathrm{F}(\varphi,\varphi') = \frac{1}{\pi}\int_0^{\pi} g(\beta)d\eta \tag{3.3}$$

where η is given by

$$\cos\beta = \cos\varphi\cos\varphi' + \sin\varphi\sin\varphi'\cos\eta \tag{3.4}$$

For the orientation distribution function $g(\beta)$, we chose Onsager's distribution (79)

$$\mathbf{g}(\beta) = p\cosh(p\cos\beta)/\sinh(p) \tag{3.5}$$

where p is a parameter determining the width of the distribution. The function was chosen because it has a simple analytic solution for the integral kernel $F(\varphi,\varphi')$

$$\mathbf{F}(\varphi,\varphi') = p/\sinh(p)\cosh(p\cos\varphi\cos\varphi')I_0(p\sin\varphi\sin\varphi') \tag{3.6}$$

where I_0 is the modified Bessel function of the first kind of order zero. For a system with fibre symmetry, Hermans' orientation parameter $\overline{P}_2$ is often used to characterize the degree of preferred orientation (80). For Eq. (3.5), we have

$$\overline{P}_2 = 1 - 3p^{-1}[\coth(p) - p^{-1}] \tag{3.7}$$

$\overline{P}_2$ is equal to 1 for a perfectly oriented system and is 0 if the orientation with respect to the bone axis is completely random.

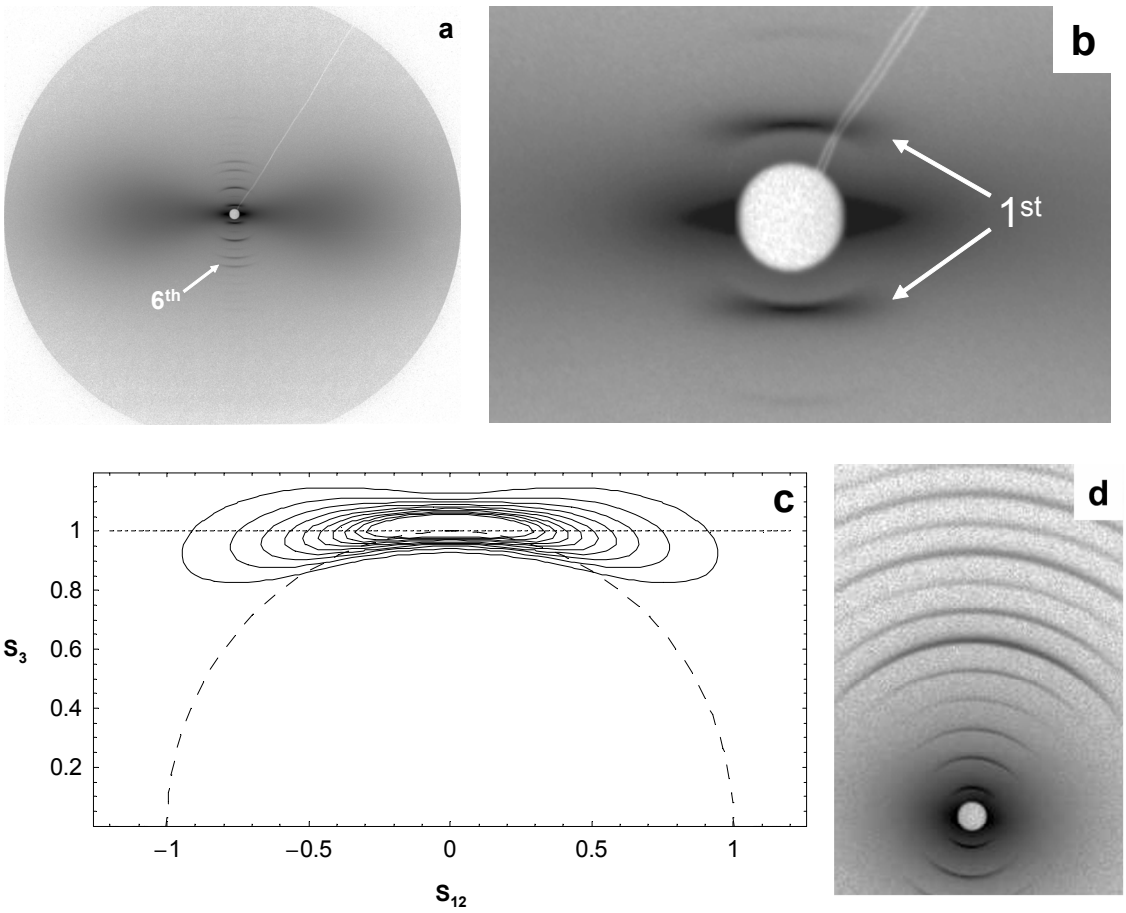

Figure 3.2 (a) 2D SAXS pattern from mineralized intramuscular shad bone. The long axis of shad bone was parallel to the vertical direction, so the meridian is vertical and the equator is horizontal. Pattern was recorded with a 1910 mm sample-to-detector distance. The 6th meridional order is indicated; (b) An enlarged portion of pattern (a) around the beam stop (small, white disk) shows that the 1st order meridional reflection is "bended"; (c) Calculated contour plot of the peak shape. The scale has been normalized to the periodicity of meridional reflections. Peak is neither on straight dotted line (perfectly oriented), nor on dashed circle (poorly oriented). Also note that the peak maximum is not exactly at the peak center; (d) Diffraction pattern from turkey leg tendon shows partial orientation of fibrils.

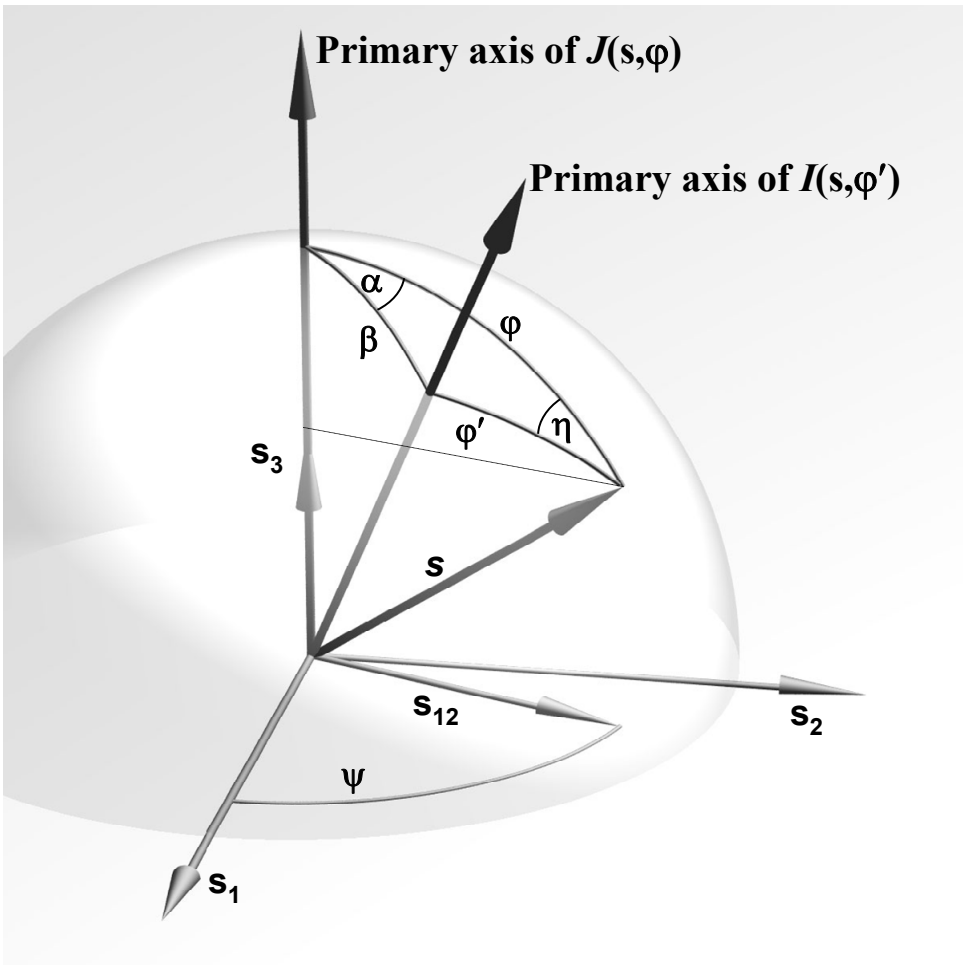

Figure 3.3 Geometrical relationship of s and the primary axes of $J(s,\varphi)$ and $I(s,\varphi')$. Courtesy to Dr. Christian Burger.

3.3 Experimental

Native intramuscular shad/herring bones were used for all experiments. Information about the sample preparation and X-ray instrumentation has been described in Chapter 2. Two-dimensional SAXS patterns were recorded with Fuji^{TM} HR-V imaging plates (IP), which possess a wide dynamic range, good linearity, sensitivity and spatial resolution. The intensity data were read out in terms of 100 μm pixel size and processed using POLAR program (a software package developed by Dr. Dufei Fang). 2D intensity regions that include meridional reflections were exported and then analyzed using customized fitting programs.

In order to fit all meridional reflections simultaneously, the background of each peak was removed individually because a global background with sufficient precision was not readily available. On the other hand, the local background around each peak could be fitted well by a 2D polynomial, which was then interpolated into the peak region. After background subtraction, the 2D intensity data of all meridional reflections were incorporated together to fit the analytical model. This procedure has the advantage that the weak orders are well-preserved or they could be overwhelmed by the imprecise global background. However, it requires that individual peaks must be sharp and well separated so that the flat region between neighbouring peaks is virtually all from background scattering. This condition is satisfied for the present small-angle equidistant meridional reflections by using a large sample-to-detector distance (~ 2000 mm) and high-resolution imaging plates.

The effects of X-ray absorption and polarization on the integrated intensity were evaluated using the method described by Brodsky and Eikenberry (41). For the present SAXS measurements, the maximum diffraction angle (2θ) was about 3°, hence the correction due to these two effects was less than 0.2% and they were

neglected. The curvature of the Ewald sphere and the possible sample tilt were taken into account during the 2D fitting procedure (77).

3.4 Results and Discussion

Intensity Analysis. Meridional reflections from unmineralized herring bone collagen (Fig. 3.4a) were analyzed by two different methods. The results are listed in Table 3.1. The same analytical scheme can also be applied to the mineralized bone collagen (81). It is shown that the intensity values obtained from unapproximated fitting approach (Method I) and numerical integration (Method II) are in good agreement for intermediate orders (6^{th} ~ 17^{th}). However, notable deviations were observed for lower orders (1^{st} ~ 5^{th}) and higher orders (18^{th} ~ 25^{th}). The relatively large pixel size of the imaging plates (100 μm for most measurements), which causes the breakdown of the rectangular integration rule, may account for the large values produced by numerical integration for lower orders. The effect is more significant for lower orders (1^{st} ~ 5^{th}) because their peak width only contains few pixels in the meridional direction. Reducing the pixel size to 50 μm can improve the precision for the numerical integration method. However, it produces four times larger data files and significantly increase the data processing time.

For higher orders (18^{th} ~ 25^{th}), Table 1 shows that intensity values obtained by numerical integration (Method II) are systematically smaller than the values obtained by fitting to the analytical model (Method I) which takes the curvature of Ewald sphere and the sample tilt effects into account. It is shown in the corrected pattern (Fig. 3.4b) that the two factors have small effects on the lower order reflections (where one would normally neglect the curvature of the Ewald sphere and employ the tangent plane approximation), but become more pronounced for higher orders.

Although the tilt angle determined from 2D fitting is usually small (< 4°), its effect is still in the same order as that caused by the curvature of the Ewald sphere. In addition, the present study emphasizes the structure of *native, untreated* bone collagen as it is in the *in vivo* condition. We avoided any stretching of the sample before and during the measurement. Instead, the sample was sealed in a capillary. For such a condition, a small sample tilt of a few degrees was almost inevitable. However, the conventional correction method (82) could not be used to deal with this effect on the integrated intensities. Therefore, we incorporated the Fraser correction method (77) into the 2D fitting procedure, making the sample tilt angle an adjustable parameter, thereby effectively filling the missing intensity gap (the blank area) through interpolation (Fig. 3.4c and Fig. 3.5), and producing more accurate values for the integrated intensities and other parameters.

Table 3.1 Integrated intensities evaluated by different methods[1]

Order	[2] I_{ori}	[3] $I_{N.I.}$
1	1000(5)	1083
2	2.6(1)	15
3	454(3)	556
4	16(1)	17
5	267(2)	331
6	49(1)	50
7	55(1)	61
8	74(1)	72
9	96(1)	96
10	33(1)	32
11	9(1)	8
12	105(2)	105
13	12(1)	8
14	17(1)	15
15	52(2)	48
16	7(1)	5
17	28(1)	26
18	43(2)	34
19	31(1)	22
20	146(3)	126
21	45(2)	38
22	17(1)	14
23	-	-
24	15(1)	13
25	45(3)	37

[1] Corresponding diffraction pattern was shown in Fig. 3.4a. Analysis was to the same set of background subtracted data. Scaling is such that the 1st order intensity obtained from the unapproximated approach (equation 3.2) is equal to 1000.
[2] Analytical scheme that taking preferred orientation effect into account (Method I). Other fitting parameters: $p = 144(1)$; $b_{12,0} = 0.0117(1)$ nm^{-1}; b_3 for different orders are plotted in Fig. 3.7; and L is shown in Fig. 6.
[3] Numerical integration (Method II) by adding up intensities registered on individual pixels with proper pre-factor (41).

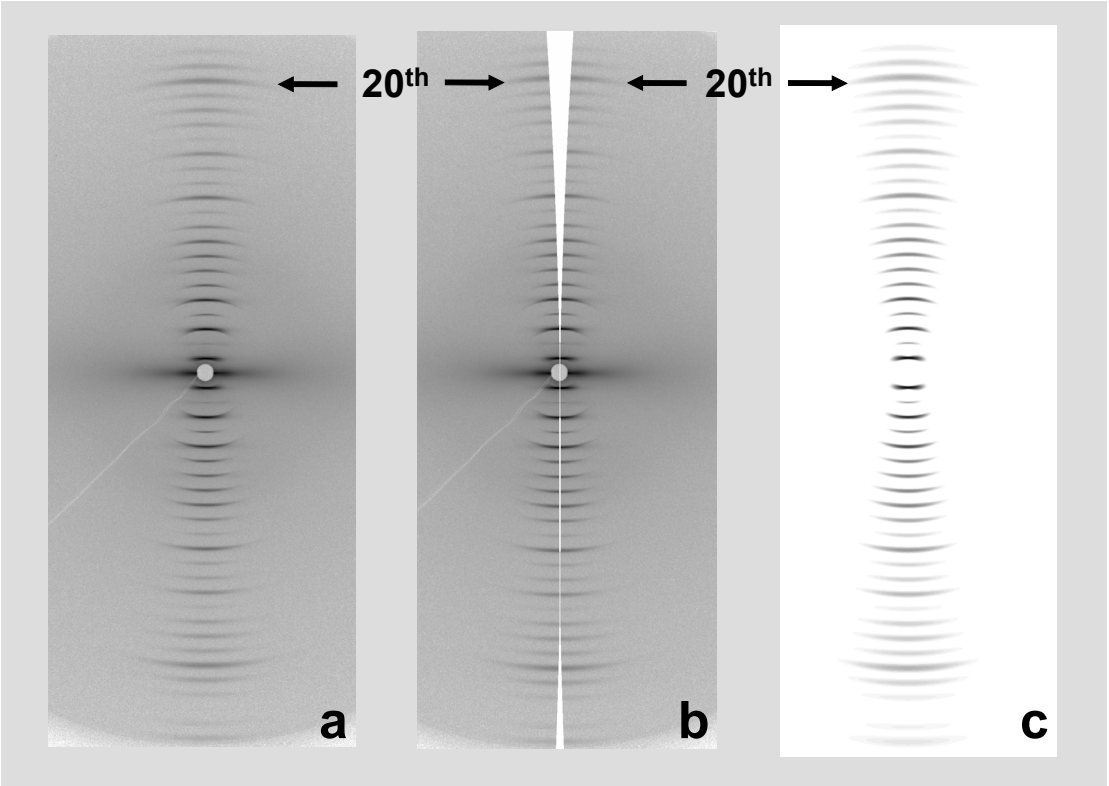

Figure 3.4 (a) Measured SAXS pattern from unmineralized intramuscular herring bone. The small asymmetry between the two sets of meridional reflections (above and below the beam stop) is not discernable by visual inspection but can be identified by POLAR program (image processing software), the asymmetry is caused by the sample tilt as well as the curvature of Ewald sphere; (b) Central section through the specimen intensity transform corrected from (a) by Fraser's method, the sample tilt (~ 0.83°) was obtained by 2D fitting of both sets of meridional reflections, the symmetry of the two sets of meridional reflections was reinstated for the corrected pattern (except for the blank areas); (c) Simulated central section through the specimen intensity transform. Parameters for calculating this pattern come from the 2D fitting results of pattern (a) and are listed in Tab. 3.1. A constant background was used for the computed pattern. The 20th orders are indicated by black arrows. The axial period of the equidistant meridional reflections is 66.6 nm.

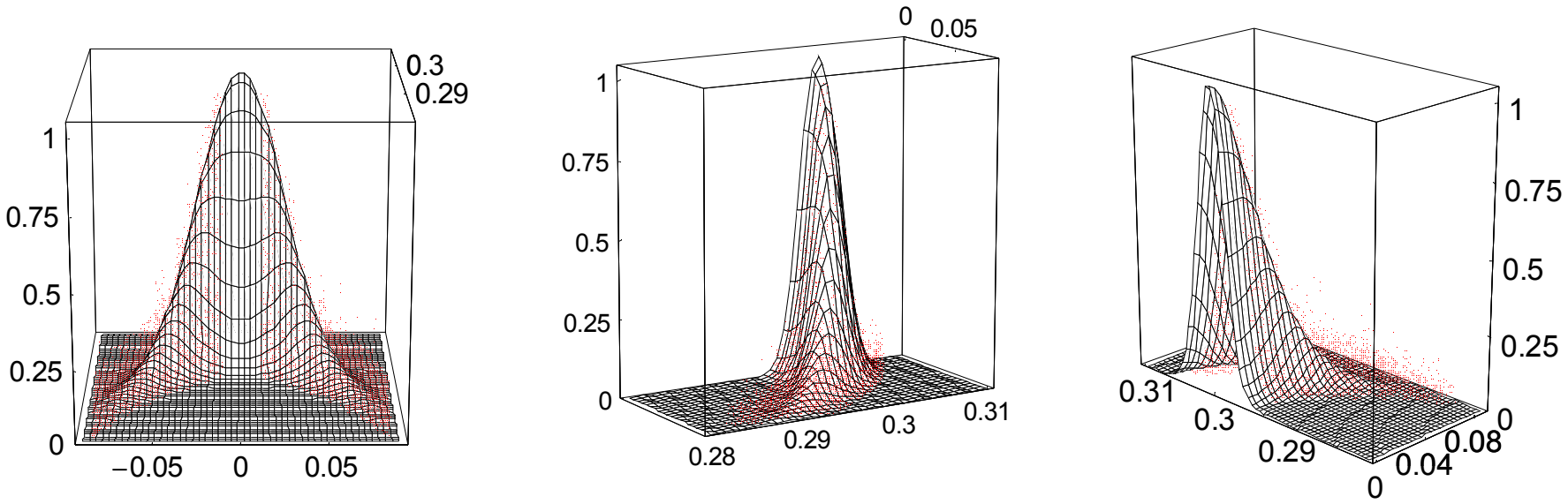

(a) (b) (c)

Figure 3.5 Retrieve of the missing intensity due to the curvature of Ewald sphere and the specimen inclination. The 20th order on the Fraser corrected pattern and the corresponding peak on the simulated pattern were overlapped. The red points represent the Fraser corrected intensity from the measured intensity. The black surface plot shows the calculated peak shape. The figures are shown in different perspectives. (a) shows that the missing intensity on the Fraser corrected pattern is suitably restored on the fitted plot. (b) and (c) show that the experimental data points are evenly distributed on both sides of the fitted surface plot.

The integrated intensities can be used to calculate the electron density projected onto the fibril axis by Fourier synthesis,

$$\rho(x) = \frac{1}{L}\sum_{n}|F_n|\exp(i\phi_n)\exp(-2\pi inx/L)\exp(-Bn^2) \qquad (3.8)$$

where x is the coordinate in the fibril axis direction, ρ is the relative density as a function of x, ϕ_n is the phase angle of the n^{th} order, and B is a Debye-Waller-like coefficient allowing for temperature and other disorder effects which have a dampening effect on the Fourier series. In order to use equation (3.8), the phases of the meridional orders must be known. Two methods have been commonly used to obtain the phases. One is to determine them from heavy atom derivatives (83), but the staining process may alter the collagen structure or cause damage to it and thereby make the resulting phase angle less accurate. The other is to calculate them from models based on the amino acid sequence and molecular conformation (29), but the primary structure of shad/herring bone collagen is not yet available. For the present analysis, we use the phase angles derived for rat tail tendon (29) to synthesize the axially projected density profile. This should be a reasonable approximation, if the chains of shad and herring bone collagen molecules are homologous to the type I α chains of rat, as is the case for zebra-fish (84-86) and rainbow trout (86).

The calculated axial electron density for herring bone collagen is shown in Fig. 3.6. The factor B was chosen based on reference (29). The gap-overlap feature is clearly seen, and oscillations that show the position of the electron dense region are also comparable to that for the rat tail tendon.

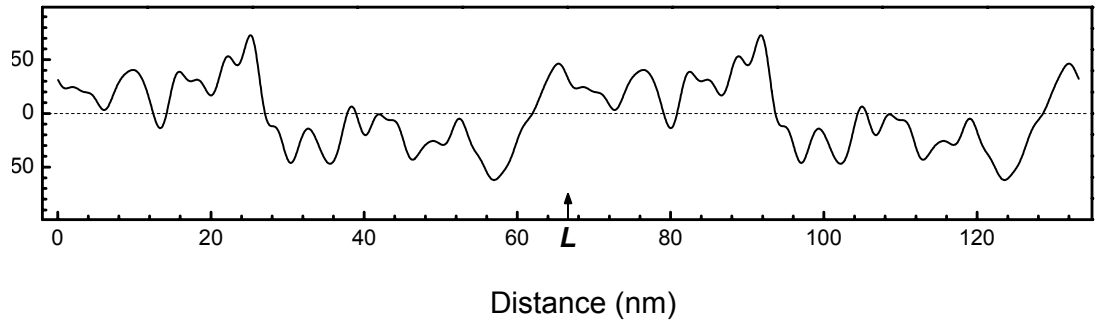

Figure 3.6 Fourier synthesis of the electron density for unmineralized bone collagen, using the intensities obtained from Method I in Table 3.1 and phases derived from model rat tail tendon (29). The axial periodicity L ~ 66.6 nm is indicated by black arrow.

Orientation Distribution. The orientation distribution of collagen fibrils in the connective tissue had been deduced from the wide-angle X-ray diffraction (WAXD) patterns before. Two methods were generally used in the literature. The first one is to analyze the angular spread of the strong equatorial peak at about 1.1 nm (87). This peak is related to the intermolecular distance in the lateral direction and its exact position varies for different tissues and species. The advantage of this method is that it is not necessary to separate the size effect and the orientation effect since for wide-angle reflections, the size effect is usually negligible unless the corresponding crystalline domain is very small. However, the method is not applicable for the mineralized intramuscular shad/herring bone, in which lateral packing of molecules is perturbed by the inclusion of mineral crystals and thereby the intensity of the equatorial reflection diminishes quickly and can no longer be used to evaluate the orientation distribution of collagen fibrils. More importantly, if the equatorial arc comes from blended row-lines,

any standard orientation evaluation not taking this fact into account will lead to ambiguous results.

The second method is to evaluate the angular spread of the high-angle meridional reflection at 0.286 nm (88). This peak is related to the axial rise of the peptide repeat in α chains and its position is almost fixed for type I collagen. Similar to the first one, this method is limited to the unmineralized collagen. Once mineralization starts, the peak at 0.286 nm due to the collagen peptide structure will be overshadowed by the broad (211) reflection of bone apatite (at 0.281 nm). It should be noted that different parts of the hierarchical structures lead to different scattering peaks and thus have different orientations. From the small-angle equidistant meridional peaks, information about the orientation of the lamellar system formed by the gap/overlap sequences, i.e., the orientation of whole fibrils in the bone sample can be obtained. Other peaks give other information. (What other information?)

By fitting the 2D intensity profile of meridional reflections to the analytical model, we obtained the orientation distribution function $g(\beta)$ for the intramuscular fish bone. However, to consider $g(\beta)$ as the orientation distribution function of bone collagen fibrils, we have neglected a possible molecular tilt about the fibril axis. This tilt is usually small (3° ~ 4°) for stretched rat tail tendon (33), and should be smaller for un-stretched fibrils (89). No values have been reported for bone collagen but it was suggested that the molecular tilt in bone fibrils should be similar to that in tendon fibrils (57, 58). Thus, the contribution from this small tilt to the overall orientation distribution $g(\beta)$ may be virtually negligible.

Fibril Diameter. As discussed earlier, the apparent b_{12} value (i.e., lateral integral width) could increase with the order n due to the molecular tilt with respect to the fibril axis. In this case, the layer lines remain straight and parallel, but each layer line is split into two components that are centered off the meridional axis, hence make the apparent b_{12} for higher orders larger than that for the lower orders. Fig. 3.1b qualitatively shows this effect. However, quantitative evaluation shows that the molecular tilt *alone* cannot explain the observed increase of b_{12} as a function of the order (unpublished results). When the molecular tilt is incorporated into the fitting as an adjustable parameter, the obtained value is too large (~ 5°) and will cause visible separation for high order meridional peaks, which is not the case for shad/herring bones. Therefore, we use an empirical function to approximate the apparent b_{12} as a function of order n

$$b_{12,n} = b_{12,0} + Cn \tag{3.9}$$

where $b_{12,0}$ is the width for zero order and free of the broadening effect and C is a proportional constant. The average fibril diameter is estimated from the reciprocal of $b_{12,0}$. For the uncalcified intramuscular herring bone studied in this work, the average fibril diameter is determined to be 85 ± 2 nm. The same system was also investigated by TEM (18) in which the fibril diameters showed a widely dispersed distribution, ranging from 50 nm to 200 nm. Our result from quantitative SAXS analysis is in reasonable agreement with the TEM observations.

Longitudinal Coherence Length. The coherence length (l_c) of collagen fibrils in the axis direction can be estimated from the peak width along the meridional direction (b_3). In the ideal case, i.e., periodic arrangement of molecules into the fibril and peptide

repeats in the α chains are free of disorder, and the incident beam is perfectly parallel and monochromatic, the coherence length can be directly calculated by the Scherrer formula $l_c = 1/b_3$. However, in reality the primary beam is divergent and has a finite wavelength distribution. More importantly, the molecular packing in the fibril contains disorder, e.g., (1) peptide repeats are not perfect considering the many types of side chains with different composition and conformation; (2) collagen molecules are relatively flexible due to the high aspect ratio; (3) noncollagenous components within or on the surface of the fibril may not be periodically distributed in the axis direction; (4) distortion is induced by calcification (for mineralized fibrils only but then the most important effect). All these factors will cause additional peak broadening along the meridional direction. In other words, the overall width (b_3) includes the contributions from the size effect (b_{size}), the instrumental effect (b_{inst}), and the disorder effect (b_{dis}). The former two are independent of the order of reflection, while the third one increases with the order (n).

The relationship between b_3 and b_{size}, b_{inst} and b_{dis} depends on the profile of individual components that give rise to the corresponding widths. The meridional component (from which b_3 is extracted) is well approximated by a Gaussian distribution (equation 3.1) for the measured system, and we may assume that profiles of individual broadening effects are also Gaussian. Therefore (90, 91),

$$b_3 = \sqrt{b_{size}^{\ 2} + b_{inst}^{\ 2} + b_{dis}^{\ 2}} \tag{3.10}$$

where b_{size} and b_{inst} are both constants, and b_{dis} varies linearly with n if the lattice disorder is of the "strain" type (92, 93) or varies with n^2 if it is of the 1D "paracrystalline" type (93). "Strain" refers to the statistical fluctuation of L spacing from fibril to fibril whilst the periodic packing of individual fibrils is perfect. And "paracrystalline" disorder deals

with the deviation of lattice points from their ideal positions within individual fibrils. If there is only one type of lattice distortion present, equation (3.10) will become

$$b_{3,n} = \sqrt{b_{size}^{\ 2} + b_{inst}^{\ 2} + A'n^2} \qquad \text{“Strain” only} \tag{3.11}$$

$$b_{3,n} = \sqrt{b_{size}^{\ 2} + b_{inst}^{\ 2} + A''n^4} \qquad \text{“Paracrystalline” only} \tag{3.12}$$

where $b_{3,n}$ is the b_3 for the n^{th} order of meridional reflection, A' and A'' are proportional constants.

However, lattice distortions in collagen fibrils are more complicated and should include “strain”, “paracrystalline”, and/or other types of disorder. Therefore, neither equation (3.11) nor equation (3.12) can solely describe the measured peak width along meridional direction (b_3). When more than one type of disorder is present, to our knowledge, there is no simple analytical solution that can incorporate individual contributions from different disorders to the overall peak broadening. Instead, we find the measured b_3 as a function of the order of reflection can be well fitted by quadratic functions (shown in Fig. 3.7)

$$b_{3,n} = b_{3,0} + B'n + B''n^2 \tag{3.13}$$

where B' and B'' are fitting parameters. The intercept $b_{3,0}$ is free of broadening by disorders. If the instrumental broadening can be neglected, $b_{3,0} = b_{size}$, and the longitudinal coherence length

$$l_c = 1/b_{size} \approx 1/b_{3,0} \tag{3.14}$$

Otherwise, $b_{3,0}$ includes both b_{size} and b_{inst} and equation (3.14) gives the lower limit of the longitudinal coherence length.

It should be noted that the longitudinal coherence length obtained in this work (~ 1010 nm) is different from the one (~ 31.2 nm) determined by Fraser *et al.* (33). Their "coherence length" was determined from layer-lines and row-lines on WAXD patterns and was mainly related to the high-resolution features of collagen structure, e.g., peptide repeats in α chains. On the other hand, the present longitudinal coherence length is determined from the equidistant meridional reflections on SAXS patterns and is mainly related to the low-resolution features of collagen structure, e.g., the *L* stagger of molecules in the fibril axis direction. Thus, it is understandable that the coherence length estimated in this work is about 30 times larger than the one estimated by Fraser *et al.* (33).

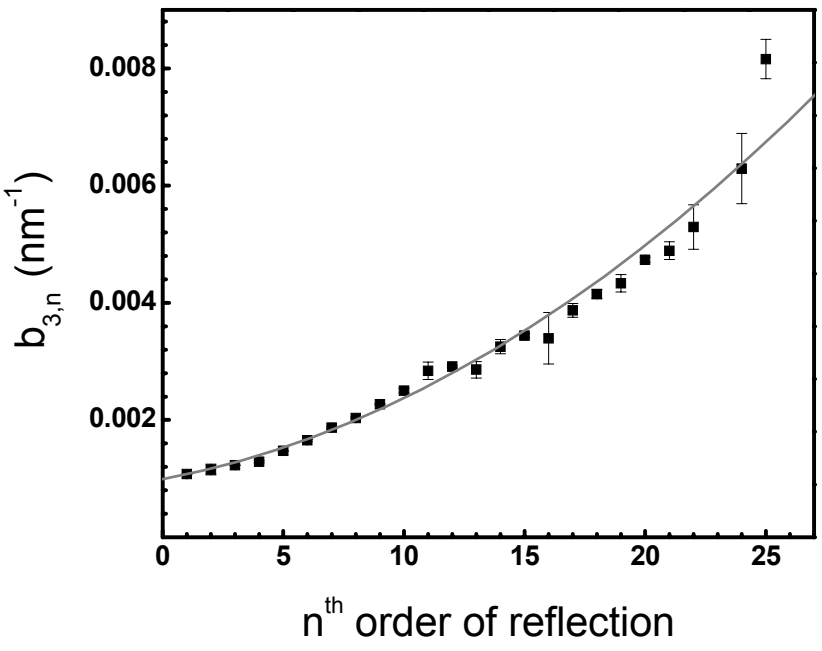

Figure 3.7 Longitudinal integral width b_3 vs. order. An empirical function $b_{3,n} = b_{3,0} + B'n + B''n^2$ is used to fit b_3 for different orders. Parameters giving the best fit are $b_{3,0} = 9.91 \times 10^{-4}$, $B' = 7.73 \times 10^{-5}$, $B'' = 6.11 \times 10^{-6}$. $b_{3,0}$ does not contain disorder effect and can be used to estimate the longitudinal coherence length by the Scherrer formula if

instrumental broadening is negligible. However, for present analysis, the contribution from instrumental broadening is unknown hence the longitudinal coherence length cannot be precisely determined. But its lower limit is $1/b_{3,0} \sim 1010$ nm.

3.5 Conclusion

We have presented a quantitative analysis of the small-angle equidistant meridional reflections from fish bone collagen fibrils, taking preferred orientation and other effects into account. It involves the separation of preferred orientation and fibril size effects and was then applied to analyze the 2D intensity profile of meridional reflections. Based on this procedure, we obtained the orientation distribution and average diameter of fibrils, the axial period, and the properly integrated intensities. The simultaneous fitting procedure of several peaks to an analytical model that depends on only very few parameters leads to highly reliable and consistent data with appropriate error propagation.

Chapter 4. Lateral Packing of Mineral Crystals in Bone Collagen Fibrils

4.1 Introduction

The mineral phase in bone has two major functions (1, 7, 17). On the one hand, it serves as an ion reservoir, which can rapidly maintain, in the extracellular fluid, appropriate concentrations of calcium, sodium, magnesium, phosphate and other ions that are critical for many physiological functions and biochemical reactions. On the other hand, in combination with the organic matrix components (predominantly type I collagen fibrils), within which the mineral phase is embedded, an elegantly arranged three-dimensional (3D) ultrastructural composite material that is both lightweight and extremely tough is formed. Both physiological and mechanical functions of bone are affected by the exact size, shape, chemical composition and crystal lattice structure of the mineral crystals (1, 3), by their specific spatial distribution and orientation within the collagen fibrils, and by the degree of mineralization. For instance, the function of the bone composite serving as an ion reservoir requires that the mineral phase must be resorbable very quickly in the body, which is best achieved if the mineral assumes the shape of nanoscale crystals with large surface-to-volume ratios. Furthermore, the particular spatial arrangement of the composite material at all levels of the anatomical hierarchy of bone substance, viz., the gross, microscopic, ultrastructural and molecular levels, provides the specific mechanical properties required to resist many different forces and stresses applied to specific regions of a particular bone as an organ, tissue and substance without structural failure (1).

After decades of intensive study, it is now clear that the very earliest calcium phosphate solid phase within the collagen fibrils are irregularly shaped, very thin "dots" (23), typically as small as ~ 1 nm or less (94). Soon after nucleation, crystal growth occurs and the habit of the mineral crystals changes to very thin, long platelets (9, 94). The changes in crystal habit and size are also accompanied by an increase in "crystallinity". Needle-shaped crystals were also proposed to be present in bone substance but have since been confirmed to actually be the edge-view of the platelets (for a review, see (1)).

Note that the properties of the mineral crystals also vary as a function of the local rate of bone formation and resorption (bone substance turnover), which in turn determines the age of the crystals locally, viz., the period of time the crystals remain in the bone substance after their initial deposition (3, 95). Regions of rapid bone turnover can be located immediately adjacent to regions of very slow bone turnover, with the result that the crystals of adjacent sites at specific microscopic regions of the bone substance may vary greatly in size, shape, local crystal structure, and physical-chemical properties.

The arrangement of mineral crystals along the axis of a collagen fibril, within which they are deposited, mirrors the periodic repeat (ca. 67 nm) present in uncalcified collagen fibrils. These periodic repeats can be visualized by the banding pattern observed in transmission electron microscopy (TEM). Small-angle X-ray scattering (SAXS) measurement has shown that the equidistant meridional reflections with a long period of ca. 67 nm are preserved for the mineralized collagen fibrils of bone for various lengths of time after mineralization is initiated (25, 26, 81). However, as the concentration of

mineral crystals within the collagen fibril increases with time, the 67 nm repeat is gradually obliterated, as observed by TEM (95), as well as by SAXS in the form of decreasing number of meridional reflections. The distortion of the original 3D supramolecular packing of collagen molecules in the fibril is also apparent from TEM of very thick ground sections of fully calcified compact bone where the mineral phase occupies the full axial period (96) and where eventually both the "free" volume within the "hole regions" and the additional volume within the "overlap regions" are filled with mineral crystals (22).

Little is known about the packing of mineral crystals in the radial direction of the collagen fibril. In electron microscopic studies, individual crystals in tissue sections are difficult to resolve because they are extremely thin, and the collagen fibrils embedding the crystals are densely packed, especially in the heavily mineralized regions of bone. Although electron microscopic tomography and image reconstruction have been utilized to study the 3D spatial arrangement of mineral crystals within the fibril (47), the resolution of this technique (4–6 nm) is well above what is needed to resolve the thickness of mineral platelets.

For more statistically relevant information of crystal dimensions and spatial orientation in a specific volume of bone, the use of SAXS remains more suitable. Several attempts have been made to investigate the lateral packing of the mineral crystals in collagen fibrils based on the analysis of the small-angle near-equatorial diffuse scattering feature (24, 25, 61, 71, 97). However, a proper analysis of the scattering data should take into account *a priori* real space information obtained from other techniques, such as TEM and atomic force microscopy (AFM). The models developed by those authors (24, 71)

assume that the mineral crystals have needle-like or irregular shapes and are randomly distributed in the cross-section of the fibrils, which is inconsistent with the known platelet nature of the mineral crystals (9-12). Furthermore, a random distribution within the fibril cross-section of the anisotropic platelet cross-sections must not allow platelet overlap and, thus, is only feasible if the degree of mineralization is very low.

In this chapter, the characteristic "butterfly pattern" originating from the lateral arrangement of the apatite crystals was analyzed in terms of disordered lamellar stacks of platelet-shaped crystals, intercalated with organic layers having a thickness of a few collagen molecules (see Fig. 4.1a). This model is more consistent with TEM observations (18, 47, 98, 99). The thickness distributions of adjacent mineral and organic layers are assumed to be statistically independent, so that the treatment of a one-dimensional density profile along the layer normals (which are preferentially oriented perpendicular to the main fibril axis) resembles the one-dimensional hard-rod fluid model of Zernike and Prins (100) with certain modifications to be discussed below. Preferred orientation effects leading to the actual "butterfly pattern" are taken into account (75, 76, 101). The analysis leads to the thickness distributions for both the mineral platelets and the intercalated organic layers, the orientation distribution of the mineral stacks, and an estimate for the average height of the mineral crystals, i.e., the dimension parallel to the fibril axis which is known to coincide with the crystallographic *c*-axis. The information about the size, shape, preferred orientation, and separation between adjacent crystals is essential for a comprehensive understanding of the 3D spatial relationship between the mineral crystals and their surrounding collagen matrix, on which the mechanical properties and the physiological and biological functions of bone strongly depend.

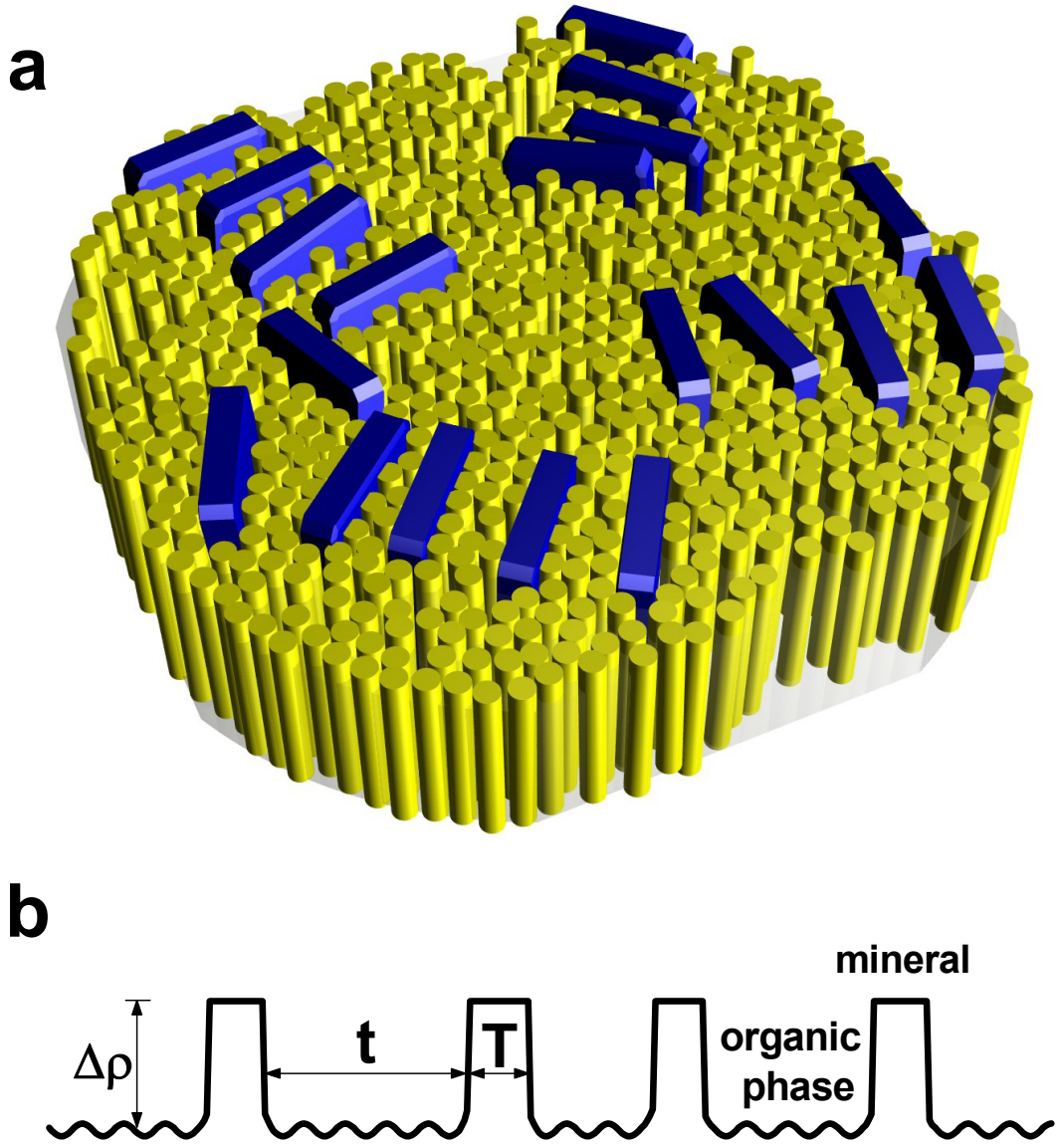

Figure 4.1 (a) Schematic illustration of the lateral packing of mineral crystals in the collagen matrix. Thin apatite platelets are aligned nearly parallel within the stacks. The thickness of crystals is typically 2 nm and the width is about 20 nm. The crystal height in the c-axis dimension (preferentially aligned about the fibril axis, not visible in this figure) is about 30 nm. Courtesy to Dr. Christian Burger. (b) Electron density projected onto the normal of a stack of mineral platelets. *T* is the thickness of individual crystals, and *t* is the thickness of organic layers between the neighboring crystals. The density of the mineral phase can be assumed to be uniform. There are small density fluctuations in the organic phase but their order of magnitude is much smaller than the density contrast ($\Delta\rho$) between the mineral phase and the organic phase.

4.2 Principles and Methods

The 3D collagen/mineral superstructure has been reviewed in previous chapters. A schematic representation of the fibril cross-section through the "hole region" is shown in Fig. 4.1a, illustrating the lateral packing of the mineral crystals in the collagen matrix. In this representation, apatite crystals with a typical height of ca. 30 nm in the *c*-axis dimension, ca. 20 nm in width, and 2 nm in thickness (9, 10) are arranged into irregular arrays (18, 47). Since the average width and height of a crystal are much larger than its thickness, each apatite platelet could be approximated by an infinitely large plate. Under this approximation, the calculation of the scattering intensity from an individual stack of mineral crystals is reduced to a 1D problem, depending only on the 1D density profile projected onto the layer normal direction, as shown in Fig. 4.1b. The stack can be treated as a two-phase system, one phase being the mineral crystal domain with a large but uniform electron density, and the other being the organic matrix layers embedded between the adjacent crystals. Due to the density difference between collagen molecules and the surrounding fluid within the fibrils, small density fluctuations are expected within the organic matrix layers (but not in the mineral phase), which could give rise to a scattering background more prominent at larger scattering angles. At the present length scales, the organic domains can be considered as homogeneous, confirming the notion of a two-phase system with two homogeneous domains. Furthermore, the density can be assumed to undergo an abrupt change at the mineral/organic phase boundaries so that corrections for a finite density transition profile are not necessary. A theoretical treatment for the scattering from an equivalent system, namely that of the 1D hard-rod fluid, was first given by Zernike and Prins (100). Later, Hermans (102) generalized it for arbitrary

thickness distributions and formulated a more elegant expression based on a summable convolution series,

$$I_{1D}(s) = \frac{f}{s^2}\,\mathrm{Re}\{\frac{[1-H_1(s)][1-H_2(s)]}{1-H_1(s)H_2(s)}\} \tag{4.1}$$

where $I_{1D}(s)$ is the intensity in 1D reciprocal space ($s = 2\lambda^{-1}\sin\theta$ is the absolute value of the scattering vector, λ is the wavelength and 2θ is the scattering angle), s is restricted to the direction normal to the layers of the stack, f is a proportionality constant related to the 1D Porod asymptote at large s (i.e., $f = \lim_{s\to\infty} s^2 I_{1D}(s)$), Re{} takes the real part of a complex number, $H_1(s)$ and $H_2(s)$ are the 1D complex Fourier transforms of the thickness distributions of the two components. Note that equation (4.1) implies an infinite length of the stack in the layer normal direction, i.e., the number of mineral plates in the stack is approximated as infinitely large. A finite number of mineral plates could be introduced, but it would be difficult to separate its effect from that of stacking disorder, unless the scattering curve shows higher order maxima, which is not the case for the present system.

A TEM study on the lightly mineralized regions of intramuscular herring bone showed that apatite crystals appear to have nearly uniform thickness (18). Therefore, we chose a narrow Gaussian for the distribution of thickness of mineral crystals:

$$p_1(T) = \frac{1}{\sqrt{2\pi}\sigma_{\mathbf{T}}}\exp(-\frac{(T-\langle T\rangle)^2}{2{\sigma_{\mathbf{T}}}^2}) \tag{4.2}$$

where $p_1(T)dT$ is the probability of finding a crystal with thickness between T and $T + dT$, $\langle T\rangle$ is the average thickness, and $\sigma_{\mathbf{T}}$ is the standard deviation of the thickness

distribution. As a probability density distribution, equation (4.2) is normalized to unity integral. The 1D Fourier transform of $p_1(T)$ is thus

$$H_1(s) = \exp(2\pi i\langle T\rangle s - 2\pi^2 \sigma_{\mathrm{T}}{}^2 s^2) \tag{4.3}$$

TEM images also show that the separations between adjacent crystals, i.e., the thickness of the intercalated organic layers have a relatively broader distribution (18). A Gamma distribution was chosen for the thickness distribution of organic layers:

$$p_2(t) = \Gamma(v)^{-1} a^{-v} t^{v-1} \exp(-t/a) \tag{4.4}$$

where $p_2(t)dt$ is the probability of finding an organic layer with thickness between *t* and *t*+*dt*, $\Gamma(v)$ is the Gamma function of argument *v*, *v* is a dimensionless parameter, and *a* is a parameter with the dimension of a length. The average thickness of organic layers $\langle t\rangle$ is given by $\langle t\rangle = av$, and the standard deviation of the distribution is $\sigma_{\mathrm{t}} = a\sqrt{v}$. Equation (4.4) is also normalized. The 1D Fourier transform of $p_2(t)$ is

$$H_2(s) = (1 - 2\pi i a s)^{-v} \tag{4.5}$$

Assuming the presence of simple fiber symmetry, the scattering intensity of a perfectly oriented system of stacks, randomly aligned with their layer normals pointing perpendicular to the fiber axis direction, can be written as

$$I(s_{12}, s_3) = \frac{1}{\pi s_{12}} I_{1D}(s_{12}) I_3(s_3) \tag{4.6}$$

where s_{12} and s_3 are components of the reciprocal space vector $\vec{s}$ with $|\vec{s}| = \sqrt{s_{12}^2 + s_3^2}$, s_{12} is perpendicular to the fiber axis and s_3 is in the fiber axis direction. A normalization factor $(2\pi s_{12})^{-1}$ results from the circular average, another factor 2 from $I_{1\mathrm{D}}$ touching the averaging circumference at two points, and the longitudinal component $I_3(s_3)$ depends

on the averaged size, shape and possible correlation of the crystals in the fiber axis direction. We found that a Lorentzian function gives the best fit to the measured 2D intensity profile,

$$I_3(s_3) = \frac{1}{w_3} \frac{1}{1 + \pi^2 (s_3 / w_3)^2} \tag{4.7}$$

where w_3 is the integral peak width, and its reciprocal value w_3^{-1} is used as an estimate of the average crystal height *H*, assuming that there is no strong correlation from a stack in one hole zone to the stacks in the neighboring hole zones along the fibril axis.

Considering the preferred orientation effects, the *c*-axes of the apatite crystals are preferentially oriented along the primary bone axis, as indicated by the arc-shaped (002) reflection on the meridian of wide-angle X-ray diffraction (WAXD) patterns (6, 25, 26, 103). Note that the preferred orientation observed by WAXD is a superposition of the preferred orientation of the fibrils with respect to the bone axis and that of the *c*-axes of mineral crystals with respect to the axis of the associated fibril (3, 6). The latter is usually identified by electron diffraction from individual mineralized collagen fibrils (6, 18). The orientation studied by SAXS analysis is similar to that by WAXD, i.e., it refers to the overall orientation of mineral crystals with respect to the bone axis. When taking this preferred orientation into account, scattering from all stacks will no longer be a thin streak on the equator, but spread into a characteristic "butterfly pattern" (shown in Fig. 4.2). The resulting fiber-averaged intensity distribution, $J(s,\varphi)$, is given by (75, 76),

$$J(s,\varphi) = \int_0^{\frac{\pi}{2}} I(s,\varphi') F(\varphi,\varphi') \sin\varphi' d\varphi' \tag{4.8}$$

where $I(s,\varphi')$ is the intensity distribution for the perfectly oriented system (equation 4.6) translated into polar coordinates, and $F(\varphi,\varphi')$ is related to the orientation distribution of the stacks. A detailed analysis and application of equation 4.8 can be found in a separated paper (101).

4.3 Experimental

Native intramuscular shad/herring bones were used for all experiments. The bone specimen has roughly a fiber shape with a diameter ca. 0.5 mm. Information about the sample preparation, X-ray instrumentation, and image processing has been described in previous chapters. In addition to the imaging plates (IP), a CCD X-ray detector (MarUSA) was also used to record selected SAXS patterns in order to confirm the absence of detector-related systematic errors.

The "butterfly pattern" was fitted after removing regions that contain meridional reflections. An analytical background was incorporated into the 2D fitting scheme since it cannot unambiguously be separated from the diffuse scattering that is of interest. Various functions (constant, plane and etc.) were tested and it was found that the background shape had a relatively small effect on the final results. The best fitting quality was achieved when an elliptically stretched Pearson type VII function was used (*n* was fixed at 12 during the fitting).

$$background = \frac{c_0}{(1 + c_1 s_{12}^2 + c_2 s_3^2)^n} \tag{4.9}$$

TEM cross-sectional images were obtained in a JEM-2011 microscope (JEOL, Japan). Bone samples were fixed in 0.1 M sodium cacodylate-buffered 4% paraformaldehyde and 2% glutaraldehyde solution for 24 h at 4 °C, and then subsequently fixed in 1% osmium

tetroxide solution for 2 h at 4 °C. After being dehydrated through a series of 50%, 70%, 85%, 95%, 100% ethanol, the samples were infiltrated in 1:1 LR White resin (Ted Pella Inc., Redding, CA) dissolved in ethanol for 24 h and then vacuum-infiltrated with pure LR White. The recovered samples were then embedded in fresh LR White resin (Ted Pella Inc., USA) for 24 h at 50 °C. Silver to golden thin sections, prepared by using an ultramicrotome (RMC model MT-X, Boeckeler Instruments Inc., Tucson, AZ), were collected on parlodion-coated grids (Ted Pella), and air-dried. The microtomed sections were typically 70 nm in thickness; therefore, they contained no more than two "hole regions" in the fibrils axis direction.

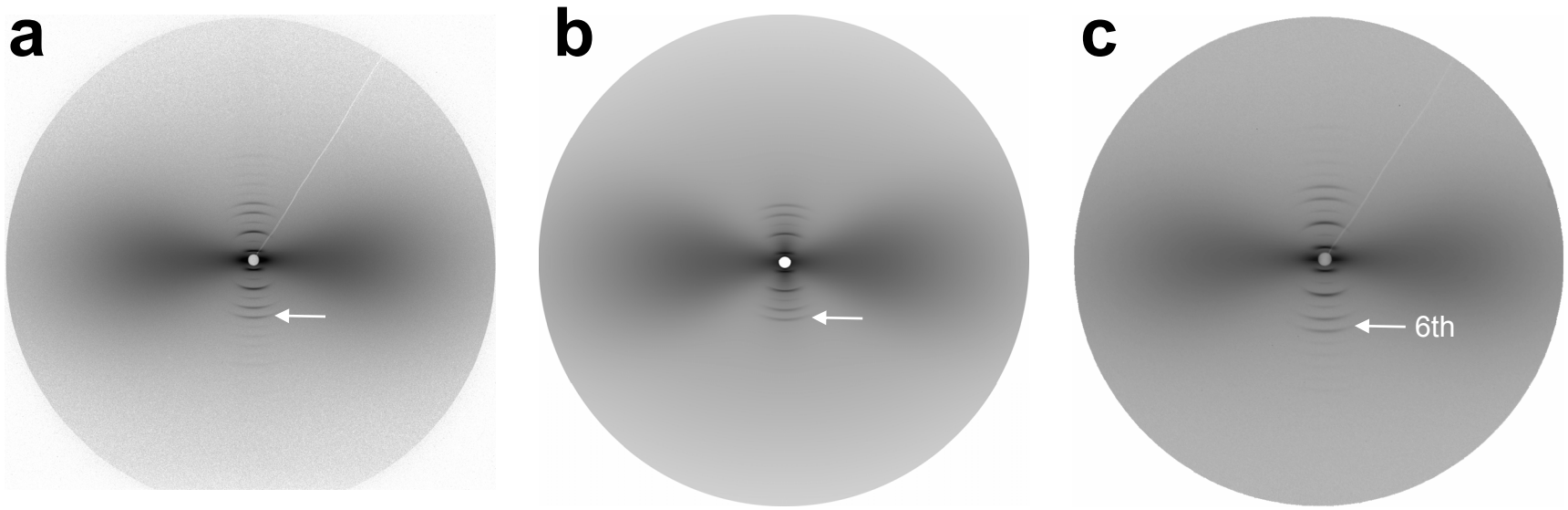

Figure 4.2 (a) Measured 2D SAXS pattern from intramuscular shad bone by imaging plate. Sample-to-detector distance was 1897 mm and the measurement range covered s = 0.01 ~ 0.38 nm^{-1}. Bone axis is in the vertical direction (s_3, meridian). The equator s_{12} is perpendicular to the bone axis. (b) Calculated pattern for (a). The total intensity is a combination of the fan-shaped diffuse scattering originating from the lateral packing of mineral crystals in organic matrix (this Chapter), and sharp meridional reflections originating from periodic packing of collagen molecules and mineral crystals along the fibril axis (Chapter 3). The corresponding fitting parameters are listed in Tab. 4.1 and 4.2. (c) Diffraction pattern from the same irradiated volume as (a) but recorded with a CCD camera. Sample-to-detector distance was 1942 mm and the measurement range covered s = 0.01 ~ 0.30 nm^{-1}. The white arrows in patterns indicate the 6th order meridonal reflections. The axial period of the equidistant meridional reflections is about 67 nm.

4.4 Results and Discussion

Fan-shaped diffuse scattering profiles in 2D SAXS patterns from heavily mineralized intramuscular shad/herring bones were analyzed using the approaches described above. The fitting results were used to calculate a "butterfly pattern" (Fig. 4.2b). The calculated pattern has faithfully reproduced the features of the measured pattern, as indicated more clearly in the 3D relief plots viewed from different perspectives (Fig. 4.3). Fig. 4.3a is viewed from the meridional direction (from bottom to top) so it shows the lower half of the "butterfly". The fitting quality in the equatorial direction is inspected in this plot. It is shown that the fitted plot has an excellent match-up to the measured intensity, which is important because the intensity distribution in the equatorial direction contains the information of our interest, i.e., the thickness distribution of mineral crystals and organic layers (equations 4.1 and 4.8). Fig. 4.3b is viewed from the equatorial direction (from left to right) and it shows the right half of the "butterfly". The measured intensity data are evenly distributed on both sides of the simulated surface plot. In addition to the diffuse scattering from the lateral packing of mineral phase, meridional reflections from the periodic structure of striated fibrils were also analyzed and simulated by a scheme described in Chapter 3.

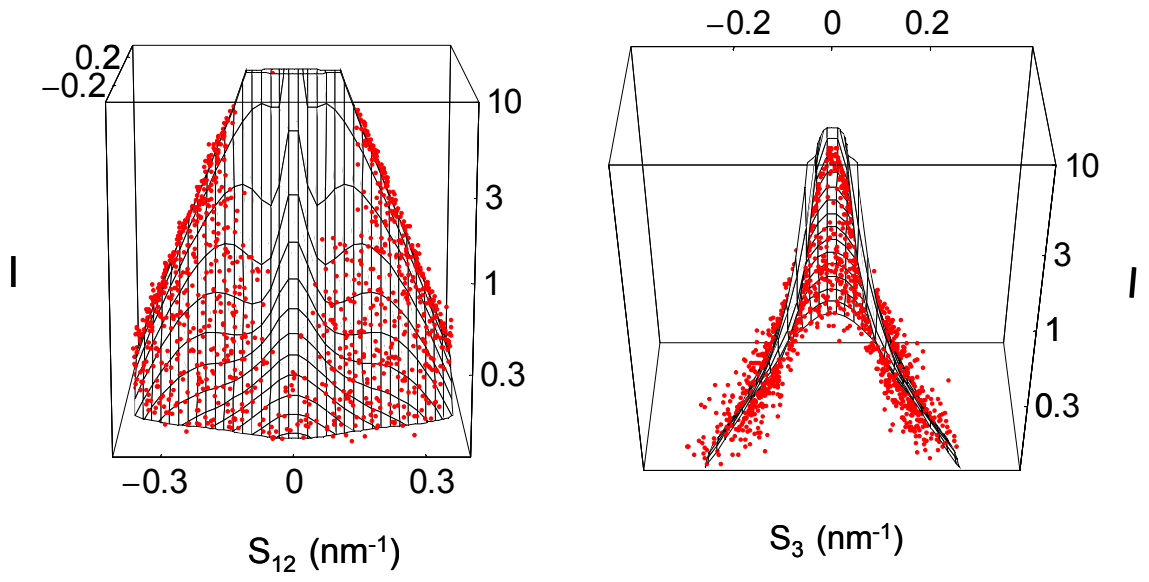

(a) (b)

Figure 4.3 3D relief plots showing the experimental intensity data points (discrete dots) and the fitted model (continuous mesh), viewed perpendicular (a) and parallel (b) to the equator.

Evaluation of the Effect of Different Detectors. Prior to performing quantitative analysis of the SAXS patterns, it is necessary to measure the intensity values accurately. The ideal detecting system, which includes the detector and the readout device, should output an intensity value that is proportional to the absorbed X-ray intensity. Conventional X-ray film is not suitable for quantitative analysis because of its narrow dynamic range, poor linearity, and large uncertainty for the readout intensities. Usage of imaging plates (IP) has greatly improved the quality for intensity measurement and hence the reliability of quantitative X-ray analysis. It was reported that the ultimate precision in intensity measurements with IP is of the order of 1% (104). However, no data is available to show how significant this uncertainty is for the subsequent analysis. Direct determination of the detector effect is usually difficult. Instead, we have recorded SAXS

patterns from the same sampling volume with two types of detectors (IP and CCD) that have completely different working mechanisms. Analysis of the patterns acquired with IP (Fig. 4.2a) and CCD (Fig. 4.2c) generates two sets of structure parameters for exactly the same sampling volume. The results are compared in Tables 4.1.

Table 4.1 Comparison of the fitting results for SAXS patterns from the exact same sampling volume but recorded on different detectors.

(a) Integrated intensities of *meridional* reflections[1]

Order	Imaging Plate	CCD Camera
1	100.0(9)	100(1)
2	0.9(1)	0.4(1)
3	28.5(3)	28.0(4)
4	1.4(1)	1.0(1)
5	7.5(2)	7.1(2)
6	6.1(2)	5.9(2)

[1] Scaling is such that the 1st orders are equal to 100.

(b) Other parameters obtained by fitting *meridional* diffraction patterns

	Imaging Plate	CCD Camera
[2] Hermans' orientation factor	0.928(2)	0.927(1)
Average fibril diameter (nm)	64(1)	65(1)
Long period (nm)	66.8(1)	67.2(1)
Coherence length (μm)	0.97(2)	0.56(1)

[2] This is the orientation distribution of collagen fibrils with respect to the primary bone axis.

(c) Structure parameters obtained by fitting the "*butterfly*" patterns. ⟨*T*⟩ – average thickness of mineral crystals, σT – width of the thickness distribution of mineral crystals, ⟨t⟩ – average thickness of organic layers, σt – width of the thickness distribution of organic layers, H – average length of crystals in the c-axis dimension.

Detectors	[3] Hermans' orientation factor	<*T*> (nm)	σ_T (nm)	<*t*> (nm)	σ_t (nm)	*H* (nm)
Imaging Plate	0.844(1)	1.91(1)	0.04(1)	5.38(3)	3.13(2)	55.6(6)
CCD Camera	0.855(1)	1.95(2)	0.05(1)	5.33(6)	3.17(4)	61(2)

[3] This is the orientation distribution of apatite platelets (or stacks) with respect to the primary bone axis.

Tables 4.1*a* and 4.1*b* list the results from fitting of the meridional reflections. After normalization to the 1st order reflection, the two sets of integrated intensities are in good agreement with each other, especially for the strong 3rd, 5th, and 6th orders. Weak orders (2nd and 4th) show relatively larger deviations, probably because they are more sensitive to the non-perfect background treatment. The Hermans' orientation factor, long period, and the average lateral fibril size (Table 4.1*b*) are also consistent with results using different types of detectors. However, the coherence length estimated from the longitudinal integral width of zero order ($b_{3,0}$) has about a 40% difference. We ascribe this difference to the broadening effect to the finite pixel size of the detector and to electronic broadening effects. The CCD detector has a larger pixel size than the imaging plate, so that the meridional reflections are broadened more severely when they are recorded on the CCD. Therefore, the $b_{3,0}$ value determined from meridional reflections by using the CCD detector is overestimated and the corresponding coherence length (l_c =

$1/b_{3,0}$) is underestimated. In the present analysis, the situation is further aggravated since the $b_{3,0}$ value (2~3 pixels) is approaching the spatial resolution limit of the detectors.

Table 4.1c lists the structure parameters extracted from the fan-shaped near-equatorial diffuse scattering. The fitting scheme is based on the one developed in this paper. Again, diffraction patterns recorded on different detectors produced very similar results. The good agreement between the two sets of structural information (from IP and CCD) not only suggests that the intensity measurement is precise and the possible detector effect is insignificant to the fitting results, but more importantly, the analytical schemes used to obtain these parameters are self-consistent.

Mineral Packing in Collagen Matrix. Table 4.1c lists the structure information about the mineral packing in the collagen matrix. For heavily mineralized intramuscular shad bone, the average thickness of apatite platelets $\langle T \rangle$ is about 1.9 nm, which is just slightly larger than the breadth of the inter-microfibrillar "channels" found in herring/shad bones (~ 1.5 nm, see Chapter 2). The thickness distribution for mineral crystals is very narrow (σ_T ~ 0.04 nm, from IP), indicating that apatite platelets have a nearly uniform thickness. The above information strongly suggests that at least initially the lateral growth of apatite crystals is confined within the "channels". The large crystal thickness measured by electron microscopy tomography (~ 4-6 nm for calcified turkey leg tendon) (47) is very likely to be overestimated, since it will cause strong perturbations to the surrounding matrix structure.

The thickness of intercalated organic layers between adjacent apatite platelets is described by a gamma distribution (solid line in Fig. 4.4). The mean value of this

distribution $\langle t \rangle$ is ca. 5.4 nm and the standard deviation σ_t is ca. 3.1 nm. These values are intrinsic properties of the mineral packing in the collagen matrix and should be independent of the form of the distribution. Thus, if another function is also a good approximation for the statistics of intercalated organic layers, using it to replace the gamma distribution in equation (4.4) should predict similar fitting results for $\langle t \rangle$ and σ_t. One of the possible selections is Gaussian, a function widely used in the literature to treat scattering from polymeric lamellar structures (93). Table 4.2 lists the fitting results when assuming the thickness distribution of organic layers obeys Gaussian. However, large deviations were shown for the $\langle t \rangle$ and σ_t values from the case that assumes a gamma distribution. The profile of Gaussian distribution was plotted in Fig. 4.4 (grey, dash line) using the parameters in Table 4.2. A portion of t falls into the negative region, which is obviously incorrect since the thickness of an organic layer cannot have negative values. Thus, we conclude that the gamma distribution is a more suitable description for the thickness distribution of intercalated organic layers.

From Table 4.2, one can estimate the "pseudo-periodicity" of the lamellar structure by adding the average thickness of mineral crystals $\langle T \rangle$ to that of organic layers $\langle t \rangle$. The sum is about 7.3 nm for heavily mineralized intramuscular shad bone. Should the thickness of organic layers have a very narrow distribution, the alternate packing of the two phases in a stack will form long-range order, and one would expect a sharp peak at the position of 7.3 nm, or ca. 0.14 nm^{-1} in the reciprocal space. However, the organic layers have a broad thickness distribution in the real case, resulting in a very weak correlation for the mineral packing in stacks. Therefore, instead of a sharp, narrow peak, we observed a weak, broad "shoulder" on the diffraction patterns (as shown in the

contour lines in Fig. 4.3*a*). However, it should be noted that the weak "shoulder" still indicates some extent of correlation for the mineral packing in the collagen matrix. The lateral arrangement of the apatite platelets cannot be completely random.

Table 4.2 Comparison of the fitting results by assuming different distributions for the thickness of organic layers. The corresponding "butterfly" pattern was shown in Fig. 4.2a. The first row is for Gaussian distribution, and the second row is for Gamma distribution.

Organic phase distribution	[1] Hermans' orient. factor	⟨T⟩ (nm)	σ_T (nm)	⟨t⟩ (nm)	σt (nm)	H (nm)
$p_2(t) = \frac{1}{\sqrt{2\pi}\cdot\sigma_t}\exp(-\frac{(t-<t>)^2}{2\cdot\sigma_t^{\,2}})$	0.841(1)	1.92(1)	0.02(1)	3.16(2)	2.40(1)	71.0(9)
$p_2(t) = \Gamma(v)^{-1}\cdot a^{-v}\cdot t^{v-1}\cdot\exp(-t/a)$	0.844(1)	1.91(1)	0.04(1)	5.38(3)	3.13(2)	55.6(6)

[1] This is the orientation distribution of apatite platelets (or stacks) with respect to the primary bone axis.

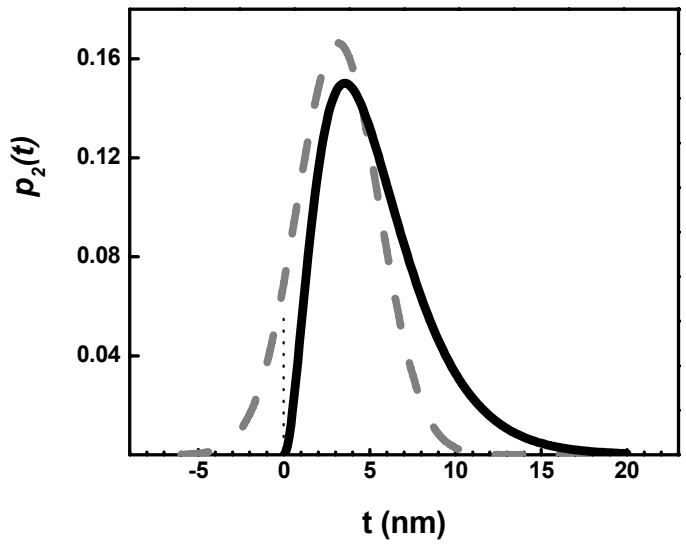

Figure 4.4 Comparison of two types of length distribution of organic layers. The Gamma distribution is shown in black, solid line (—) and the Gaussian distribution is shown in grey, dash line (---). A portion of t has negative values in the Gaussian distribution.

Comparison with TEM Results. TEM cross-section images (Fig. 4.5) for the lightly mineralized collagen fibrils indicate that apatite crystals have large width-to-thickness aspect ratios. This observation is consistent with the platelet shape in the 3D space when taking the height of crystals (~ 30 nm) into account. The mineral platelets are packed into irregular arrays or stacks within the collagen fibrils. The width of the mineral crystals measured from TEM images shows a range from 10 nm to 50 nm, with an average value ca. 30 nm. The results also agree well with early measurements for isolated bone apatite crystals (10). However, a quantitative evaluation of the mineral crystal thickness from TEM data is difficult. For instance, the *c*-axes of the mineral crystals show a preferred orientation with respect to the axis of the associated fibril and, thus, cannot be aligned to the electron beam simultaneously (1, 6, 18). When the *c*-axis of a crystal is not parallel to the electron beam, the profile of the crystal projected onto the TEM image (showing as a dark line) will become thicker, especially in the thickness dimension. Therefore, direct measurement for the crystal thickness from a TEM cross-sectional image will get overestimated values. Fig. 4.5 shows that the short dimension of the dark lines ranges from 2.1 nm to 3.3 nm, which is larger than the average crystal thickness (~ 1.9 nm) determined from the SAXS analysis. Giving an average crystal height of ca. 30 nm, the tilt of the crystallographic *c*-axes to the electron beam is estimated (1° − 4°). This value is significantly smaller than the one determined by electron microscopic tomography (15° − 20°, see (47)), making sure that our assumption for the parallel arrangement of mineral platelets in a stack is a good approximation. Instead of measuring the thickness of the organic layers directly, we estimated the center-to-center distance between adjacent crystals, i.e., the summation of a crystal thickness *T*

and that of an embedded organic layer *t*. The results show a broad distribution (3.5 nm − 10.4 nm) but is also in good agreement with the XRD analysis (~ 7.3 nm on average).

Limitations of the Model The present analytical scheme is suitable for the case of platelet-shaped apatite crystals packed into near-parallel arrays. The width and height of the crystals must be significantly larger than the thickness so that the approximation of infinitely large plates is well justified. This condition is satisfied for chicken, bovine, mouse, herring, and other species, based on the TEM study of isolated crystals (10) and the tissue sections in this work.

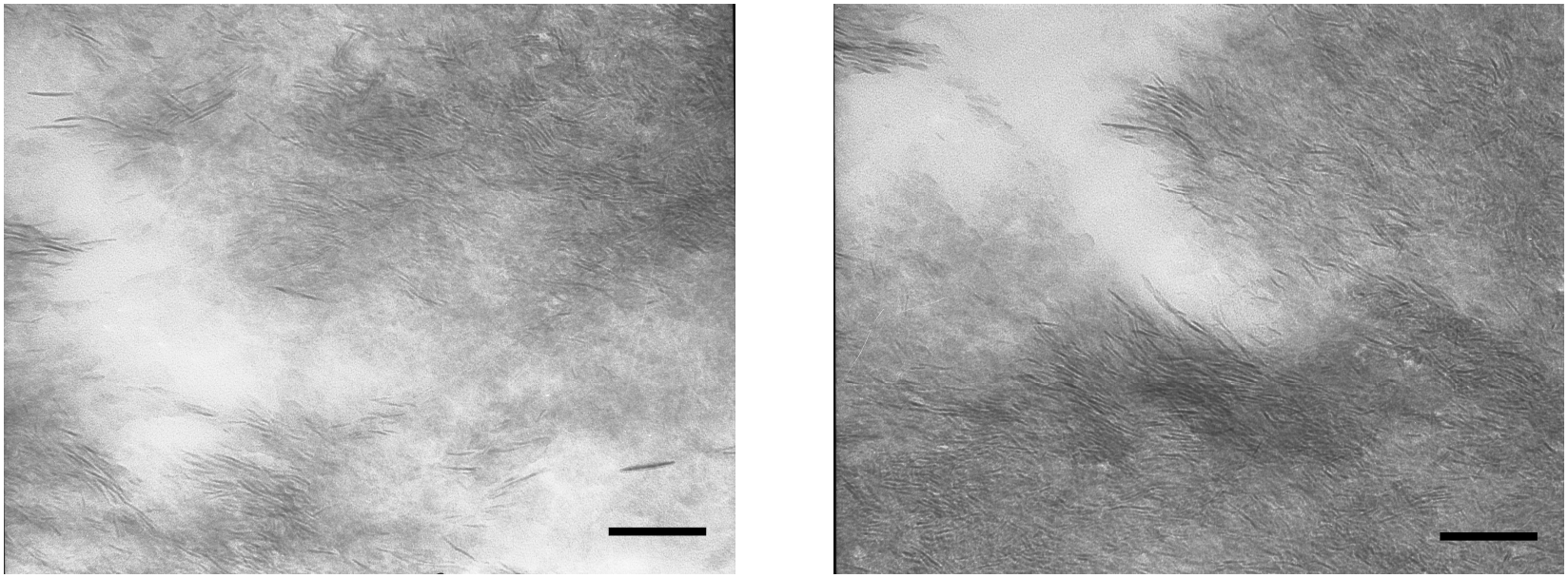

Figure 4.5 TEM images of lightly mineralized intramuscular herring bone. Platelet-shaped mineral crystals are shown as dark lines in the cross-section of the fibrils and form near parallel arrays schematically shown in Fig. 4.1. The scale bar is 100 nm. Courtesy to Dr. Hao Wang.

4.5 Conclusions

In summary, we have developed an effective method to evaluate the lateral packing of mineral crystals in the collagen matrix via quantitative analysis of the "butterfly pattern" in small-angle X-ray scattering of intramuscular shad/herring bones. We obtained the thickness distributions for both mineral platelets and intercalated organic layers embedded between them, hence providing more comprehensive information about the spatial arrangement of the mineral phase in the collagen matrix. Such 3D structural information, together with the total volume fraction of the mineral phase, provide much better insights into the structure-property relationships than, e.g., solely the degree of mineralization as presently used in many studies (3). The information obtained in this work can also be used to refine the much simplified 1D structural models developed for calcified collagen fibrils (105), and to find a more precise relationship between the collagen/mineral superstructure and its mechanical properties (13, 14). Additionally, we expect it will eventually allow investigations of possible changes in the spatial arrangement of the collagen matrix and embedded mineral phase for bones in pathological conditions.

Chapter 5. Maturation and Mineralization of Bone Collagen Fibrils

5.1 Introduction

Bone formation and development (osteogenesis) is a dynamic process involving several major steps. Firstly, osteoblasts are differentiated from the mesenchymal cells and then secret an extracellular organic matrix called osteoid; the osteoid is then mineralized and becomes bone; the newly-formed bone matures and ages and eventually is resorbed by osteoclasts.

The osteoid is composed of uncalcified collagen fibrils that are formed by the self-assembly of genetic type-I collagen molecules and probably some noncollagenous proteins. The chemical composition and mechanical features of the osteoid are similar to many other soft connective tissues such as tendon and ligaments. However, the osteoid can be mineralized under normal physiological conditions, converting it from a soft and pliable tissue into the hard and rigid bone tissue, thus support the body and protecting the internal organs.

It is not clear why collagen fibrils in the osteoid can be mineralized in vivo. Past research had been focused on the role of certain noncollagenous proteins, which were proposed to promote or inhibit the osteogenesis process (106, 107). However, whether these proteins participate the mineralization step directly or not remains unknown. More importantly, it was found that reconstituted collagen fibrils not containing those proteins can still be mineralized in vitro, suggesting that noncollagenous proteins may not be necessary factors for the mineralization to occur (66).

Note that the vast majority of the mineral content is NOT deposited in the inter-fibrillar spaces of the osteoid but within the individual collagen fibrils (18). It was proposed that the spatial arrangement of the collagen molecules in the fibrils might be essential for the nucleation of Ca-P apatite crystals (6). However, to our knowledge, there are no first-hand materials about the three-dimensional supramolecular architecture of the collagen fibrils in osteoid. Owing to the continuous remodeling, normal bone tissues from young or adult animals are usually mixtures of aged and newly formed tissues. The current micro-dissection techniques cannot separate the uncalcified collagen fibrils from those calcified and thus facilitate the X-ray diffraction study. TEM may not be the suitable tool to study the structure of the uncalcified fibrils, in particular, the lateral packing of collagen molecules, because it will be easily altered by the destructive sample preparation process. A relatively large amount of uncalcified collagen fibrils may be found in embryo bones, but the orientation of those fibrils is poor, which again hinders the X-ray structure analysis.

The present work chose intramuscular shad and herring bones to study the ultra-structural development of bone collagen fibrils before and after the initial mineralization. These bones contain very few oestoblasts so the mineralization process as well as the turnover is relatively slow. Consequently, collagen fibrils at different developing stages are no longer mixed together but well separated along the length of the fiber-shaped bone (Fig. 5.1). From the fleshy end at the bottom, the uncalcified collagen fibrils become progressively more mature when approaching the initial site of mineralization. The degree of mineralization gradually increases from the mineralization front to the spur in the middle (18). Additionally, the collagen fibrils are well-oriented to the bone axis. Thus,

the anatomical and analytical difficulties mentioned above are largely obviated. For the first time, we could conduct a detailed synchrotron X-ray scattering study on the ultra-structural development of the bone collagen matrix.

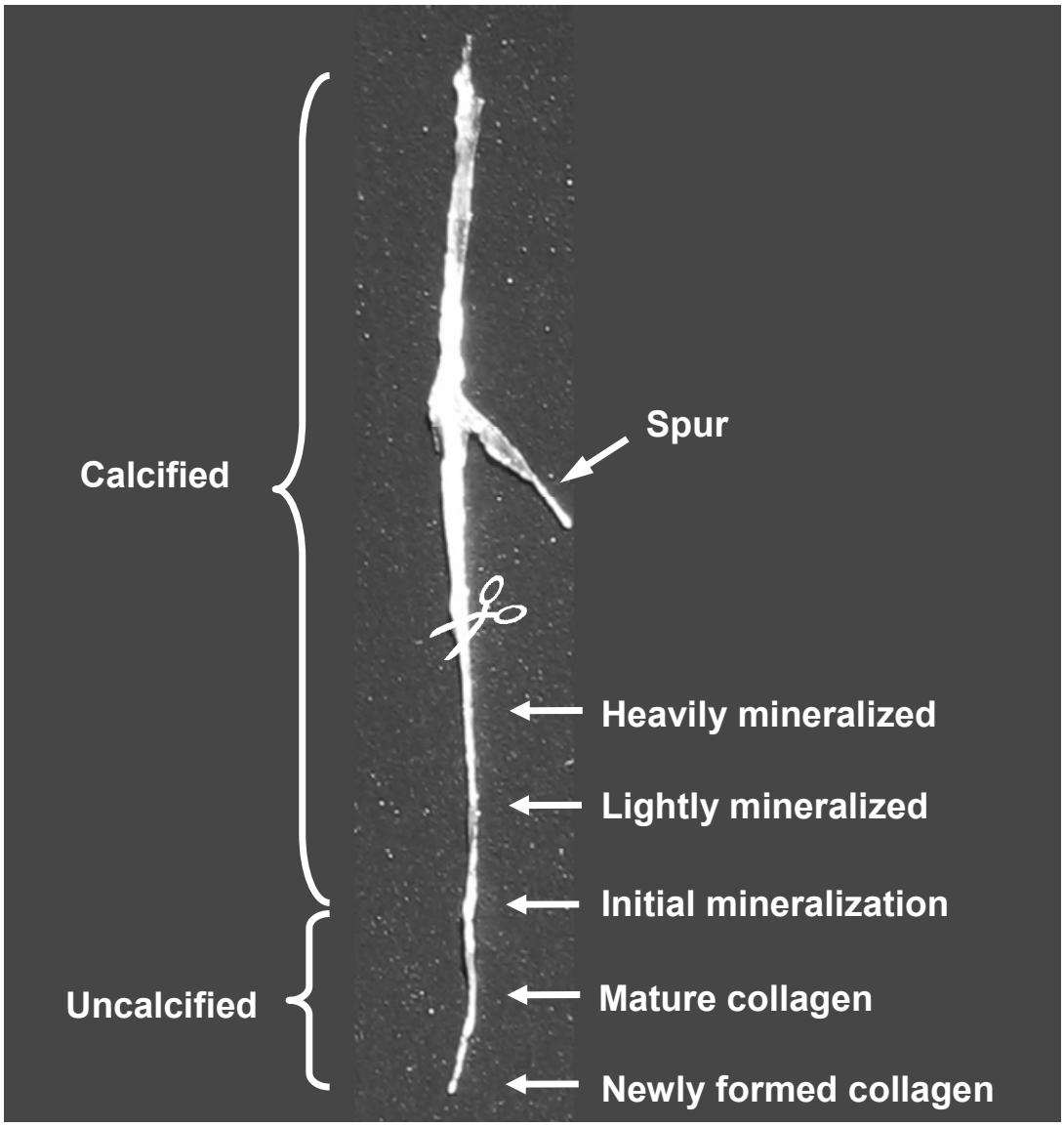

Figure 5.1 Photograph of a typical intramuscular herring bone. The sample consists of a long and rigid calcified portion and a short and soft uncalcified portion. X-ray diffraction studies were conducted on the lower half of the sample. 2D patterns were recorded for different spots along the length of the bone.

5.2 Experimental

Fresh bone samples were extracted from the muscles close to the tail fin of shad or herring of approx. 3 to 5 years old, then immediately frozen in the liquid nitrogen and stored with dry ice. Selected samples were treated with 0.5 M EDTA for 9 days to dissolve the mineral content in the calcified portion. The EDTA treated samples (including both uncalcified collagen and decalcified collagen) serve as the control for the native bone. Prior to the X-ray study, the portion below the spur was cut off (see Fig. 5.1) and sealed in the thin-walled quartz capillary tube from Charles Supper Co. The measured sample is typically 20 mm in length and 0.5 mm in diameter. During the measurement, the capillary tube was fixed on an X-Z translational stage so that the sample can be displaced horizontally and vertically. The step resolution of the translational stage is approximately 60 μm.

Information about the X-ray instrumentation, image processing, and data analysis is described in previous chapters. The sample-to-detector distance was adjusted to record the scattered X-ray from 0.08° to 45°, corresponding to the spatial resolution from 0.2 nm to 100 nm (see Table 5.1 for more details). 2D X-ray diffraction patterns were taken from spots along the length of the fish bone samples. The step size was about 1 mm in regions far away from the mineralization front but reduced to about 60 μm when approaching the initial site of mineralization. The structural information recorded on SAXS, MAXS, and WAXD patterns from the same sampling volume is complementary with each other and thus provides a comprehensive view of the bone hierarchical structures over several levels.

Table 5.1 Details of the experimental setup

	Sample-to-detector distance (mm)	Spatial resolution (nm)	2θ (°)	Measured structure formation
SAXS	~ 2000	2.5 ~ 100	0.08 ~ 3	Longitudinal packing of collagen molecules in the fibril; lateral arrangement of mineral crystals in the fibril
MAXS	~ 300	0.4 ~ 16	0.5 ~ 20	Lateral packing of collagen molecules in the fibril
WAXD	~ 100	0.2 ~ 5	1 ~ 45	Crystal structure of the mineral phase

SAXS — Small-angle X-ray scattering;
MAXS — Medium-angle X-ray scattering;
WAXD — Wide-angle X-ray diffraction.

5.3 Results and Discussion

Newly Formed Bone Collagen. The hierarchical structures in the newly-secreted organic matrix are highly disordered. Collagen fibrils have a relatively broad orientation distribution about the bone axis, as shown in the corresponding SAXS pattern (Fig. 5.2) that the angular spread of the meridional reflections is broad. The equidistant meridional reflections originate from the periodic arrangement of the collagen molecules in the fibril axis direction. A quantitative analysis to these reflections (see Chapter 3) leads to the integrated intensities of different orders, the axial period, the orientation distribution of the fibrils, the fibril diameter, and the longitudinal coherence length (Tables 5.2 and 5.3).

Collagen fibrils are formed by self-assembly of the collagen molecules through hydrophobic and charged interactions (108), which are maximized when adjacent

molecules are staggered by multiples of 234 residues or in the longitudinal direction. This staggered arrangement then creates the gap and overlap regions along the fibril axis, providing that the total length of the collagen molecule is not integer times of 234 residues (22). The intensities for orders 1-5 are the results from the ratio of the gap and overlap lengths. The relatively strong 6th, 12th, 15th, and 20th orders are probably related to the subperiod for the arrangement of the hydrophobic and charged side groups (108-110). The absence of other high order reflections suggests that the fine features of the molecular assembly consist of substantial disorders. For instance, the peptide repeat in the α chains formed a very weak long-range order thus the layer line at 0.286 nm is hardly discernable on the corresponding WAXD pattern (data not shown). Additionally, no lateral packing order was observed for the molecular arrangement in the newly formed bone collagen fibrils.

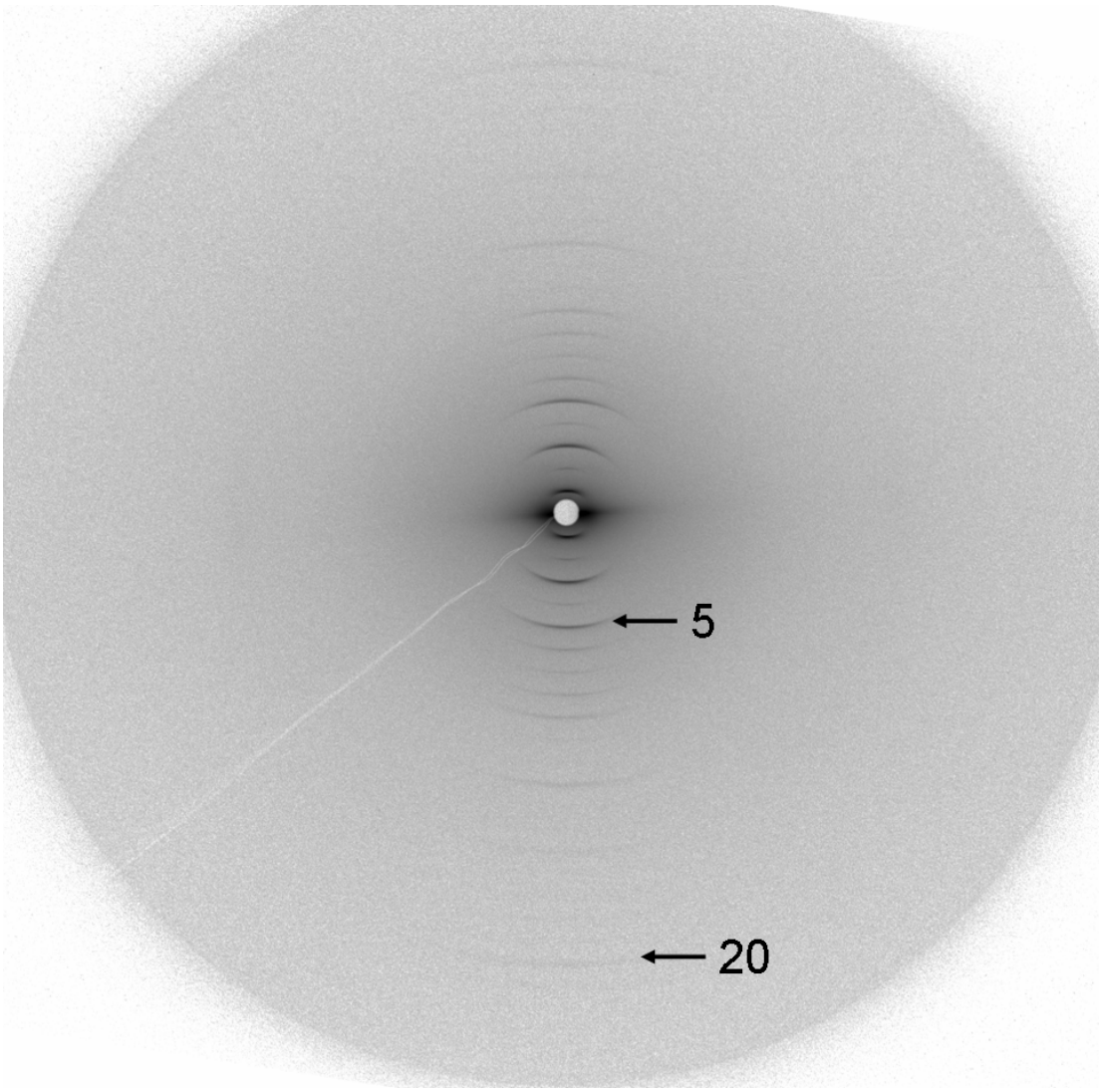

Figure 5.2 SAXS pattern from the portion composed of newly formed bone collagen fibrils. The long axis of the bone was parallel to the vertical direction, so the meridian is vertical and the equator is horizontal. The 5th and 20th meridional orders are indicated. The axial period of the equidistant meridional reflections is 66.7 nm.

Table 5.2 Relative intensities of the meridional reflections for herring bone collagen at different developmental stages[1]

Order	Newly formed collagen	Mature collagen	Lightly mineralized	Heavily mineralized
1	1000(8)	1000(5)	1000(9)	1000(7)
2	34(1)	3(0)	32(1)	52(1)
3	562(7)	454(3)	386(5)	405(3)
4	30(1)	16(1)	16(1)	16(1)
5	339(5)	267(2)	162(2)	138(2)
6	75(2)	49(1)	64(2)	83(2)
7	38(2)	55(1)	63(2)	20(2)
8	62(2)	74(1)	37(2)	-
9	80(2)	96(1)	148(3)	38(3)
10	-	33(1)	61(3)	-
11	-	9(1)	72(4)	32(3)
12	95(5)	105(2)	69(4)	-
13	-	12(1)	26(3)	-
14	-	17(1)	67(4)	-
15	52(7)	52(2)	21(3)	-
16	-	7(1)	22(4)	-
17	-	28(1)	31(4)	-
18	-	43(2)	-	-
19	-	31(1)	52(5)	-
20	117(9)	146(3)	103(7)	-
21	-	45(2)	40(4)	-
22	-	17(1)	-	-
23	-	-	-	-
24	-	15(1)	-	-
25	-	45(3)	-	-

[1] Scaling is such that the 1st orders are equal to 1000.

Table 5.3 Structure parameters of collagen fibrils at different developmental stages

	Newly formed collagen	Mature collagen	Lightly mineralized	Heavily mineralized
Coherence length (μm)	1.00(6)	1.01(1)	0.86(2)	0.94(3)
Hermans' orientation factor[1]	0.907(2)	0.979(1)	0.975(1)	0.961(1)
Axial period (nm)	66.7(1)	66.6(1)	66.4(1)	66.4(1)
Fibril "diameter"[2] (nm)	102(1)	85(2)	59(2)	54(2)

[1] Hermans' orientation factor was defined in Chapter 3. It has values between 0 and 1. Zero means randomly oriented and one means perfectly oriented. Larger values mean better orientation.

[2] For mineralized bone, this parameter represents the lateral dimension of the domain defined by the mineral phase rather than the fibril.

Collagen Maturation in Osteoid. The hierarchical structures of the osteoid become progressively more ordered when it approaches to the mineralization front. The collagen fibrils show improved orientation (column three in Table 5.3) with respect to the primary bone axis. Strong meridional reflections up to the 25th order are readily seen in the SAXS patterns (see Fig. 3.4 for example) and the layer line corresponding to the peptide repeat becomes more visible in the WAXD patterns (Fig. 5.5), suggesting that the α chain conformation in the triple helical region and the longitudinal arrangement of the molecules are more ordered. More importantly, the packing of the molecules in the lateral direction shows long-range order, as indicated by the equatorial Bragg reflections in Fig. 5.3. The lateral packing of collagen molecules in bone collagen fibrils prior to mineralization has been described in Chapter 2. The molecules are first grouped into the Smith type micro-fibrils and the microfibrils are then packed on a 2D oblique lattice with some degree of translational and rotational disorders (see Fig. 2.3). The ordered packing of microfibrils creates parallel "channels" in bone collagen fibrils, which are the ideal spaces to accommodate the platelet-shaped apatite crystals.

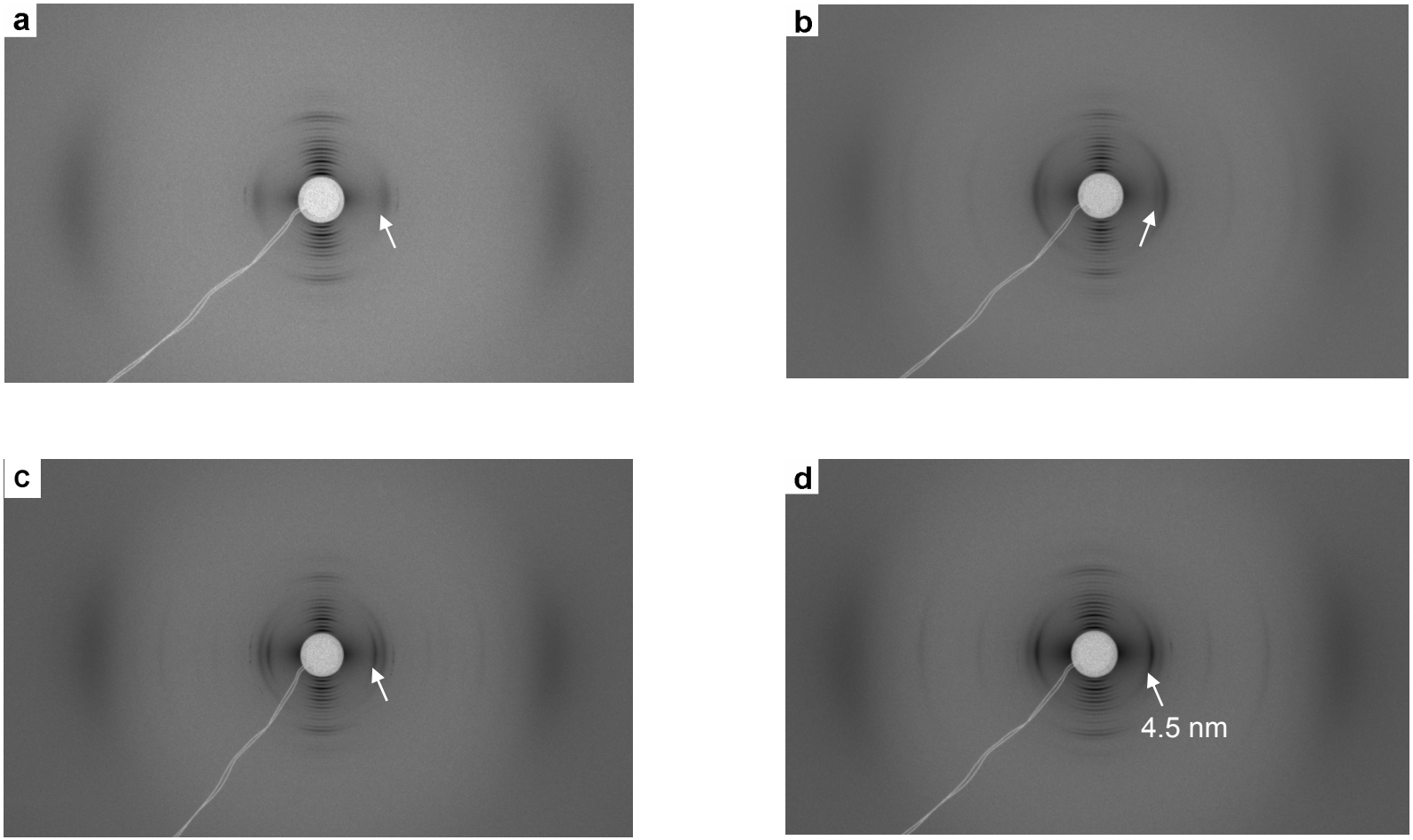

Figure 5.3 MAXS patterns from the portion consisting of more mature bone collagen. From (a) to (d), the sampling position moves closer toward the mineralization front. (d) was taken from the spot just before the first detectable mineral. All white arrows indicate the equatorial reflection with a Bragg spacing of 4.5 nm. Other peak positions are listed in Tab. 2.1.

The lateral packing of micro-fibrils contains more disorders for the less mature osteoid, hence the row-lines at 3.9 nm and 4.5 nm are weak and broad and are superimposed together (Fig. 5.3a). For the osteoid closer to the mineralization front, the packing of the microfibrils becomes more ordered, thus the individual row-lines are well separated and their relative intensities are stronger (Fig. 5.3b, c). Near the initial site of mineralization, the intensity of the row-line at 4.5 nm increases dramatically, suggesting that the alignment of the microfibrils along the "channels" is greatly improved. Consequently, the "channels" are more straight and spacious, making it less resistant for crystal growth in the width dimension.

The ultrastructural evolution of the bone collagen fibrils might be related to the formation of the cross-links between neighboring molecules and/or microfibrils. These individual structure units are flexible because of their large aspect ratios, so the packing of the molecules or microfibrils into the fibril is likely to contain many local disorders. The formation of the cross-links between the telopeptides of one molecule and the helical region of another molecule (8, 111-116) will largely restrict the molecular mobility and improve the overall rigidity of the organic matrix, which may also reduce the density of the disorders. However, to understand the effect of the cross-links on molecular packing in bone collagen fibrils, it is necessary to study the biochemical changes of the collagen matrix before the deposition of the mineral phase, which, to our knowledge, has not been conducted so far.

Initial Site of Mineralization. The long-range order of the molecular packing in the cross-section of the fibrils is immediately destroyed once mineralization starts. The

nucleation and initial growth of the apatite crystals may be confined within the "channels" to minimize the energy required for distorting the surrounding organic matrix. The packing of the mineral crystals in bone collagen fibrils will be described in detail in next section. The impact of mineralization on the supramolecular architecture of bone collagen fibrils is not reversible. We observed that the lateral packing order of the collagen molecules in fibrils was well-preserved in the EDTA-treated uncalcified bone (Fig. 5.4a). However, only very weak lateral packing order was shown on the XRD patterns from the demineralized bone samples (Fig. 5.4b).

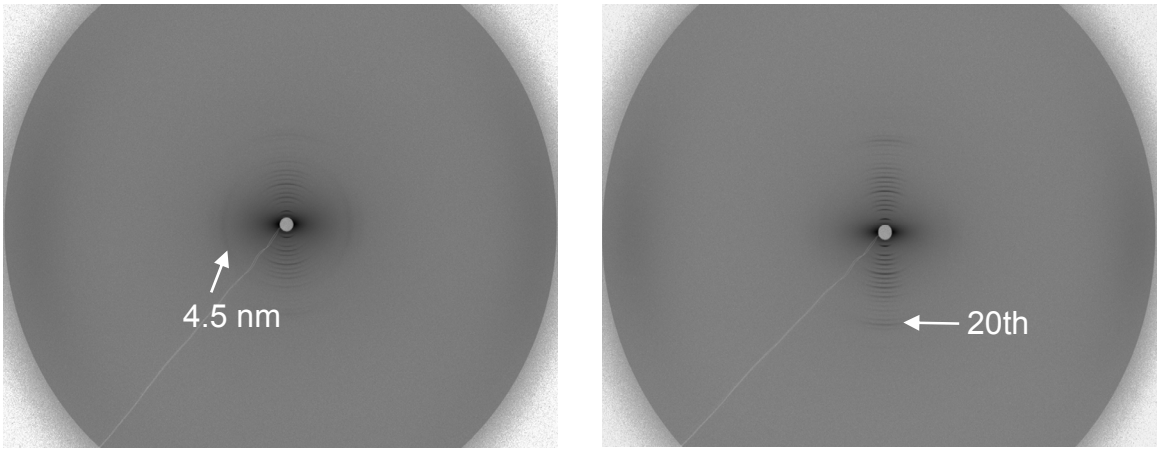

(a) (b)

Figure 5.4 XRD patterns from EDTA-treated bone samples. (a) was taken from spot in the uncalcified portion and (b) was from demineralized portion. The sample-to-detector distance was about 750 mm. The arrow in the left pattern indicates the equatorial reflection with Bragg spacing of 4.5 nm. The arrow in the right pattern indicates the 20th order meridional reflections. The axial period of the equidistant meridional reflections is 64.7 nm.

The crystalline structure of the mineral phase was studied by WAXD. The first detectable mineral was found to have a very poor crystalline structure. Only one weak

peak corresponding to the (002) reflection of hydroxyapatite was observed (see Pattern m_0 in Fig. 5.5). The intensity of the (002) reflection increases as the mineralization progresses, and other Bragg reflections from the hydroxyapatite structure are observed (Fig. 5.5), suggesting that more mineral content has been deposited into the organic matrix and the crystalline structure of the mineral phase becomes increasingly ordered. However, the crystal structure of the bone apatite is still much less ordered than the synthetic hydroxyapatite crystals—the latter shows many more Bragg reflections in the corresponding diffraction patterns.

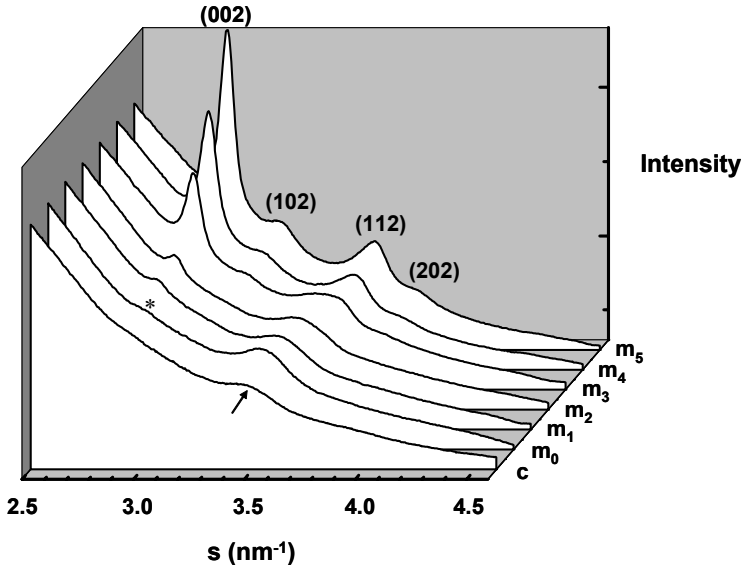

Figure 5.5 Evolution of the crystalline structure of the mineral phase in intramuscular herring bone. Pattern *c* is from the spot just before the first detectable mineral. The peak indicated by the arrow (~ 3.49 nm^{-1}) comes from the peptide repeat in α chains. The first detectable mineral is observed on m_0, where the (002) reflection of hydroxyapatite is marked by a star (*). The peak from collagen is still there and no other hydroxyapatite reflections are observed. Patterns m_1 and m_2 are from two consecutive spots after m_0. The (002) reflection becomes stronger but still no other reflections from the mineral phase are detectable. Pattern m_3 is from a spot in the lightly mineralized portion. The (102) hydroxyapatite reflection becomes visible. The broad peak at about 3.5 nm^{-1} is the superposition of the (112) hydroxyapatite reflection and the one from collagen. Patterns m_4 and m_5 are from spots in the heavily mineralized portion of the herring bone sample and contain more mature crystals.

Maturation of the crystal structure of bone mineral is accompanied by the change of the chemical compositions. Bone mineral has a crystal structure similar to hydroxyapatite, $Ca_{10}(PO_4)_6(OH)_2$, but differs in the exact composition and crystal imperfections. A portion of the phosphate groups (PO_4) in bone mineral are substituted by the carbonate groups (CO_3) and acid phosphate groups (HPO_4) either in the interior of the crystal or on its surface (117-120), and a small amount of the calcium ions may also be substituted by magnesium and sodium (for a recent review, see (1)). The hydroxyl groups (OH) are deficient compared with the stoichiometric hydroxyapatite crystals (121-126), and the $Ca/(P+CO_3)$ molar ratio is smaller than the ideal value of hydroxyapatite (~ 1.67), leaving numerous cation vacancies in the crystal lattice (124). "Young" crystals have lower $Ca/(P+CO_3)$ molar ratios so they contain more imperfections than the "aged" crystals. It was also found that the content of the acid phosphate groups decreases and the content of the carbonate groups increases after the initial deposition (124). But its implication on the crystalline structure is not clear.

Development of Collagen/Mineral Superstructure. Unlike the bones in higher vertebrates, in which regions of the newly-formed osseous tissue are mixed with regions of the aged tissue in a microscopic scale (i.e., much smaller than the typical size of an X-ray beam), the intramuscular shad/herring bone shows a gradually increased degree of mineralization along the bone axis (18), thus allowing us to use X-ray scattering and diffraction techniques to study the structural evolution of bone at different developing stages. SAXS patterns from spots at different degrees of mineralization were analyzed, and the results are listed in Tab. 5.4. The average thickness of the mineral crystals $\langle T \rangle$

shows a monotonic increase from ca. 1.8 nm at the initial site of mineralization to ca. 2.1 nm at the heavily mineralized regions. However, the thickness distribution of the mineral crystals σ_T at each developing stage is relatively narrow (see Fig. 5.6, left), indicating that bone apatite crystals of a similar age have a nearly uniform thickness. The average separation between the neighboring crystals $\langle t \rangle$ decreases from ca. 7 nm at the initial site of mineralization to ca. 5 nm at the heavily mineralized regions, suggesting that the packing of mineral crystals in the collagen matrix becomes more dense as the mineralization progresses. However, the separations between adjacent crystals within a mineral stack are broadly distributed (see Fig. 5.6, right). The average crystal height H, i.e., the dimension along the c-axis direction, also shows an increase from the initial site of mineralization (~ 30 nm) to the heavily mineralized regions (~ 50 nm). The overall orientation of the mineral stacks defined by the Hermans' orientation factor (80, 101) remains unchanged.

Table 5.4 Structure parameters about the lateral packing of mineral crystals at different degree of mineralization[1,2,3]

	Hermans' orientation factor	$\langle T \rangle$ (nm)	σ_T (nm)	$\langle t \rangle$ (nm)	σ_t (nm)	H (nm)
IM01	0.882(1)	1.81(1)	0.08(1)	7.28(4)	4.31(3)	30.6(3)
LM02	0.885(1)	2.00(1)	0.07(1)	6.13(3)	3.75(2)	36.1(3)
LM03	0.881(1)	1.95(1)	0.07(1)	5.66(3)	3.37(2)	39.8(4)
LM04	0.880(1)	1.96(1)	0.06(2)	5.26(3)	3.03(2)	46.1(4)
HM05	0.884(1)	2.03(1)	0.06(2)	5.28(2)	3.00(2)	48.8(5)
HM06	0.883(1)	2.05(1)	0.05(3)	5.47(2)	3.09(2)	51.2(5)

[1] Parameters extracted by fitting the near-equatorial diffuse scattering.
[2] IM − the initial site of mineralization; LM − lightly mineralized portion; HM − heavily mineralized portion.
[c] $\langle T \rangle$ – average thickness of the mineral crystals; σ_T – width of the thickness distribution of the mineral crystals; $\langle t \rangle$ – average thickness of the intercalated organic layers between neighboring crystals; σ_t – width of the thickness distribution of the organic layers; H – average crystal length in the *c*-axis dimension.

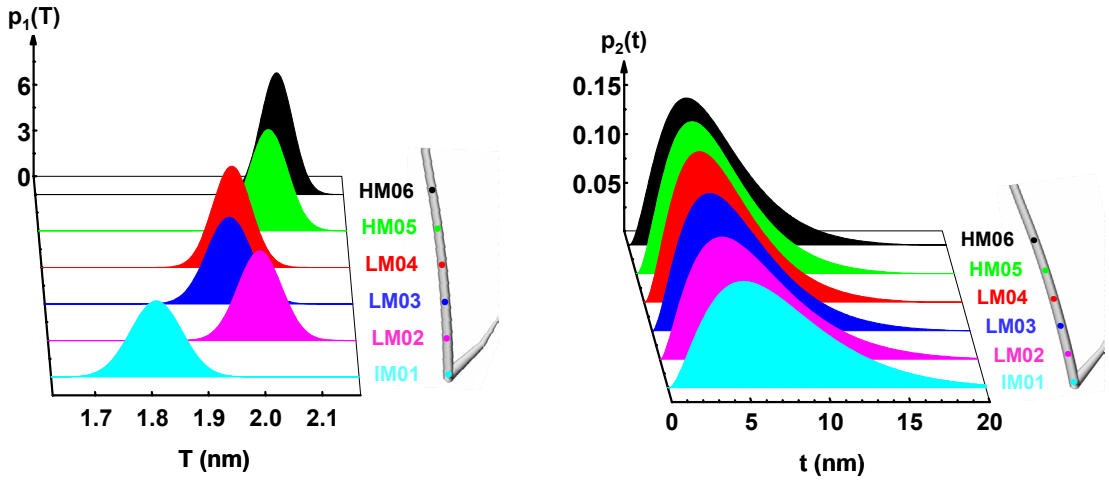

Figure 5.6 Evolution of the mineral crystal packing in the collagen matrix at different degrees of mineralization. The thickness distributions of the mineral crystals are plotted as the narrow Gaussian and the thickness distributions of the intercalated organic layers are plotted as the Gamma distribution (see Chapter 3 for details). Note that the scale range for the mineral thickness distribution (left) is 1/40 of that for the organic layer thickness distribution (right).

Note that the majority of the bone mineral crystals are formed within a confined environment, i.e., the individual collagen fibrils based on which the bone tissues are constructed. The nucleation and crystal growth thus are strongly affected by the 3D supramolecular architecture in the collagen fibrils (6). We have shown in the previous sections that, prior to mineralization, parallel "channels" are created within the collagen fibrils by the ordered packing of molecules in the fibril cross-section. The "channels" are ca. 1.5 nm in breadth, which is comparable to the thickness of the early mineral crystals. Crystal growth in the thickness dimension is strongly constrained by the breadth of the "channel", as indicated by the small increase of the crystal thickness from the lightly mineralized regions to the heavily mineralized regions. On the other hand, the length of

the “channels” extends to more than 50 nm, thus the crystal growth in this dimension (corresponding to the width of the crystal) can reach tens of nanometers.

The parallel arrangement of the “channels” in unmineralized bone collagen fibrils ensures that the mineral crystals form lamellar stacks rather than being randomly oriented in the cross-section of the fibril. For the platelet-shaped crystals, the formation of stacks can achieve higher packing density and therefore improved mechanical strength and stiffness. At the early stages of mineralization, the apatite crystals may be randomly deposited into the parallel “channels” thus the separation between the nearest neighbors, or the thickness of the intercalated organic layers is expected to have a relatively broad distribution, as depicted in Fig. 5.6. However, it should be mentioned that the nucleation and growth of a mineral crystal in one “channel” perturbs the surrounding matrix structure as well as the adjacent “channels”. Consequently, the packing of mineral platelets does not possess long-range order in the lateral direction. Molecular packing in the axial direction was also disturbed and the high order meridional reflections were attenuated.

5.4 Conclusion

The ultrastructural evolution of bone collagen was studied by synchrotron X-ray scattering techniques and the subsequent quantitative analysis. The results showed that the hierarchical structures are less-ordered in the newly-formed osteoid but become more organized when the osteoid is more mature. Molecular packing in mature collagen fibrils shows long-range order in the lateral direction and results in broad parallel “channels”. The “channels” are mostly aligned in the osteoid just before the mineralization front,

suggesting the organic matrix is ready for the deposition of mineral crystals. The first detectable mineral has a crystalline structure similar to that of hydroxyapatite, but with considerably more crystal imperfections. The density of the imperfections is reduced for more mature crystals. The packing of the mineral crystals forms irregular lamellar stacks in the collagen matrix. The crystal growth mainly occurs in the length and width direction, the thickness of the mineral crystals remains nearly unchanged during the mineralization process. Meanwhile, the packing density of the apatite crystals increases with more mineral content deposited into the fibrils. The average separation between adjacent crystals is about 7 nm at the initial site of mineralization and reduced to about 5 nm for heavily mineralized fibrils.

Chapter 6. Conclusions

Based on the interpretation of the strong equatorial Bragg reflections observed for the first time for any bone tissues, a new molecular packing scheme was discovered for bone collagen,. The arrangement of collagen molecules in bone collagen fibrils is significantly different from early postulations modified from the rat tail tendon collagen structure and particularly suited for the mineralization of bone.

A 2D scheme was developed for analyzing SAXS patterns showing preferred orientation and was applied to the equidistant meridional reflections resulting from periodic structure of collagen fibrils in the axial direction and the fan-shaped near-equatorial diffuse scattering resulting from the lateral arrangement of mineral crystals in the collagen matrix. The analysis leads to a comprehensive 3D ultrastructural construct over several levels of bone hierarchy, which is critical for a correct understanding of the biological and physiological functions and mechanical properties of bone.

The 3D ultrastructural evolution of the bone tissue was investigated by combined SAXS/MAXS/WAXD study of bone collagen at different developing stages. The results showed how the osteoid matures before mineralization, the abrupt change of bone collagen structure at the initial site of mineralization, the crystalline structure of the first detectable mineral phase; and the 3D collagen/mineral ultrastructural development during bone mineralization and aging.

Bibliography

1. Glimcher, M. J. 1998. The nature of the mineral phase in bone: Biological and clinical implications. In *Metabolic Bone Disease and Clinically Related Disorders*. L. V. Avioli, and S. M. Krane, editors. Academic Press, San Diego. 23-50.

2. Weiner, S., and H. D. Wagner. 1998. The material bone: Structure-mechanical function relations. *Annu. Rev. Material Sci.* **28**:271-298.

3. Glimcher, M. J. 2006. Bone: Nature of the calcium phosphate crystals and cellular, structural, and physical chemical mechanisms in their formation. *Reviews in Mineralogy and Geochemistry* **64**:223-282.

4. Weiner, S., and W. Traub. 1992. Bone structure: from angstroms to microns. *FASEB J.* **6**:879-885.

5. Rich, A., and F. H. C. Crick. 1963. The molecular structure of collagen. *J. Mol. Biol.* **3**:483-506.

6. Glimcher, M. J. 1959. Molecular biology of mineralized tissues with particular reference to bone. *Rev. Modern Phys.* **31**:359-393.

7. Glimcher, M. J. 1960. Specificity of the molecular structure of organic matrices in mineralization. In *Calcification in biological systems*. R. F. Sogannes, editor. Am. Assoc. Adv. Sci., Washington DC. 421-487.

8. Bailey, A. J., N. D. Light, and E. D. T. Atkins. 1980. Chemical cross-linking restrictions on models for the molecular organization of collagen fiber. *Nature* **288**:408-410.

9. Bocciarelli, D. S. 1970. Morphology of crystallites in bone. *Calcif. Tissue Res.* **5**:261-269.

10. Kim, H.-M., C. Rey, and M. J. Glimcher. 1995. Isolation of calcium-phosphate crystals of bone by nonaqueous methods at low temperature. *J. Bone Miner. Res.* **10**:1589-1601.

11. Eppell, S. J., W. Tong, J. L. Katz, L. Kuhn, and M. J. Glimcher. 2001. Shape and size of isolated bone mineralites measured using atomic force microscopy. *J. Orthop. Res.* **19**:1027-1034.

12. Tong, W., M. J. Glimcher, J. L. Katz, L. Kuhn, and S. J. Eppell. 2003. Size and shape of mineralites in young bovine bone measured by atomic force microscopy. *Calcif. Tissue Int.* **72**:592-598.

13. Gao, H., B. Ji, I. L. Jäger, E. Arzt, and P. Fratzl. 2003. Materials become insensitive to flaws at nanoscale:Lessons from nature. *Proc. Natl. Acad. Sci. USA* **100**:5597-5600.

14. Ji, B., and H. Gao. 2004. Mechanical properties of nanostructure of biological materials. *J. Mech. Phys. Solids* **52**:1963-1990.

15. Ji, B., and H. Gao. 2004. A study of fracture mechanisms in biological nano-composites via the virtual internal bond model. *Mater. Sci. Eng. A* **366**:96-103.

16. Glimcher, M. J. 1968. A basic architectural principle in organization of mineralized tissues. *Clin. Orthop. Rel. Res.* **61**:16-36.

17. Glimcher, M. J. 1984. Recent studies of the mineral phase in bone and its possible linkage to the organic matrix by protein-bound phosphate bonds. *Phil. Trans. R. Soc. Lond. B* **304**:479-508.

18. Lee, D. D., and M. J. Glimcher. 1991. Three-dimensional spatial relationship between the collagen fibrils and the inorganic calcium phosphate crystals of pickerel (americanus americanus) and herring (clupea harengus) bone. *J. Mol. Biol.* **217**:487-501.

19. Bear, R. S. 1942. X-ray diffraction studies on protein fibers. I. The large fiber-axis period of collagen. *J. Am. Chem. Soc.* **66**:1297-1305.

20. Bear, R. S. 1952. The structure of collagen fibrils. *Advances in protein chemistry* **7**:69-160.

21. Schmitt, F. O., C. E. Hall, and M. A. Jakus. 1942. Electron microscope investigations of the structure of collagen. *J. Cell. Comp. Physiol.* **20**:11-33.

22. Hodge, A. J., and J. A. Petruska. 1963. Recent studies with the electron microscope on ordered aggregates of the tropocollagen molecule. In *Aspects of Protein Structure*. G. N. Ramachandran, editor. Academic Press, New York 289-300.

23. Fitton-Jackson, S. 1957. The fine structure of developing bone in the embryonic fowl. *Proc. Roy. Soc. (London) B* **14**:270-280.

24. Finean, J. B., and A. Engstrom. 1953. The low-angle scatter of x-rays from bone tissue. *Biochim. Biophys. Acta* **11**:178-189.

25. Carlstrom, D., and J. B. Finean. 1954. X-ray diffractgion studies on the ultrastructure of bone. *Biochim. Biophys. Acta* **13**:183-191.

26. Chen, J.-L., C. Burger, C. V. Krishnan, B. Chu, B. S. Hsiao, and M. J. Glimcher. 2005. In vitro mineralization of collagen in demineralized fish bone. *Macromol. Chem. Phys.* **206**:43-51.

27. Tomlin, S. G., and C. R. Worthington. 1956. Low-angle x-ray diffraction patterns of collagen. *Proc. Roy. Soc. A.* **235**:189-201.

28. Ericson, L. G., and S. G. Tomlin. 1959. Further studies of low-angle x-ray diffraction patterns of collagen. *Proc. Roy. Soc. (London) A* **252**:197-216.

29. Hulmes, D. J. S., Miller, A., White, S.W. & Doyle, B.B. 1977. Interpretation of the low angle meridional x-ray diffraction pattern from collagen fibers in terms of known amino acid sequence. *J. Mol. Biol.* **110**:643-666.

30. Chandross, R. J., and R. S. Bear. 1973. Improved profiles of electron-density distribution along collagen fibrils. *Biophys. J.* **13**:1030-1048.

31. Chapman, J. A. 1974. Staining pattern of collagen fibrils. 1. Analysis of electron micrographs. *Connect. Tissue Res.* **2**:137-150.

32. Hulmes, D. J. S., and A. Miller. 1979. Quasi-hexagonal molecular packing in collagen fibrils. *Nature* **282**:878-880.

33. Fraser, R. D. B., T. P. MacRae, A. Miller, and E. Suzuki. 1983. Molecular conformation and packing in collagen fibrils. *J. Mol. Biol.* **167**:497-521.

34. Hulmes, D. J. S., T. J. Wess, D. J. Prockop, and P. Fratzl. 1995. Radial packing, order, and disorder in collagen fibrils. *Biophys. J.* **68**:1661-1670.

35. Wess, T. J., A. P. Hammersley, L. Wess, and A. Miller. 1998. Molecular packing of type I collagen in tendon. *J. Mol. Biol.* **275**:255-267.

36. Orgel, J. P. R. O., A. Miller, T. C. Irving, R. F. Fischetti, A. P. Hammersley, and T. J. Wess. 2001. The in situ supermolecular structure of type I collagen. *Structure* **9**:1061-1069.

37. Orgel, J. P. R. O., T. Irving, A. Miller, and T. J. Wess. 2006. Mircofibrillar structure of type I collagen in situ. *Proc. Natl. Acad. Sci. USA* **103**:9001-9005.

38. North, A. C. T., P. M. Cowan, and J. T. Randall. 1954. Structural units in collagen fibrils. *Nature* **174**:1142 - 1143.

39. Miller, A., and J. S. Wray. 1971. Molecular packing in collagen. *Nature* **230**:437.

40. Jésior, J. C., A. Miller, and C. Berthet-Colominas. 1980. Crystalline 3-dimensional packing is a general characteristic of type-I collagen fibrils. *FEBS Lett.* **113**:238-240.

41. Brodsky, B., and E. F. Eikenberry. 1982. Characterization of fibrous forms of collagen. *Methods in Enzymology* **82**:128-174.

42. Brodsky, B., E. F. Eikenberry, K. C. Belbruno, and K. Sterling. 1982. Variations In collagen fibril structure in tendons. *Biopolymers* **21**:935-951.

43. Katz, E. P., and S. T. Li. 1972. The molecular packing of collagen in mineralized and non-mineralized tissues. *Biochem. Biophys. Res. Comm.* **46**:1368-1373.

44. Katz, E. P., and S. T. Li. 1973. The intermolecular space of reconstituted collagen fibrils. *J. Mol. Biol.* **73**:351-369.

45. Katz, E. P., and S. T. Li. 1973. Structure and function of bone collagen fibrils. *J. Mol. Biol.* **80**:1-15.

46. Hodge, A. J. 1989. Molecular models illustrating the possible distributions of holes in simple systematically staggered arrays of type I collagen molecules in native-type fibrils. *Connect. Tissue Res.* **21**:467-477.

47. Landis, W. J., M. J. Song, A. Leith, L. McEwen, and B. F. McEwen. 1993. Mineral and organic matrix interaction in normally calcifying tendon visualized in three dimensions by high-voltage electron-microscopic tomography and graphic image-reconstruction. *J. Struct. Biol.* **110**:39-54.

48. Smith, J. W. 1968. Molecular pattern in native collagen. *Nature* **219**:157-158.

49. Bouteill, M., and D. C. Pease. 1971. Tridimensional structure of native collagenous fibrils, their proteinaceous filaments. *J. Ultrastruct. Res.* **35**:314-338.

50. Lillie, J. H., D. K. Maccallum, L. J. Scaletta, and J. C. Occhino. 1977. Collagen structure: Evidence for a helical organization of collagen fibril. *J. Ultrastruct. Res.* **58**:134-143.

51. Ruggeri, A., F. Benazzo, and E. Reale. 1979. Collagen fibrils with straight and helicoidal microfibrils - freeze-fracture and thin-section study. *J. Ultrastruct. Res.* **68**:101-108.

52. Raspanti, M., V. Ottani, and A. Ruggeri. 1989. Different architectures of the collagen fibril - morphological aspects and functional implications. *Int. J. Biol. Macromol.* **11**:367-371.

53. Holmes, D. F., C. J. Gilpin, C. Baldock, U. Ziese, A. J. Koster, and K. E. Kadler. 2001. Corneal collagen fibril structure in three dimensions: Structural insights into fibril assembly, mechanical properties, and tissue organization. *Proc. Natl. Acad. Sci. USA* **98**:7307-7312.

54. Parry, D. A. D., and A. S. Craig. 1979. Electron-microscope evidence for an 80 Å unit in collagen fibrils. *Nature* **282**:213-215

55. Trus, B. L., and K. A. Piez. 1980. Compressed microfibril models of the native collagen fibril. *Nature* **286**:300-301.

56. Piez, K. A., and B. L. Trus. 1981. A new model for packing of type-I collagen molecules in the native fibril. *Bioscience Rep.* **1** 801-810.

57. Ottani, V., M. Raspanti, and A. Ruggeri. 2001. Collagen structure and functional implications. *Micron* **32**:251-260.

58. Ottani, V., D. Martini, M. Franchi, A. Ruggeri, and M. Raspanti. 2002. Hierarchical structures in fibrillar collagens. *Micron* **33**:587-596.

59. Woodhead-Galloway, J., and P. A. Machin. 1976. Modern theories of liquids and diffuse equatorial x-ray-scattering from collagen. *Acta Cryst. A* **32**:368-372.

60. Hukins, D. W. L. 1977. X-ray-diffraction by collagen tape shows that type-1 collagen fibrils need not have a 3-dimensional lattice. *Biochem. Biophys. Res. Comm.* **77**:335-339.

61. Fratzl, P. 1994. Statistical model of the habit and arrangement of mineral crystals in the collagen of bone. *J. Stat. Phys.* **77**:125-143.

62. Kessler, E., K. Takahara, L. Biniaminov, M. Brusel, and D. S. Greenspan. 1996. Bone morphogenetic protein-1: The type I procollagen C-proteinase. *Science* **271**:360-362.

63. Weber, G. F., S. Ashkar, M. J. Glimcher, and H. Cantor. 1996. Receptor-ligand interaction between CD44 and osteopontin (Eta-1). *Science* **271**:509-512.

64. Lanske, B., A. C. Karaplis, K. Lee, A. Luz, A. Vortkamp, A. Pirro, M. Karperien, L. H. K. Defize, C. Ho, R. C. Mulligan, A. B. AbouSamra, H. Juppner, G. V. Segre, and H. M. Kronenberg. 1996. PTH/PTHrP receptor in early development and Indian hedgehog-regulated bone growth. *Science* **273**:663-666.

65. Jones, D. C., M. N. Wein, M. Oukka, J. G. Hofstaetter, M. J. Glimcher, and L. H. Glimcher. 2006. Regulation of adult bone mass by the zinc finger adapter protein Schnurri-3. *Science* **312**:1223-1227.

66. Glimcher, M. J. 1989. Mechanism of calcification: role of collagen fibrils and collagen-phosphoprotein complexes in vitro and in vivo. *Anatom. Res.* **224**:139-153.

67. Grynpas, M. 1977. Three-dimensional packing of collagen in bone. *Nature* **165**:381-382.

68. Burger, C., H.-W. Zhou, H. Wang, S. Igors, B. S. Hsiao, B. Chu, L. Graham, and M. J. Glimcher. 2008. Lateral packing of mineral crystals in bone collagen fibrils. *Biophys. J.* **95**:1-8.

69. Chu, B., and B. S. Hsiao. 2001. Small-angle X-ray scattering of polymers. *Chem. Rev.* **101**:1727-1761.

70. King, G., E. M. Brown, and J. M. Chen. 1996. Computer model of a bovine type I collagen microfibril. *Protein Eng.* **9**:43-49.

71. Fratzl, P., N. Fratzl-Zelman, and K. Klaushofer. 1993. Collagen packing and mineralization. *Biophys. J.* **64**:260-266.

72. Hulmes, D. J. S., A. Miller, S. W. White, P. A. Timmins, and C. Berthet-Colominas. 1980. Interpretation of the low-angle meridional neutron-diffraction patterns from collagen-fibers in terms of the amino-acid-sequence. *Int. J. Biol. Macromol.* **2**:338-346.

73. White, S. W., D. J. S. Hulmes, A. Miller, and P. A. Timmins. 1977. Collagen-mineral axial relationship in calcified turkey leg tendon by x-ray and neutron diffraction. *Nature* **266**:421-425.

74. Berthet-Colominas, C., A. Miller, and S. W. White. 1979. Structural study of the calcifing collagen in turkey leg tendons. *J. Mol. Biol.* **134**:431-445.

75. Ruland, W., and H. Tompa. 1968. The effect of preferred orientation on the intensity distribution of (hk) interferences. *Acta. Cryst. A* **24**:93-99.

76. Ruland, W. 1977. Elimination of the effect of orientation distribution in fiber diagrams. *Colloid Polym. Sci.* **255**:833-836.

77. Fraser, R. D. B., T. P. MacRae, A. Miller, and R. J. Rowlands. 1976. Digital processing of fibre diffraction patterns. *J. Appl. Cryst.* **9**:81-94.

78. Guinier, A. 1963. *X-ray diffraction: In crystals, imperfect crystals, and amorphous bodies.* Chap. 6 W.H. Freeman, San Francisco.

79. Onsager, L. 1949. The effects of shape on the interaction of colloidal particles. *Ann. N.Y. Acad. Sci.* **51**:627-659.

80. Hermans, J. J., P. H. Hermans, D. Vermaas, and A. Weidinger. 1946. Quantitative evaluation of orientation in cellulose fibres from the x-ray fibre diagram. *Recl. Trav. Chim. Pays-Bas-J. Roy. Neth. Chem. Soc.* **65**:427-447.

81. Zhou, H.-W., C. Burger, S. Igors, B. S. Hsiao, B. Chu, L. Graham, and M. J. Glimcher. 2007. Small-angle X-ray study of the three-dimensional collagen/mineral superstructure in intramuscular fish bone. *J. Appl. Cryst.* **40**:s666-s668.

82. Wang, S. K., and C. R. Worthington. 1975. Low-angle x-ray data processing for collagen. *Biophys. J.* **15**:322a.

83. Stinson, R. H., M. W. Bartlett, T. Kurg, P. R. Sweeny, and R. W. Hendricks. 1979. Experimental confirmation of calculated phases and electron-density profile for wet native collagen. *Biophys. J.* **26**:209-221.

84. Dubois, G. M., Z. Haftek, C. Crozet, R. Garrone, and D. Le Guellec. 2002 Structure and spatio temporal expression of the full length DNA complementary to RNA coding for alpha2 type I collagen of zebrafish. *Gene* **294**:55-65.

85. Fisher, S., P. Jagadeeswaran, and M. E. Halpern. 2003. Radiographic analysis of zebrafish skeletal defects. *Dev. Biol.* **264**:64-76.

86. Saito, M., Y. Takenouch, N. Kunisaki, and S. Kimura. 2001. Complete primary structure of rainbow trout type I collagen consisting of alpha1(I)alpha2(I)alpha3(I) heterotrimers. *Eur. J. Biochem.* **268**:2817-2827.

87. Aspden, R. M., and D. W. L. Hukins. 1979. Determination of the direction of preferred orientation and the orientation distribution function of collagen fibrils in connective tissues from high-angle x-ray-diffraction patterns. *J. Appl. Cryst.* **12**:306-311.

88. Bigi, A., A. Ripamonti, N. Roveri, L. Compostella, L. Roncon, and L. Schivazappa. 1982. Structure and orientation of collagen fibers in human mitral valve. *Int. J. Biol. Macromol.* **4**:387-392.

89. Hosemann, R., R. Bonart, and T. Nemetschek. 1974. The inhomogeneous stretching process of collagen. *Colloid Polym. Sci.* **252**:912-919.

90. Warren, B. E. 1941. X-ray diffraction methods. *J. Appl. Phys.* **12**:375-384.

91. Harrison, I. R., S. J. Kozmiski, W. D. Varnell, and J.-I. Wang. 1981. SAXS instrumental broadening and the order dependence of peak width. *J. Polym. Sci. Polym. Phys. Ed.* **19**:487-497.

92. Strobl, G. R. 1973. Determination of the lamellar structure of partially crystalline polymers by direct analysis of their small-angle X-ray scattering curves. *J. Appl. Cryst.* **6**:365.

93. Hosemann, R., and S. N. Bagchi. 1962. *Direct analysis of diffraction by matter*, Chap. 12, North-Holland, Amsterdam.

94. Rey, C., H. M. Kim, I. Gerstenfeld, and M. J. Glimcher. 1995. Structural and chemical characteristics and maturation of the calcium-phosphate crystals formed during the calcification of the organic matrix synthesized by chicken osteoblasts in cell-culture. *J. Bone Miner. Res.* **10**:1577-1588.

95. Glimcher, M. J. 1976. Composition, structure and organization of bone and other mineralized tissue and the mechanism of calcification. In *Handbook of Physiology: Endocrinology*. R. O. Greep, and E. B. Astwood, editors. American Physiological Society, Washington, DC. p25.

96. Robinson, R. A. 1952. An electron-microscope study of the crystalline inorganic component of bone and its relationship to the organic matrix. *J. Bone Joint Surg.* **34**:389-434.

97. Fratzl, P., S. Schreiber, and K. Klaushofer. 1996. Bone mineralization as studied by small-angle x-ray scattering. *Connect. Tissue Res.* **34**:247-254.

98. Traub, W., T. Arad, and S. Weiner. 1989. Three-dimensional ordered distribution of crystals in turkey tendon collagen-fibers. *Proc. Natl. Acad. Sci. USA* **24**:9822-9826.

99. Zylberberg L, T. W., De Buffrenil V, Allizard F, Arad T, Weiner S. 1998. Rostrum of a toothed whale: Ultrastructural study of a very dense bone. . Bone 23:241-247.

100. Zernike, F., and J. A. Prins. 1927. X-ray diffraction from liquids. *Zeits. f. Physik* **41**:184-194.

101. Burger, C., H.-W. Zhou, S. Igors, B. S. Hsiao, B. Chu, L. Graham, and M. J. Glimcher. 2008. SAXS study of intramuscular fish bone: Collagen fibril superstructure determined from equidistant meridional reflections. *J. Appl. Cryst.* **41**:252-261.

102. Hermans, J. J. 1944. Concerning the influence of grid disturbances on the X-ray pattern, particularly in gels. *Rec. Trav. Chim. Pays-Bas* **63**:211-218.

103. Engstrom, A. 1972. Aspects of the molecular structure of bone. In *The biochemistry and physiology of bone* G. H. Bourne, editor. Academic, New York. 237-257.

104. Amemiya, Y. 1995. Imaging plates for use with synchrotron radiation. *J. Synchrotron Rad.* **2**:13-21.

105. Jäger, I., and P. Fratzl. 2000. Mineralized collagen fibrils: a mechanical model with a staggered arrangement of mineral particles. *Biophys. J.* **79**:1737-1746.

106. Boskey, A. L. 1996. Matrix proteins and mineralization: An overview. *Connect. Tissue Res.* **35**:357-363.

107. Robey, P. G. 1996. Vertebrate mineralized matrix proteins: Structure and function. *Connect. Tissue Res.* **35**:131-136.

108. Hulmes, D. J. S., A. Miller, D. A. D. Parry, K. A. Piez, and J. Woodhead-Galloway. 1973. Analysis of primary structure of collagen for origins of molecular packing. *J. Mol. Biol.* **79**:137-148.

109. McLachlan, A. D. 1977. Analysis of periodic patterns in amino-acid sequences - collagen. Biopolymers 16:1271-1297.

110. Miller, A. 1984. Collagen: the organic matrix of bone. *Phil. Trans. R. Soc. Lond. B* **304**:455-477.

111. Eyre, D. R. 1984. Cross-linking in collagen and elastin. *Ann. Rev. Biochem.* **53**:717-748.

112. Eyre, D. R. 1987. Collagen cross-linking amino acid. *Methods in Enzymology* **144**:115-139.

113. Yamauchi, M., E. P. Katz, K. Otsubo, K. Teraoka, and G. L. Mechanic. 1989. Cross-linking and stereospecific structure of collagen in mineralized and nonmineralized skeletal tissues. *Connect. Tissue Res.* **21**:159-169.

114. Yamauchi, M., and E. P. Katz. 1993. The post-translational chemistry and molecular packing of mineralizing tendon collagens. *Connect. Tissue Res.* **29**:81-98.

115. Knott, L., and A. J. Bailey. 1998. Collagen cross-links in mineralizing tissues: A review of their chemistry, function, and clinical relevance. *Bone* **22**:181-187.

116. Eyre, D. R., and J.-J. Wu. 2005. Collagen cross-links. *Top. Curr. Chem.* **247**:207-229.

117. Featherstone, J. D., S. Pearson, and R. Z. LeGeros. 1984. An infrared method for quantification of carbonate in carbonated apatites. *Caries Res.* **18**:63-66.

118. Rey, C., B. Collins, T. Goehl, I. R. Dickson, and M. J. Glimcher. 1989. The carbonate environment in bone-mineral - A resolution-enhanced Fourier-transform infrared-spectroscopy study. *Calcif. Tissue Int.* **45**:157-164.

119. Beshah, K., C. Rey, M. J. Glimcher, M. Shimizu, and R. G. Griffin. 1990. Solid state carbon and proton NMR studies of carbonate containing calcium phosphates and enamel. *J. Solid State Chem.* **84**:71-81.

120. Wu, Y., M. J. Glimcher, C. Rey, and J. L. Ackerman. 1994. A unique protonated phosphate croup in bone-mineral not present in synthetic calcium phosphates - Identification by P-31 solid-state NMR-spectroscopy. *J. Mol. Biol.* **244**:423-435.

121. Biltz, R. M., and E. D. Pellegrino. 1971. The hydroxyl content of calcified tissue mineral. *Calcif. Tissue Res.* **36**:259-263.

122. Termine, J. D., E. D. Eanes, D. J. Greenfield, M. U. Nylen, and R. A. Harper. 1973. Hydrazine-deproteinized bone mineral: Physical and chemical properties. *Calcif. Tissue Res.* **12**:73-90.

123. Bonar, L. C., M. Shimizu, J. E. Roberts, R. G. Griffin, and M. J. Glimcber. 1991. Structural and composition studies on the mineral of newly formed dental enamel:

A chemical, x-ray diffraction, and 31p and proton nuclear magnetic resonance study. *J. Bone Miner. Res.* **6**:1167-1176.

124. Rey, C., J. L. Miquel, L. Facchini, A. P. Legrand, and M. J. Glimcher. 1995. Hydroxyl groups in bone mineral. *Bone* **16**:583-586.

125. Loong, C.-K., C. Rey, L. T. Kuhn, C. Combes, Y. Wu, S.-H. Chen, and M. J. Glimcher. 2000. Evidence of hydroxyl-ion deficiency in bone apatites: An inelastic neutron-scattering study. *Bone* **26**:599-602.

126. Cho, G.-G., Y.-T. Wu, and J. L. Ackerman. 2003. Detection of hydroxyl ions in bone mineral by solid-state NMR spectroscopy. *Science* **300**:1123-1127.

127. Bella, J., M. Eaton, B. Brodsky, and H. M. Berman. 1994. Crystal and molecular structure of a collagen-like peptide at 1.9 Å resolution. *Science* **266**:75-81.

128. Berisio, R., L. Vitagliano, L. Mazzarella, and A. Zagari. 2002. Crystal structure of the collagen triple helix model $[(\text{Pro-Pro-Gly})_{10}]_3$. *Protein Sci.* **11**:262-270.

129. Chen, J. M., C. E. Kung, S. H. Feairheller, and E. M. Brown. 1991. An energetic evaluation of a smith collagen microfibril model. *J. Protein Chem.* **10**:535-552.

130. Brown, E. M., G. King, and J. M. Chen. 1997. Model of the helical portion of a type I collagen microfibril. *J. Am. Leather Chem. Assoc.* **92**:1-7.

Appendix I. Scattering from Microfibrillar Packing in Bone Collagen Fibrils Based on Assumption of Simple Rotational Disorder

For a packing of microfibrils with ideal rotational disorder, i.e., the centers of the microfibrils are located at the lattice points but the internal structure of a microfibril is randomly oriented in all radial directions with respect to its center, the scattering from such a system is given by the Laue substitution disorder approach,

$$I(\vec{s}) = \left\langle \left|F(\vec{s})\right|^2 \right\rangle_{\Psi} - \left|\left\langle F(\vec{s})\right\rangle_{\Psi}\right|^2 + \left|\left\langle F(\vec{s})\right\rangle_{\Psi}\right|^2 \cdot \left|Z(\vec{s})\right|^2 \qquad \text{(A1)}$$

where $\vec{S}$ is the reciprocal lattice vector, $s = |\vec{s}| = 2\sin\theta/\lambda$, θ is the scattering angle, and λ is the wavelength of the incident beam. $\left\langle \left|F(\vec{s})\right|^2 \right\rangle_{\Psi}$ is the scattering from an individual microfibril,

$$\left\langle \left|F(\vec{s})\right|^2 \right\rangle_{\Psi} = J_0(2\pi \cdot R \cdot s)^2 + 2\sum_{n=1}^{\infty} J_{5n}(2\pi \cdot R \cdot s)^2 \qquad \text{(A2)}$$

where J_0 and J_{5n} are the Bessel functions of the first kind of *zero* and *5n* orders, respectively. *R* is the radius of the circle passing through the 5 molecule centers in the Smith's type microfibril ((48), see Fig. A1). The relationship between *R* and the center-to-center intermolecular distance *d* is $R = d[(1+5^{-1/2})/2]^{1/2}$.

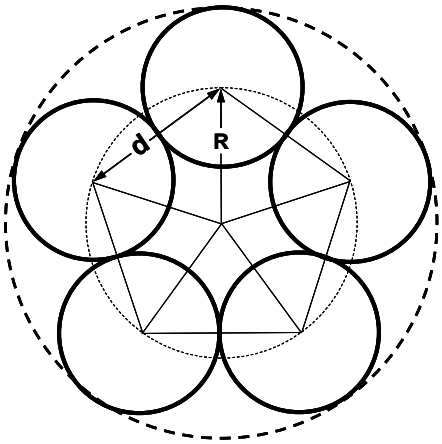

Figure A1. Geometric relationship in a Smith's type 5-strand microfibril.

$\left|\left\langle F(\vec{s})\right\rangle_{\Psi}\right|^2$ is the scattering from a rotationally averaged microfibril, which is equivalent to the scattering from a hollow cylinder with $R + d/2$ being the outer diameter and $R - d/2$ being the inner diameter,

$$\left|\left\langle F(\vec{s})\right\rangle_{\Psi}\right|^2 = J_0(2\pi \cdot R \cdot s)^2 \tag{A3}$$

Therefore,

$$I(\vec{s}) = 2\sum_{n=1}^{\infty} J_{5n}(2\pi \cdot R \cdot s)^2 + J_0(2\pi \cdot R \cdot s)^2 \cdot \left|Z(\vec{s})\right|^2$$

$$\approx 2J_5(2\pi \cdot R \cdot s)^2 + J_0(2\pi \cdot R \cdot s)^2 \cdot \left|Z(\vec{s})\right|^2 \tag{A4}$$

where $J_5(2\pi \cdot R \cdot s)^2$ is the fluctuation term that produces the equatorial interference maximum at about 1.06 nm (Fig. A2); $J_0(2\pi \cdot R \cdot s)^2$ is the form factor or the Fourier transform of the electron density of a rotationally averaged microfibril; and $\left|Z(\vec{s})\right|^2$ is the Fourier transform of the 2D oblique lattice for the ordered microfibrillar packing. The overall scattering intensity calculated from equation A4 was showed in Fig. A3.

However, a comparison between the experimental curve (Fig. A2, *black*) and the calculated one (Fig. A3) shows that equation A4 cannot be used to quantitatively analyze the equatorial scattering pattern from native, uncalcified intramuscular herring bone. A packing of microfibrils with ideal rotational disorder will produce a broader interference maxima (Fig. A2, *red*) than the measured one (Fig. A2, *black*). If there is no rotational disorder, i.e., the locations of the collagen molecules in different microfibrils are also in register, the scattering intensity will be simplified to

$$I(\vec{s}) = \left|F(\vec{s})\right|^2 \cdot \left|Z(\vec{s})\right|^2 \qquad \text{(A5)}$$

where $\left|F(\vec{s})\right|^2$ is the form factor of the 5-strand microfibrils. Note equation A5 does not contain the fluctuation term. One would expect a series of discrete narrow peaks at the position corresponding to the interference maximum showed in Fig. A2. The experimental scattering intensity profile seems to be somewhere between the case of ideal rotational disorder and the case of no rotational disorder, suggesting that the packing of microfibrils in bone collagen fibrils should have partial rotational disorder.

Fig. A3 shows that the (1 1) reflection at 1/2.670 nm^{-1} is suppressed by the form factor $J_0(2\pi \cdot R \cdot s)^2$, which explains the absence of this low order peak in the measured intensity profile. The unit cell also predicts some unobserved Bragg reflections, suggesting that the Smith's type microfibril model might be oversimplified. Information about other structural defects, such as the deviation of the microfibril cross-section from the ideal pentagon shape due to intra- and inter- microfibrillar interactions and the α-chain packing disorders in collagen triple helix, is needed for a more quantitative evaluation of the scattering intensity from bone collagen fibrils.

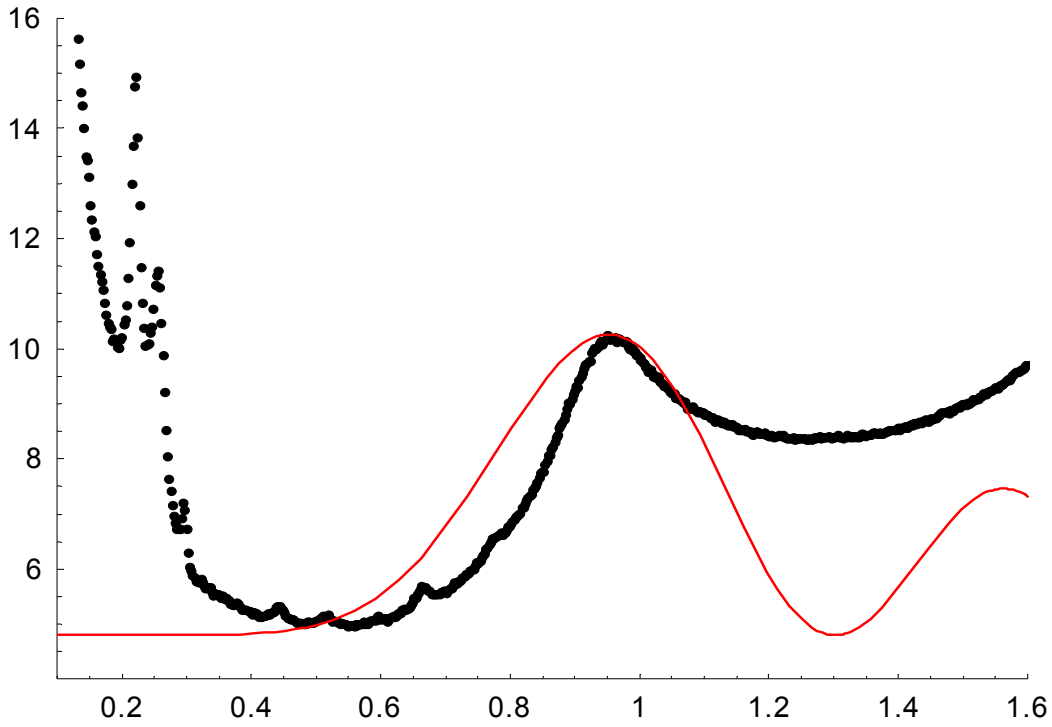

Figure A2. The observed equatorial intensity profile for native, uncalcified herring bone collagen is shown in black. The sharp Bragg reflections originate from the ordered packing of microfibrils in lateral direction. The broad "peak" at ca. 1/1.06 nm^{-1} originates from the interference between neighboring collagen molecules. For Smith's type 5-strand microfibrils with ideal rotational disorder, the fluctuation term (showed in red, also see equation A4) contributes to most of the intensity and the shape of the broad peak at 1/1.06 nm^{-1}. The center-to-center distance $d \sim 1.26$ nm was chosen to obtain the best fit between the calculated interference maximum and the measured one. The value of d is in good agreement with those in literatures (see Tab. A1).

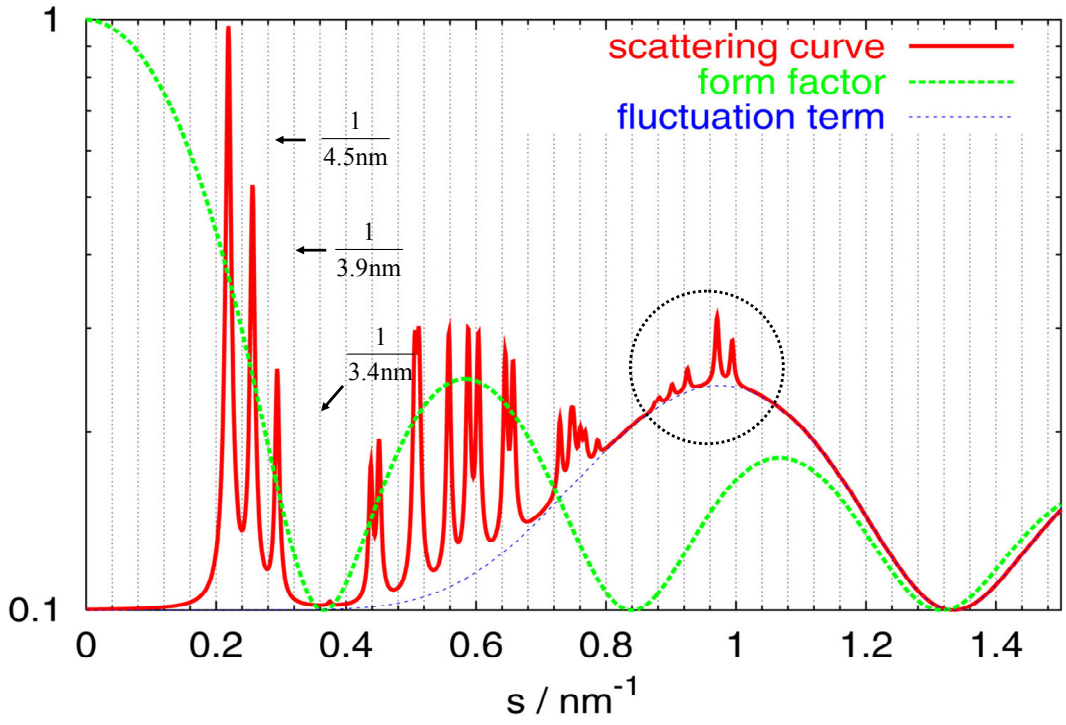

Figure A3. Calculated overall intensity of microfibrillar packing with ideal rotational disorders.

Table A1. "Diameter" of collagen triple helix and Smith 5-strand microfibril

Type	**Diameter** (nm)	**Techniques**	**Remark**
Triple Helix:			
Reconstituted steer skin collagen	1.18	XRD	Equivalent diameter (44)
	1.25	XRD	Contact diameter (44)
Turkey leg tendon collagen	1.19	XRD	Effective repulsion diameter (71)
RTT collagen	1.18	XRD	Effective repulsion diameter (59)
Ala substituted $(Gly\text{-}Pro\text{-}Hyp)_{10}$	1.0	XRD	No long side chains (127)
$[(Gly\text{-}Pro\text{-}Pro)_{10}]_3$	1.0	XRD	No long side chains (128)
$(Gly\text{-}Pro\text{-}Hyp)_{12}$	1.26	Energy-minimized computational model	No long side chains (129)
Microfibril:			
$(Gly\text{-}Pro\text{-}Hyp)_{12}$	3.20	Energy-minimized computational model	No long side chains (129)
Bovine type I collagen, segment	2.87 ~ 3.43	Energy-minimized computational model	Backbone (130)
	3.20 ~ 3.55	Energy-minimized computational model	With side chains (130)

The rotational disorder of microfibrils might be regulated by the cross-linking of collagen molecules, as pointed out by Bailey (8) and other authors (113, 114). However, information about the cross-linkage in herring bone collagen is not yet available. Ideally, a comparative XRD and cross-linking study may give the correlation between cross-linkage and molecular packing. However, the sampling volume tested by X-ray is so small (~ 0.01 mm^3 or ~ 0.01 mg) that it is not sufficient for the sequencing analysis and hence identifying the cross-linking types. Nevertheless, the present structure information may still give some insight about the nature of cross-links in bone collagen. For instance, it could be conceived that cross-linkage is between molecules from neighboring microfibrils since molecules within a microfibril are closely packed and there is limited space for large cross-linking structures such as pyridinoline and/or pyrrole (for more information about bone collagen cross-links, see reviews (111, 112, 115, 116)).